MECHANISM OF FOAMING ON

POLYMER-PAPERBOARD COMPOSITES

A Thesis
Presented to
The Academic Faculty

by

Sriram Kiran Annapragada

In Partial Fulfillment
of the Requirements for the Degree
Doctor of Philosophy in the
School of Chemical & Biomolecular Engineering

Georgia Institute of Technology
December, 2007

MECHANISM OF FOAMING ON

POLYMER-PAPERBOARD COMPOSITES

Approved by:

Dr. Sujit Banerjee, Advisor
School of Chemical & Biomolecular Engineering
Georgia Institute of Technology

Dr. Timothy Patterson, Co-Advisor
School of Mechanical Engineering
Georgia Institute of Technology

Dr. Dennis Hess
School of Chemical & Biomolecular Engineering
Georgia Institute of Technology

Dr. Carson Meredith
School of Chemical & Biomolecular Engineering
Georgia Institute of Technology

Dr. Gregory Fike
Neenah Technical Center,
Georgia-pacific Corporation

Date Approved: October 31st, 2007

“To my Parents”

ACKNOWLEDGEMENTS

I would like to thank my thesis advisor Dr. Sujit Banerjee for his support and guidance throughout the research project. It has been a wonderful learning experience working with him. Next, I would like to thank my co-advisor Dr. Timothy Patterson for his insight into the different aspects of the project. I would also like to thank Dr. Gregory Fike of Georgia-Pacific Corporation for both serving on my committee and also helping me coordinate with the research group at Neenah Technical Center.

Thanks to the thesis committee members Dr. Dennis Hess and Dr. Carson Meredith for their valuable suggestions and inputs. I would also like to thank Dr. William Koros for providing his insight into the theoretical aspects of the work. Thanks also to Banerjee group members for all the good times together; especially to Usha Hooda, Tuan Le, Uma Udaysankar and Mike Buchannan for also assisting me in the experimental work.

I would also like to acknowledge the financial support provided by the Institute of Paper Science and Technology and Georgia-pacific Corporation. Lastly, I am grateful for having a wonderful set of parents, brother and friends whose support always plays a key role in all my achievements.

TABLE OF CONTENTS

LIST OF TABLES

LIST OF FIGURES

LIST OF EQUATIONS

SUMMARY

The use of traditional polymeric foams has raised several environmental concerns leading the industry to seek greener solutions for food packaging. This thesis addresses a new technique of foaming on polymer-paperboard composites which combines the advantages of traditional polymeric foam with the environmental benefits of paperboard. Paperboard is sandwiched between two extruded polymeric layers of different densities. On application of heat, one face is foamed by the evaporating moisture in the board [10]; the other face serves as a barrier. The moisture inside the board vaporizes and moves in the thickness direction to serve as the driving force behind the foaming process. Different polymers can be employed in the process [10].

The current work is directed at gaining a better understanding of the fundamental processes in foaming polymers on paperboard. The ultimate goal is to be able to produce uniform bubbles of a predetermined size on the surface so as to give optimum heat insulation and good tactile properties. A combination of experimental techniques was employed to study the foaming process. Low Density Polyethylene (LDPE) of different grades extruded at different speeds and to different thicknesses were foamed on paperboard constructed under different conditions.

Scanning Electron Microscopy (SEM) studies of the board cross section determined that pores present on the paper surface serve as bubble growth sites; the shape and size of the pores were also found to play a role in the final bubble size distribution. A high speed

imaging technique was used to track individual bubbles. Different properties of paper were varied to determine its role in foaming. The paper properties were found to be the primary controlling factor in the number of bubbles initially formed. A new SEM-Imaging technique was developed to study the surface uniformity of pores. The growth rate of bubbles depends on the paperboard sheet resistance. These conclusions were further confirmed using infrared thermography.

Bubble growth was studied as a function of paperboard properties, polymer melt index, extrusion speed, polymer thickness, temperature and moisture content. It was concluded that the bubble size which relates to the final foam thickness was controlled by the thickness of the polymer layer and its ability to bond with the paperboard. The effect of coalescence on the size distribution was determined.

Pore size distribution was analyzed using SEM images of the paper surface. Vapor loss measurements were made to determine the different fractions of moisture lost during the foaming process. The theoretical maximum bubble size was predicted and compared to the average bubble size seen in the imaging experiments. It was found that the bubble size is limited by the cell wall thickness. The degree of coalescence controlled the final cell size distribution. Thicker foams resulted from increased coalescence.

In summary, foaming is caused by the vapor escaping from the pores in the paperboard substrate and subsequent foaming of the polymeric layer. The vapor driving force depends on the paperboard properties as well as on the ability of the polymer to bond

with the paperboard. The bubbles initially formed relate directly to the pore distribution; coalescence subsequently occurs and leads to an increase in foam thickness.

CHAPTER 1: INTRODUCTION

Foams are cellular plastics with gas bubbles dispersed in a polymeric matrix. They are light, low-cost, and have good thermal insulation and strength properties with high commercial significance. As a result they are widely used in food packaging and in other consumer products industries [1-4]. Food packaging includes products such as coffee cups, cookie trays, pizza boxes and represents an $11 billion industry annually [5]. A large percentage of food packaging currently employs foam based products such as Styrofoam.

Several environmental concerns with the extensive use of traditional foams in packaging have been raised recently. Their light weight (low density) causes the generation of large volumes of waste, which further leads to problems with collection and transportation. The waste can end up in storm drains and marine environments raising environmental concerns [6, 7]. Waste that is collected is usually landfilled. Traditional foam resins are petroleum based and need several decades to degrade in these landfills [8]. Foam recycling is the other feasible option, but there are two key problems. The low cost of foam products gives little incentive for manufacturers to recycle. Furthermore, efforts to economically recycle foam waste have not yet been successful [9]. Foams used in food packaging are also difficult to recycle because of potential contamination with food [8]. Other concerns with traditional foams used in the past have been with regard to the manufacturing process which employs environmentally harmful blowing agents such as

CFC (e.g. CFC-11) and HCFC (e.g. HCFC-141b, HCFC-22 etc.) [2]. Several studies are currently underway to identify greener blowing agents [1,2].

Greener products such as paper and biodegradable polymers have been proposed as a viable alternative to traditional polymeric foams. Although these greener alternatives have successfully been used to manufacture food service products such as cups, plates, boxes etc., they are not cost-effective when compared to traditional foams. The present study is a step towards developing a long term environmentally friendly alternative to foam-based products. Foaming on paperboard is a relatively new technique first developed by Nippon Dixie Co. Ltd. in 1984, which combines the advantages of traditional polymeric foam with the environmental benefits of paperboard [10]. Paperboard is sandwiched between two extruded polymeric layers of different densities as illustrated in Figure 1.1.

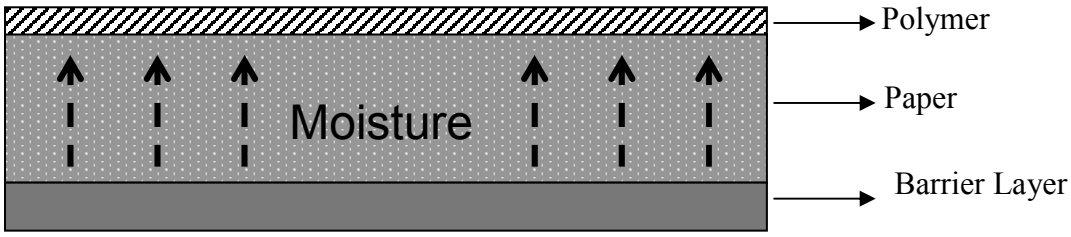

Figure 1.1 Schematic of the extruded board composite

On application of heat, one face is foamed by the evaporating moisture in the board [10]; the other face serves as a barrier. The moisture inside the board vaporizes and traverses in the thickness direction to serve as the driving force behind the foaming process. Different polymers can be employed in the process [10]. Traditional polymeric foams are

manufactured from different processes such as use of expandable beads, injection molding and extrusion. They usually employ a chemical blowing agent dispersed in the polymer [1-4]. The pre-blended mixture is melted in a cell followed by a reduction in cell pressure causing the blowing agent (gas) to become supersaturated leading to nucleation and non isothermal bubble growth [11]. The foam quality is, in effect, dictated by the nucleation kinetics and the bubble growth dynamics. Several factors could affect such a process including temperature, pressure, nucleating agents, melt rheology and the solubility of the blowing agent [1, 2, 12]. This process has been extensively studied in the literature [13-24]. Foaming on polymer-paper composites differs from traditional foams in two key aspects -

1. It replaces the blowing agent with moisture, which reduces cost and minimizes environmental concerns.
2. The composite replaces between 80 and 90% of the polymeric material used in traditional foams with paperboard: a well known cheap renewable substrate.

The composite, in turn, offers the same advantages of heat insulation and good tactile properties that traditional foams do in food packaging. In contrast to traditional foaming where the solubility of dissolved blowing agent plays a key role, the vapor pressure generated by the moisture drives the paperboard foaming process. The bubble formation is limited to a thin layer of extruded polymer on the surface. The parameters influencing paperboard foaming are hypothesized to be the paperboard moisture content, the foaming temperature, the duration of exposure to elevated temperature, polymer extruded weight, extrusion speed, polymeric properties and interfacial properties. The fundamental

processes in paperboard foaming have not been studied in the literature before and are not well understood. The recent commercial interest in this product is the primary motivation behind this study. The current work is directed at gaining a better understanding of the fundamental processes in foaming polymers on paperboard. The ultimate goal is to be able to produce uniform bubbles of a predetermined size on the surface so as to give enhanced heat insulation and good tactile properties. A foamed board with uniform cell size distribution is shown in Figure 1.2.

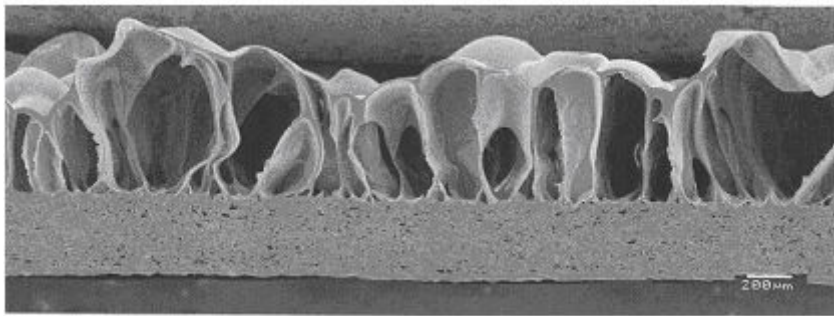

Figure 1.2 Cross section of foamed board with uniform cell size distribution.

This work could also help develop biodegradable polymers that could be used to foam on paperboard, thus providing a complete environmentally friendly food packaging solution. The three main objectives of the current study were as follows –

1. Determine the fundamental mechanism of bubble formation in foaming.
2. Determine the most sensitive process parameters that affect the final foam cell size distribution.
3. Relate foam quality (thickness) to the cell size distribution and determine the various factors affecting it.

A combination of experimental investigations was employed to achieve these objectives.

CHAPTER 2: BACKGROUND and LITERATURE REVIEW

Foaming on polymer-paper composites is a relatively new technique, which produces a layer of foam on paperboard. No published literature specific to this topic is available. This chapter aims to give a broad overview of the background and literature of the different parameters that could affect such a foaming process.

To compare the pros and cons of the technique presented here the chapter begins with a discussion of the traditional foaming process and the properties that makes it so widely used today. A discussion of the properties of paper, polymer and the interface is included to help understand the role of various parameters that could be important in paperboard foaming. Moisture drives the current process; the different transport mechanisms and role of moisture would thus be important and is also reviewed here. Lastly, the theory behind the infrared thermography technique used to study the foaming mechanism in the current study is also discussed.

2.1 Polymeric Foams

Foams are lightweight polymeric structures with a gas phase dispersed in the form of bubbles as shown in Figure 2.1 [1, 2]. Polymeric properties such as melting point, rheological properties, molecular weight, etc., play an important role in the traditional foaming processes. This section focuses on traditional foaming technology.

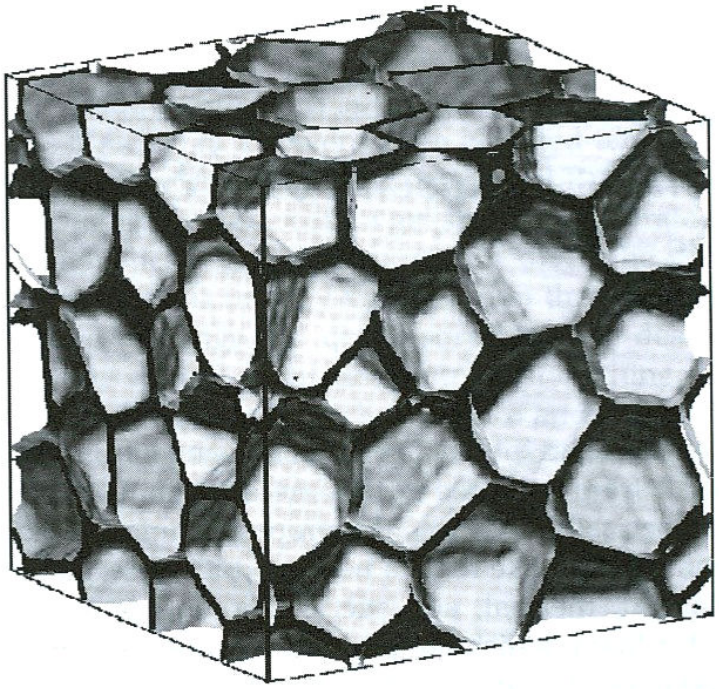

Figure 2.1 Structure of Foam [2]

2.1.1 Non-Newtonian behavior of Polymeric fluids

Polymers are structurally complex fluids which exhibit non-Newtonian behavior [25]. The high molecular weight causes polymeric molecules to differ in terms of non Newtonian viscosity and the elastic effects experienced. The non-Newtonian viscosity and shear normal stresses are defined as follows [25]:

$$\tau_{yx} = -\eta \frac{dv_x}{dy} \tag{2.1}$$

$$\tau_{xx} - \tau_{yy} = -\psi_1 \left(\frac{dv_x}{dy} \right)^2 \tag{2.2}$$

$$\tau_{yy} - \tau_{zz} = -\psi_2 \left(\frac{dv_x}{dy} \right)^2 \tag{2.3}$$

where -

τ_{yx} is the shear stress in the x direction on an unit area perpendicular to the y direction,

η is the non Newtonian viscosity,

$\frac{dv_x}{dy}$ is the change in velocity in the y direction

$\tau_{xx}, \tau_{yy}, \tau_{zz}$ are normal stresses

ψ_1 and ψ_2 are the first and second stress coefficients.

The viscosity and stress coefficients are functions of the shear rate λ. In the case of Newtonian fluids, $\eta = \mu$, the Newtonian viscosity, and $\psi_1 = 0$ & $\psi_2 = 0$. Thus, for non-Newtonian fluids, one needs to account for both viscosity and other effects such as normal stresses, time dependency and elasticity. Several models have been proposed to describe these effects for non-Newtonian polymeric fluids [25]. A generalized Newtonian fluid model can be described as

$$\tau = -\eta \dot{\gamma} \tag{2.4}$$

$\dot{\gamma}$ is called the rate of strain tensor or the rate of deformation tensor.

A simpler model that captures the non-Newtonian viscosity but does not account for effects of normal stresses, time and elastic effects is the power law model which relates the non-Newtonian viscosity to the strain tensor as [25]:

$$\eta = m \dot{\gamma}^{n-1} \tag{2.5}$$

where m and n are constants characteristic of the fluid.

Another class of models is referred to as linear viscoelastic models; these account for time effects and employ a linear relation between the non-Newtonian viscosity and the strain tensor. A simple model that describes both viscous and elastic effects is the Maxwell model, which is given as [25]:

$$\tau + \lambda_1 \frac{\partial}{\partial t}\tau = -\eta_0 \dot{\gamma} \tag{2.6}$$

where -

λ_1 is the time constant or relaxation time

η_0 is the zero shear rate viscosity.

A generalized Maxwell model includes several relaxation times corresponding to different internal degrees of freedom possessed by a polymeric liquid. A more complex class of models is the non linear viscoelastic model, which relates the stress tensor to the rate of strain tensor through the addition of non linear terms. One of the commonly used non linear viscoelastic model is the Oldryod-B model, which is given as [25]:

$$\tau + \lambda_1 \frac{D}{Dt}\tau - \frac{1}{2}\lambda_1\{\tau\cdot\gamma + \gamma\cdot\tau\} = -\eta_0\left(\dot{\gamma} + \lambda_2 \frac{D}{Dt}\dot{\gamma} - \lambda_2\left\{\dot{\gamma}\cdot\dot{\gamma}\right\}\right) \tag{2.7}$$

where –

λ_1, λ_2 are time constants.

2.1.2 Traditional foaming processes

The two manufacturing techniques which are widely used in traditional polymeric foams are soluble foaming and reactive foaming [1]. They employ three steps - gas implementation, expansion and stabilization of the foam [2]. These are illustrated in Figure 2.2. Soluble foaming employs a blowing agent, dissolved into the polymer solution at high pressure. A reduction in pressure causes the gas to vaporize leading to the nucleation and bubble growth [1,2]. The solubility of the blowing agent is the controlling factor in the process, which, in turn, depends on the pressure and temperature of the system. The selection of a polymer-blowing agent combination depends on the final foam properties desired, processing issues, and compliance with environmental regulations. Polystyrene and polyethylene are two good examples of soluble foaming [1, 26].

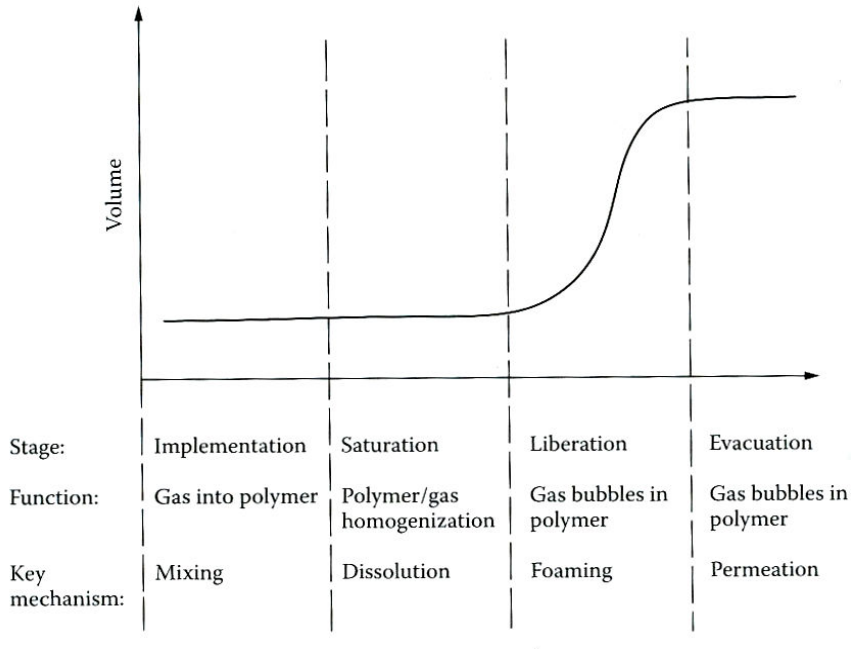

Figure 2.2 Steps in foaming [1]

Reactive foaming leads to gas generation due to a chemical reaction in the polymeric mixture, and is the more widely used technique today [1]. Some examples of polymers foamed through reactive foaming are polyurethane, polyisocyanurate and phenolics [1,26]. The reactive foaming process can be better understood by considering the example of polyurethane foaming which involves both polyols and isocyanate. Water reacts with isocyanate to form CO_2 which serves as the foaming agent. A variation in the type and ratio of components added leads to a plethora of products with different densities, dimensions and cell size distribution.

2.1.3 Properties of Foams

Foams are known to provide low cost solutions in a variety of applications such as construction, automobiles, transportation, sports, pharmaceutical and home furnishings [1, 2]. The density reduction obtained due to the dispersion of gas bubbles inside the polymeric matrix gives foam its two main properties of insulation and mechanical strength [27].

The amount of gas dispersed depends on the cell (bubble) size distribution. Figure 2.3 compares materials of different densities and their corresponding thermal conductivity and Young's modulus [2, 28, 29]. Foams have a low thermal conductivity and Young's modulus. The low thermal conductivity due to negligible heat convection in the gas phase leads to the good insulation properties of foams. A low Young's modulus implies high

flexibility of foams when under stress. In the present study, the insulation properties of foam layer are of principal consideration.

Density reduction also leads to structural changes in foams. Thus, a number of other factors such as expansion ratio, cell size distribution, open cell content and cell integrity play a role in the final foam properties. Blowing agents also contribute to the insulation properties. Any residual blowing agent would increase the insulation. Blowing agents are eventually replaced by air; as a result, the insulation properties decrease over time.

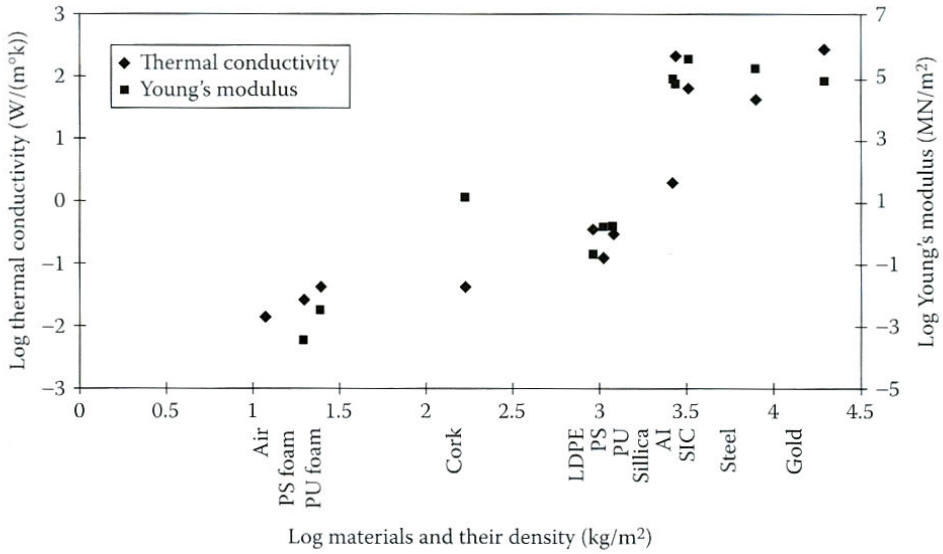

Figure 2.3 Variation of thermal conductivity and Young's modulus for different materials [2, 28, 29]

2.1.3.1 Cell size distribution

The cell size distribution is important for determining the mass and heat transfer characteristics of the foam as well as its material properties. Smaller cells lead to better

energy absorption and insulation properties due to the increased resistance to heat transfer, as illustrated in Figure 2.4 [2]. Smaller cells also give better insulation due to reduced radiation effects in the cell during heat transfer [30]. The degree to which the gas phase can be compressed under deformation dictates the strength of the foam [2]. The properties of low density polyethylene foams are also known to be dominated by how well the gas is dispersed [2].

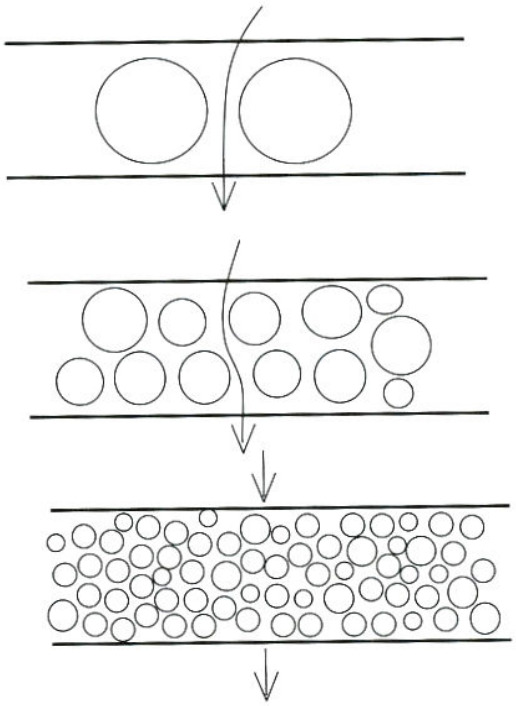

Figure 2.4 Heat flux in different foam cell size distribution [2]

In traditional foams, the cell size and number depends on the nucleation process. This is an energy controlled step where the stable nuclei gain energy to offset the opposition forces in order to grow. Nucleation does not occur uniformly across the polymeric phase; it begins earlier at some points than at others [31].

2.1.3.2 Cell structure

The cell structure is dependent on the shape of the bubbles formed, which is a function of bubble birth (nucleation in traditional foaming) and coalescence. According to packing theory a bubble that expands to about four times its initial size inevitably makes contact with its neighboring bubbles [3]. This is also the case if the final foam contains 75% or more void space (gas). The degree to which bubbles can grow or make contact with their neighbors affects the rate of coalescence.

Coalescence creates open cells or interconnected bubbles which contribute to poor material strength and the insulation properties of foam [32, 33, 34]. On the other hand, open cells lead to the formation of capillaries which allows the absorption of fluids. These cells also help in sound insulation due to the attenuation of sound waves [2]. Spherical bubbles will provide the best insulation and strength properties. Coalescence should be limited in order to have several small spherical bubbles. This could be achieved by incorporating two sets of bubble birth processes; a primary nucleation step leading to the first set of bubbles. This is followed by a secondary nucleation which helps fill inter bubble space thereby reducing density without sacrificing the spherical shapes of bubbles and also retaining the structural integrity of the foam [2].

2.1.3.3 Estimating Foam Density

The reduction in foam density can be determined as –

$$\rho_f = \frac{(W_g + W_p)}{(V_g + V_p)} \tag{2.8}$$

where

ρ – density of foam

W – weight of foam

V – volume of foam

g – gas

p – polymer

As the foam size increases, the volume of the polymer becomes negligible compared to that of the gas, while the weight of gas becomes negligible compared to that of the polymer. Hence the density can be approximated as [2] -

$$\rho_f = \frac{W_p}{V_g} \tag{2.9}$$

The mechanical strength of foam is a function of its density and structure. To understand the effects of density and cell structure (open or closed) on their mechanical properties, the cubic cell model proposed by Gibson and Ashby [28] can be used. For the case of open cells, they proposed the following relation between the modulus (M) to the density -

$$\frac{M_f}{M_p} = \left(\frac{\rho_f}{\rho_p}\right)^2 \tag{2.10}$$

For closed cell structures, the modulus depends both on the effects of cell wall buckling and cell wall stretch and is related to the density as -

$$\frac{M_f}{M_p} = (1-\phi)\left(\frac{\rho_f}{\rho_p}\right) \tag{2.11}$$

where ϕ denotes the strut volume as discussed in the model [28]. The strength decreases linearly with the density reduction for closed cells and on the square of density function for open cells. Thus it can be inferred that open cells present a lower modulus compared to closed cells and deform more under stress. In many cases, the amount of open cell content determines its end use. Open cell morphology in foams has been well studied in the literature and is also known to be caused by processing conditions [2] such as the percent of blowing agent employed, screw design, foaming temperature etc.

2.1.4 Nucleation and bubble growth processes in foaming-

Nucleation leads to the formation of gas bubbles inside the polymeric phase during foaming [1, 2]. A nucleated bubble so formed is termed a critical bubble, which is intrinsically unstable and grows further. The bubble growth creates a concentration gradient in the system leading to the diffusion of gas from the polymeric solution, which in turn feeds the growth process [1,2]. Bubble growth is a complex process involving mass, momentum, and heat transfer [23]. A brief discussion on nucleation and bubble growth processes is included here.

2.1.4.1 Nucleation

Nucleation is an important concept in various processes such as boiling, crystallization, and foaming. The concept of nucleation was first proposed by Volmer and Weber [35] in 1926 and has been extensively studied and reviewed by others [13-15, 35]. Nucleation is the process of formation of small bubbles of a different phase either in a homogenous liquid, which is termed homogenous nucleation, or at the interface between two phases, which is termed heterogeneous nucleation [16]. The classical nucleation theory is based on the Gibbs free energy (ΔG_n) required to form a single bubble of volume V_g in mechanical and thermodynamic equilibrium with the surrounding liquid. The work involved in the formation of a new phase consists of the positive work to create the new surface and the work by molecules diffusing into the bubble. The bubble so formed is called a critical cluster containing 'n' molecules of radius of r_c.

For negligible volume changes, the free energy can be given as [36] –

$$\Delta G_n = 4\pi R^2 \sigma + \frac{4\pi}{3} R^3 (P_G - P_L) \tag{2.12}$$

where

R is the radius of the bubble,

σ the surface tension

P_G is pressure inside the gas

P_L is the pressure in the liquid phase.

The criterion for bubble survival is the maximum free energy; thus the critical radius of the bubble can be calculated by differentiating equation 2.12 and equating to zero leading to:

$$r_c = \frac{2\sigma}{(P_G - P_L)} \tag{2.13}$$

On the other hand, if the bubble is only slightly larger than the critical size, thermal fluctuations can cause it to fall into a subcritical state or collapse [37].

For the case of polymeric foaming, it has been shown that the classical nucleation theory does not work because it does not account for free energy changes caused by changes in free volume and the potential energy changes due to changes in distance between polymeric chains [15]. Several attempts to modify classical nucleation theory to account for polymeric systems have been made [13-16,]. Colton and Suh [13] studied heterogeneous bubble nucleation in polymeric melt in microcellular foams, and modified the classical theory to account for change in the potential energy of the system. They claimed that the decrease in potential energy decreases the energy needed for nucleation and needs to be accounted for in the free energy term of the classical theory. Other studies included similar modifications to account for the presence of solid particles, which enhance heterogeneous nucleation [14], for supersaturation of the blowing agent [15] and for the effect of dissolved gas in polymeric solutions on surface tension [16].

It is well established in the boiling literature that the presence of crevices and depressions on solid surfaces harbor microbubbles to serve as seeds for nucleation [14,17]. Ramesh et.al [19], showed the existence of these microbubbles on rubber particles added to

polystyrene as nucleating agents. Recently, Feng and Bertelo [12] proposed a nucleation model based on this finding and on the work of Ramesh et. al. [19].

Ramesh et.al. [18, 19] mathematically modeled the nucleation mechanism based on the hypothesis that several micro-voids exist on the surface of the nucleating agents and that only the largest micro-voids are able to survive. Using a log normal distribution to model the size of the nucleating agents, they assumed that each particle contributed to a single micro-void. The size of the micro-void is influenced by the size of the nucleating agent and is dependent on the size distribution of the nucleating agents.

Feng and Bertelo[12] showed several inconsistencies with Ramesh's model [18, 19] in terms of their method for the determination of the critical radius of the initial bubbles and the fact that a log normal bubble distribution was assumed. They argued that the size distribution of nucleating agents should follow a truncated log normal pattern. Drawing on some of the assumptions made by Ramesh et. al. [18, 19] such as the size of the nucleated bubble, the size of the particle and that there is a critical radius of the initial bubble which determines its survival, they derived a nucleation model. Unlike Ramesh et. al. who calculated the critical radius by a force balance between the bubble pressure and the resistive forces of surface tension, the critical radius was determined in a manner similar to that used for bubble formation on a rough surface in classical nucleation. In their work, they modeled a micro bubble trapped in a conical surface crevice or depression (as shown in Figure 2.5) which expands towards the surfaces as the pressure is

reduced in the foaming process. A bubble with radius, r, greater than the critical radius, r_c, as in classical nucleation theory would survive and grow.

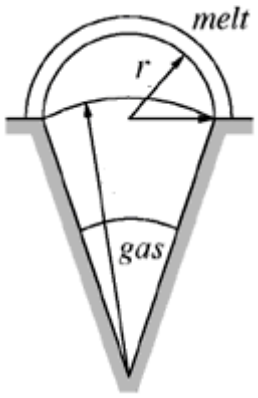

Figure 2.5 Nucleation of bubble from a pre-existing micro void [12]

The concept that a conical cavity as discussed by Feng and Bertelo [12] serves as a starting point for bubble growth is relevant to the current study. Paperboard has pores of several shapes and sizes as discussed in Section 2.3, which could serve as similar starting points for bubble growth.

2.1.4.2 Bubble Growth

In contrast to nucleation, bubble growth is well defined, while still remaining a complex process involving mass, momentum, and heat transfers. For the case of polymeric foams, the growth process should also account for transient interactions between different bubbles and for the changing shape of bubbles. Two types of bubble growth processes have been studied in the literature: with and without mass transfer. For the case without mass transfer, the bubble growth is due to the pressure difference between a gas bubble and the surrounding liquid [23].

The literature supports the idea that the bubbles or cells in foams are spherical but there are two widely used assumptions for bubble growth – the infinite dilute assumption (IDL) and thin boundary layer (TBL) assumption. IDL is the case when the dissolved gas is assumed to be infinitely diluting; thus the driving force for mass diffusion is very small. The TBL assumption implies that the variation in concentration field for a bubble growth process is limited to a thin shell around the bubble. Barlow and Langlois [38] were one of the first to treat the diffusion of dissolved blowing agent from the liquid for a mass transfer controlled system. They considered the system to be isothermal and used the Henry's law equilibrium relationship for low diffusivity boiling agents. Street et. al. [39] studied bubble growth in a viscous liquid. Using a non Newtonian – power law model, they considered the effects of heat, mass and momentum transfer to study the influence of parameters such as viscosity and shear thinning. Other studies on diffusion induced growth have been pursued in Newtonian, power law and viscoelastic melts [20-22]. The interactions between bubbles are either neglected or are taken into account.

Shafi and Flummerfelt [37] considered a nucleated bubble to be one which reaches a supercritical state where any thermodynamic fluctuations do not allow the bubble to return to a subcritical state. Shafi et. al., [37] further expanded on their work to determine the initial conditions of the bubble and developed a model which predicts simultaneous nucleation and bubble growth. Using an influence volume approach, they assumed that within the influence volume the nucleation process would be limited due to a reduction in the concentration of the gas, while outside the influence volume the concentration would

be high enough for nucleation to occur. Within the influence volume, there would be bubble growth until all the dissolved gas is consumed. They concluded that the most influential parameters in the final bubble size distribution depend on the nucleation process with growth dynamics playing a secondary role [37].

Amon and Denson [24] studied the depletion of gas from a polymeric melt as the bubble expands. The bubble in such a case cannot exceed a certain equilibrium size due to a finite supply of dissolved gas and also due to the fact that there is much less liquid to be stretched. This is especially true during the final stages when bubbles are separated by thin films. Combining the equations of bubble growth with macroscopic flow parameters such as pressure and velocity, they pursued a mathematical analysis. Arefmanesh and Advani [21] relaxed the assumption made by Amon and Denson that an average bubble will represent all the bubbles in the foam and solved for the growth of many closely spaced bubbles under isothermal conditions.

Venerus [23] et. al., analyzed the growth of a single spherical gas bubble surrounded by a viscoelastic liquid under isothermal conditions. Venerus et. al's work represents a classic case of diffusion-induced bubble growth in a viscoelastic liquid. For a polymer foaming system, the gas is dissolved in the liquid and diffuses into the nucleated bubble. Venerus et. al., modeled this with Fickian diffusion with the growth of a bubble being caused by the concentration difference of the diffusing solute in the liquid melt. They assumed the gas in the bubble to be in-viscid, ideal, with uniform bubble pressure, and neglected the inertial effects. They also assumed the liquid surrounding the bubble to be incompressible

with rheological properties independent of concentration. Considering a single component system with binary constitution of the volatile species and the viscoelastic fluid they tracked the bubble growth. They validated the assumptions of infinite dilute solution and the thin boundary layer for viscoelastic fluids over a range for which these are valid, and determined the importance of nonlinear viscoelastic systems for diffusion-induced bubble growth systems.

Feng and Bertelo[12] developed a numerical scheme based on Venerus et. al.'s [23] bubble growth model and studied the effect of viscoelasticity on bubble growth. They combined their nucleation model with Venerus et. al.'s, bubble growth model to predict the final cellular structure of the foam. The governing equations for the bubble growth developed by Venerus et. al., and employed by Feng and Bertelo are given below:

Momentum equations:

$$P_g - P_a = \rho\left(R\ddot{R} + \frac{3}{2}\dot{R}^2\right) + \frac{2\sigma}{R} + \frac{4\mu_s \dot{R}}{R} - 2\int_R^\infty \frac{\tau_{rr} - \tau_{\theta\theta}}{r} dr \qquad (2.14)$$

where

$P_g(t)$ and $r(t)$ are instantaneous bubble pressure and radius,

σ is the surface tension,

μ_s is Newtonian viscosity,

τ_{rr} and $\tau_{\theta\theta}$ are viscoelastic normal stress components.

Each of the terms on right hand side represents resistance to bubble growth due to inertia, surface tension and viscoelastic normal stresses respectively. $\ddot{R}$ and $\dot{R}$ represent the time derivates.

Mass balance for the bubble:

$$\frac{d}{dt}(P_g R^3) = 3DAR^2 \frac{\partial c}{\partial r}_{r=R} \tag{2.15}$$

where

A is the constant for isothermal ideal gas where $P_g = A\rho_g$

D is diffusion constant

C is the concentration at time *t*, and radius, *r*.

Mass balance for gas in melt:

$$\frac{\partial c}{\partial t} + v_r \frac{\partial c}{\partial r} = \frac{D}{r^2}\frac{\partial}{\partial r}\left(r^2 \frac{\partial c}{\partial r}\right) \tag{2.16}$$

Lastly the Oldryod B constitutive equations [12] for non linear viscoelastic normal stresses are given as:

$$\begin{aligned} \tau_{rr} + \lambda\left(\frac{d\tau_{rr}}{dt} + \frac{4R^2\dot{R}}{r^3}\tau_{rr}\right) &= -\frac{4\mu_p R^2 \dot{R}}{r^3} \\ \tau_{\theta\theta} + \lambda\left(\frac{d\tau_{\theta\theta}}{dt} - \frac{2R^2\dot{R}}{r^3}\tau_{\theta\theta}\right) &= \frac{2\mu_p R^2 \dot{R}}{r^3} \end{aligned} \tag{2.17}$$

where

λ is the polymer relaxation time, and μ_p is the polymer viscosity.

The dimensionless form of these equations is solved with the appropriate boundary conditions. Feng and Bertelo [12] accounted for growth of a bubble in a shell with a finite amount of gas and where the bubbles exist in close proximity, and analyzed the role of viscoelasticity in foaming.

2.1.5 Biodegradable Foams

The current study focuses on foaming traditional polymers such as LDPE on paperboard but keeps open the possibility of foaming biodegradable polymers in a future application. A brief discussion of different biodegradable foams is included here. Biodegradability is defined as the ability of a polymer to decompose naturally over a defined period of time by environmentally occurring processes [2]. Biodegradable polymers are materials made from renewable resources considered environmentally friendly, in contrast to traditional petroleum based polymers. Examples of bio-based polymers include starch, proteins, natural fibers and cellulose [40, 41]

The primary interest in biodegradable foams arise from two reasons - the increasing cost of resins made from oil and natural gas, and the environmental concerns of traditional foams[2]. One of the main advantages of biodegradable foams is its source of raw materials, which is renewable biomass feedstock [2, 40, 41]. These feedstocks reduce the dependence on oil and also contribute less to CO_2 emissions helping to achieve emission standards specified by the Kyoto protocol [40, 41]. The other advantages are accelerated degradation in landfills thus freeing up land space for other uses. On the other hand,

biodegradable foams have problems associated with additives, plasticizers and modifiers, which could wash off from landfills into groundwater. They are also usually sensitive to moisture and must employ processes that involve low shear rates.

Several successful attempts at foaming biopolymers such as poly-caprolactone and polylactic acid foams [42-46] have been made. Several scientists have worked on the extrusion of starch foams [47-51]. The use of wood fiber in foaming has also been investigated [52]. Table 2.1 lists the different biofoams used and their applications. Currently about 10% of the polystyrene loose fill market is replaced by starch foam [53] which is also gaining a lot of interest for different automotive applications [40]. Current technology limits the manufacture of bio-foam to sizes in the range of 50-100μm. Microcellular foaming (<50 μm cell size) which could give an overall foam thickness of over 10 mm and a width above 1 meter still faces technologic challenges [2].

Table 2.1 Biodegradable plastics & applications [2]

Biodegradable plastics	Foams/fills	Application
Starch	Loose fill foam	Packaging
Poly-lactic acid (PLA)	Sheets	Thermo formable sheets
Polyvinyl alcohol (PVOH)	Water soluble foam or film	Packaging
Polycaprolactone (PCL)	Foamable	Packaging
Ethylene vinyl alcohol (EVOH)	Water soluble foam or film	Oxygen barrier, multi layer packaging and foams.

2.2 Extrusion Process

During extrusion coating a thin film of molten thermoplastic polymer is pressed on to paperboard through a slot die [54, 55]. Extrusion coating is a well studied process and is widely used to make several products such as liquid packaging, flexible packaging, board packaging, industrial wraps, industrial products, sacks etc. [66]. In contrast to traditional foaming, the present study offers a unique approach to foaming polymers on a predetermined porous substrate. The manner in which the polymer bonds with the paper is important in the foaming process on paperboard. As the moisture vaporizes during foaming, pressure is built up inside the board. The pressure buildup is determined by the degree of adhesion of the polymer to the board. Extrusion also affects the interfacial properties which can play a role in the foaming process. Parameters such as line speed, extruded temperature profile, chill roll temperature and press roll pressure can be important in the present study [54, 55].

2.2.1 Adhesion properties

Adhesion between paper and polymer depends on several factors such as the melt temperature, extrusion speed, die height, nip pressure etc. Adhesion occurs both by both mechanical and chemical bonding [56]. Mechanical adhesion dominates for porous substrates such as paper or paperboard where the polymer physically penetrates the fibers or the pores [56]. Chemical bonding dominates for non-porous substrates where the oxidation of polymer or the pretreatment of substrate allows the formation of chemical

bonds. Several factors lead to good adhesion of the polymer with the paperboard. Higher surface tension between the polymer and paper promotes adhesion. Higher coat weights also increase adhesion [56, 57]. This is because higher coat weights leads to a closer contact between the polymer and the fiber surface. This also increases the amount of polymer which gets nipped between the voids of the fibers. An increased weight also enables better heat transfer to the paperboard [57].

A higher melt temperature also promotes better adhesion. Although LDPE is non-polar in nature, the melt oxidizes in the air gap between the die and the nip to form oxidized polar functional groups [54]. Oxidation leads to the formation of stronger bonds between the paper and the polar surface groupings. A higher melt temperature causes better oxidation. The induced polarity (due to oxidation) improves adhesion especially on non-porous substrates. Figure 2.6 shows the better bonding obtained at higher melt temperatures compared to the poorer bonding at lower melt temperature seen in Figure 2.7. Figure 2.8 shows the effect of melt temperature on adhesion with and without ozone. Ozone helps improve adhesion at lower melt temperatures [57, 58].

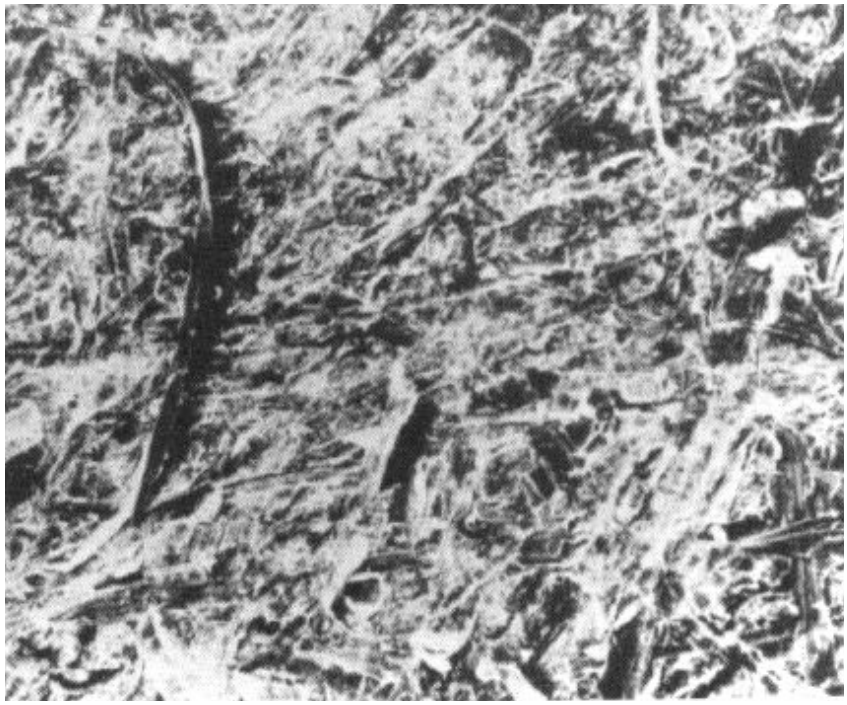

Figure 2.6 High temperature coating process produces good bonding on paperboard [58]

Figure 2.7 Low temperature coating process produces poor bonding on paperboard [58]

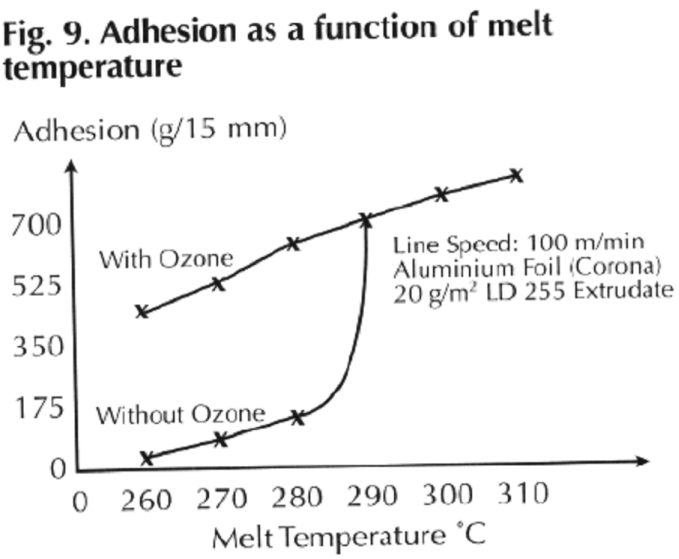

Figure 2.8 Effect of melt temperature on adhesion [58,59]

Line speed is the other factor which plays an important role in adhesion and determines the residence time of polymer in the air gap [57]. The residence time directly relates to the degree of oxidation that the polymer melt undergoes. A faster line speed leads to lower oxidation but has the advantage of faster processing of the material. At very high line speeds (low residence times), the degree of oxidation deteriorates to a point where there is not enough time for the oxidation process to be initiated, and the adhesion drops [59].

Figure 2.9 illustrates this point [57]. Several surface treatment technologies can be applied to improve adhesion at higher speeds [60-62]; one of the widely used techniques is ozonation.

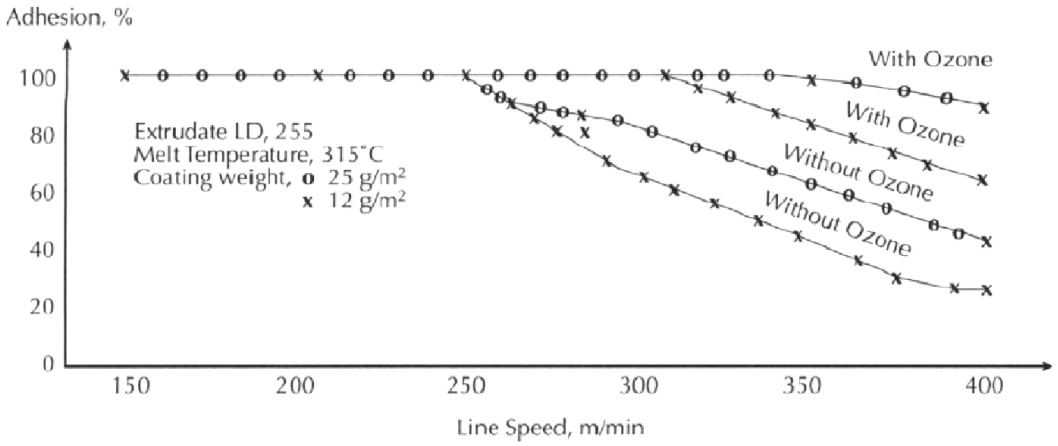

Figure 2.9 Effect of line speed on adhesion [58,59]

2.2.2 Effect of interfacial properties due to extrusion

The extrusion process also affects the properties of the polymer and paperboard at the interface. Furuheim et. al. [63-65] conducted a phase structural analysis of polyethylene on extruded paper. Using AFM and SEM techniques they characterized the polyethylene surface at the interface. The extrusion process involves shear forces and adhesion to fibers which result in orientation of the polymeric chains [63]. The shear forces affect the orientation of the polyethylene to form monoclinic crystalline regions. Other processes such as corona discharge treatment before the extrusion cause formation of hydro-peroxide bonds which make the surface of paper more reactive to the polymer. The cooling rate also affects the strain rate at the interface of the paper and polymer due to differences in the thermal expansion coefficients of materials [66].

A polymer extruded on a board experiences a number of changes to its structure. Furuheim et.al. [64], concluded that the properties of paper used also impact the final polymer structural properties. They noted that a large fraction of the monoclinic crystalline phase was present at the interface of the paper and polymer. Their SEM studies also revealed the presence of open flat bubbles which they hypothesized to be caused by the evaporation of water from the paper due to heat flow during the extrusion process. Figure 2.10 illustrates the open flat bubbles on LDPE and HDPE surfaces extruded on paperboard. Other process parameters such as the load in the press rolls, the surface energy of paper, and the adhesive properties of the polymer play key roles in determining the relative fraction of monoclinic crystalline regions at the interface.

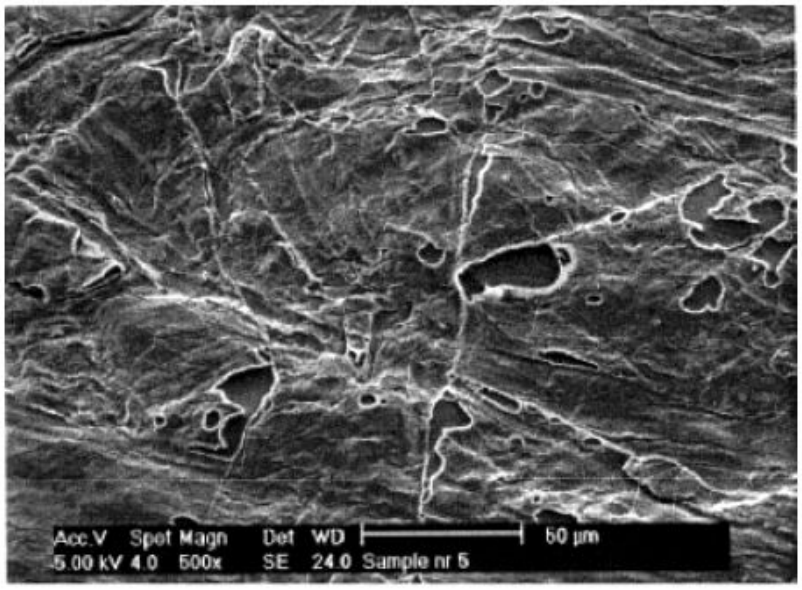

(a)

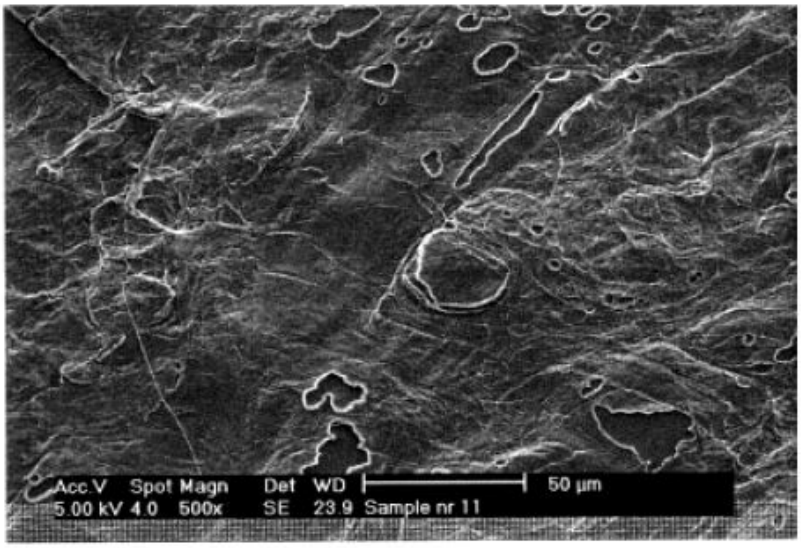

(b)

Figure 2.10 SEM images of inside surfaces of polyethylene coating on steam box treated paper. Imprints of flat collapsed cellulose fibers and bubbles are seen. (a)– LDPE, (b) – HDPE (425X) [64]

2.2.3 Low density polyethylene in extrusion

The current study employs low density polyethylene. Polyethylene offers several advantages for film application such as light weight, low cost, flexibility (low modulus), toughness, chemical resistance, ease of sealability etc. [67]. Plastics, in general, have inert nonporous surfaces with low surface tensions, causing them to be non-receptive to bonding with substrates [60]. LDPE is known to have excellent adhesion to kraft paperboard. Polyethylene and polypropylene have very low surface tension and often need surface treatment steps to improve adhesion [68-70].

2.2.4 Chemistry

Low density polyethylene (LDPE) is a molecule with a carbon back bone and several long and short branches as shown in Figure 2.11.

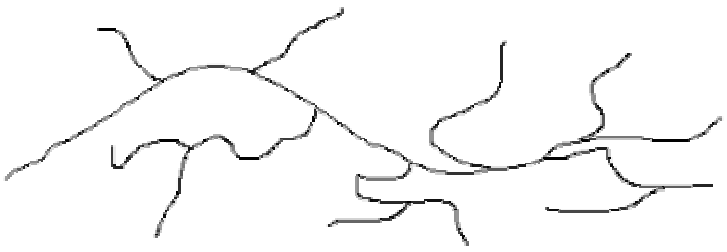

Figure 2.11 Low density polyethylene molecule (LDPE) [71]

LDPE contains both crystalline and amorphous regions [67]. The crystalline region consists of spherulites where the polymeric chains form an organized structure. The short branches in LDPE lead to the formation of amorphous regions. The average molecular

weight (Melt Index), crystallinity (density) and molecular weight distribution (MWD) primarily determine the properties of a low density polyethylene [67]. The molecular weight determines the physical properties such as tear, strength, tensile properties, impact and toughness. The density determines the crystalline properties of the polymer. The MWD distribution affects the viscosity of the polymer. The melt index and the density of LDPE are two properties important in the extrusion process [56].

2.2.5 Melt Index (MI)

This parameter determines the ease with which a resin will flow. The Melt Index is also inversely proportional to the molecular weight of the polymer [72]. At a constant density and molecular weight distribution, a decreasing MI improves melt strength but decreases processing ability, drawdown and die swelling [67]. The solid state properties, on the other hand, show an increase in tensile strength, impact strength and heat sealing ability [67]. A lower MI also gives better tensile strength properties to the end product but leads to processing difficulties due to the higher viscosity of the polymer. It also improves melt strength but reduces the ability to draw down to a thin gauge. Higher MI would mean easier flow characteristics, and hence lower pressures and power needed during processing. The heat sealability also increases at higher MI due to lower viscosity [67].

2.2.6 Density

LDPE density determines barrier and heat seal ability properties. The higher density material leads to better barrier properties such as grease resistance and moisture vapor transmission rate (MVTR) as shown in Figure 2.12. An increase in coated weight also improves barrier properties (decreases MVTR) [56].

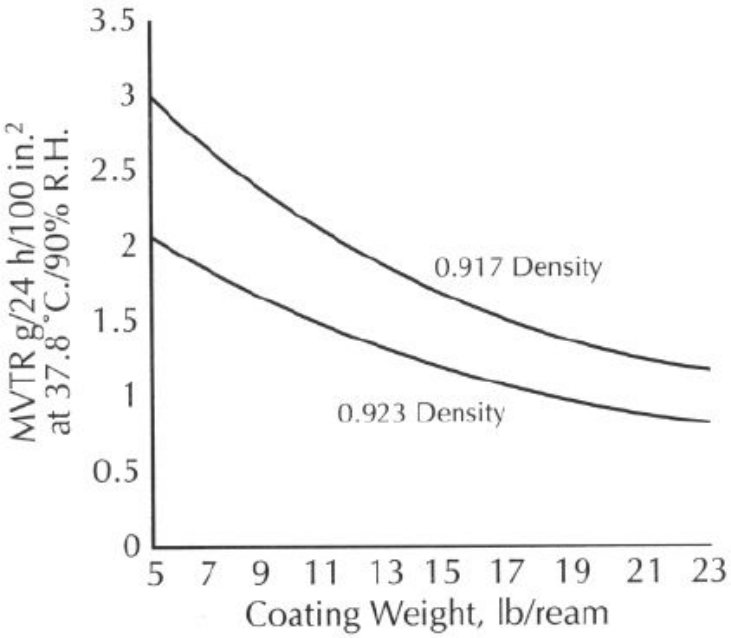

Figure 2.12 Moisture vapor transmission rate vs coating weight [56]

At a constant molecular weight distribution, decreasing density would not have significant effects on the melt properties. On the hand it would have an effect on the solid state properties by decreasing stiffness, increasing impact strength, improving permeability, improving heat seal ability etc. [67]. The density of the extruded resin is always lower than the initial polymeric density. This is due to the quench cooling action

of the chill roll which prevents crystalline growth. To compensate for this decrease in density, a higher resin density is used to begin with [67].

2.3 Paperboard – Structure and transport properties

A porous medium is defined as one whose solid volume is distributed in a space larger than itself [73]. Paper is classified as a consolidated porous medium due to fibers being bonded together in a continuous fashion. Paperboard forms the substrate in the present study and thus plays an important role in determining the final foam characteristics. This section discusses the different fundamental properties of paperboard which could be important to the foaming process.

A paper sheet contains different sizes and shapes of interconnected passages and pores which allow transport of fluids through the sheet [74]. A scanning electron microscope picture shown in Figure 2.13 illustrates the porous structure of paperboard. The porous nature of the paper makes it very useful for a variety of products such as in paper towels, filter paper, blotting papers, sanitary tissues, writing paper etc [73]. The porous nature also enables better bonding with the polymer during extrusion in the current work. The sheet porosity also directly relates to the permeability or transport rate of fluids inside [74]. The dry sheet structure consists of fibers, moisture and gas filled pores. The volume fraction of each component, continuity, tortuosity and pore size distribution determines its properties. The tortuous path inside the sheet depends on the shape of the pores as

shown in Figure 2.14. An ideal pore would have a tortuosity value of one implying a straight pore while a more tortuous path would have a higher value [74].

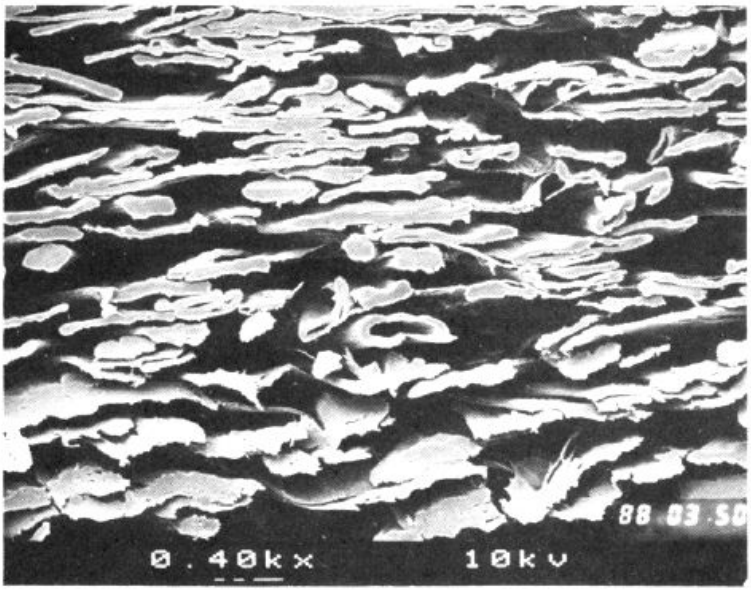

Figure 2.13 Scanning electron micrograph of paper cross section [75]

Porosity also directly relates to permeability, which determines the paper sheet transport resistance. The pore size and permeability depend on a host of factors such as the degree of refining of the fibers, the presence or absence of fillers, the type of coating applied to the sheet, the amount of wet pressure applied to the sheet, drying conditions etc [73]. The structure of the sheet also depends on the number and type of fibers in the sheet formation process. Wood fibers primarily consist of cellulose, hemicellulose and lignin [76]. The lignin helps to "cement" the components together [76]. Two primary types of wood fibers widely used in papermaking are softwood and hardwood. Figure 2.15 illustrates the cell structures of these two types of wood fibers [77].

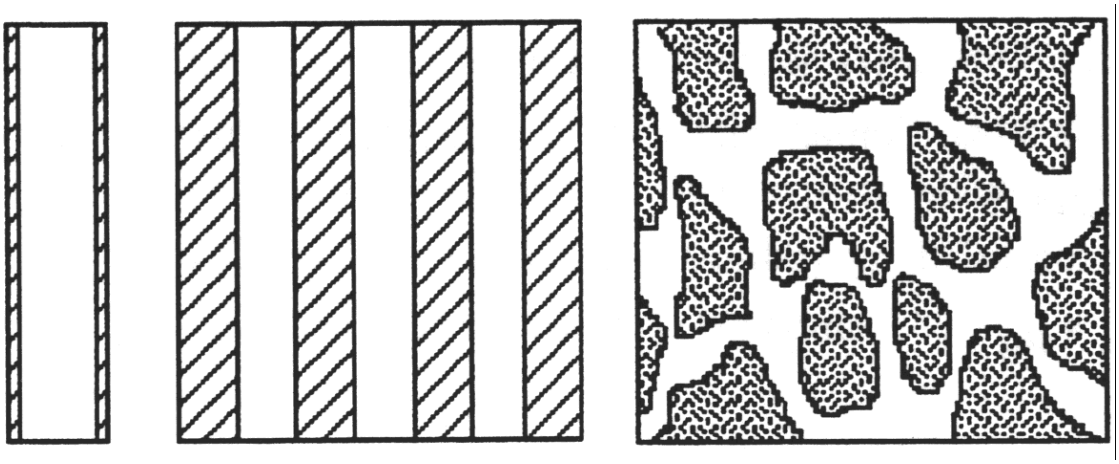

Figure 2.14 Cross sections of a porous media: a) an ideal pore, b) parallel ideal pores, c) a natural or synthetic structure [78].

Softwood or gymnosperms have longer fibers than their hardwood counterparts. Softwood (SWD) fibers usually have fiber length between 2.5 – 7 mm and are 25-60 μm wide [76]. The primary component of softwood is the longitudinal tracheid which accounts for 90-95% of the wood fiber. The function of tracheids is to move fluids through the tree [77]. The rest of the fiber accounts for the ray cell (5-10%) and resin cells between 0.5-1.0% [76]. The ray cells are washed out after pulping [77]. Thus a softwood pulp primarily consists of tracheids, which are arranged so that their ends overlap to form well-aligned radial rows.

Hardwoods, on the other hand, are composed of shorter fibers. Hardwoods are also called angiosperms and are deciduous trees that have a more complex structure than softwood. In addition to the tracheids, rays and resin cells, hardwoods contain vessel elements and libriform fibers [77]. The vessel elements cause the hardwood fibers to be shorter. A hardwood fiber is about 1-1.5 mm long and has a lower percentage of open area as

compared to softwood fibers [77]. The shorter fibers cause the paper sheet to be much smoother but decrease its strength properties [76].

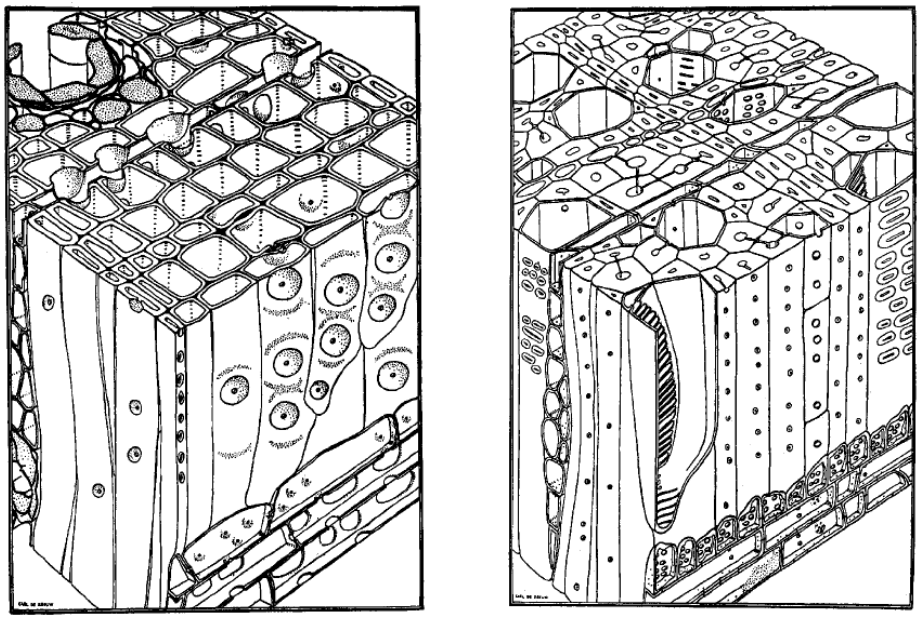

Figure 2.15 Cell wall – Softwood (left), Hardwood (right). [77]

2.3.1 Refining and its effects of fiber bonding

The process of refining causes cyclic deformation of cellulose fibers, and is performed by a set of rotating bars or rotating surfaces. Refining is widely used and is well studied in the literature [79-83]. In the present study, two different refining levels were used. The numbers of fibers that get refined depend on the consistency of the pulp suspension. For lower consistency suspensions, refining principally occurs at the bar edges; higher consistency stock gets refined more as individual fibers and the action primarily occurs

on the fiber surface. Refining is a complex process with different actions taking place at different points of the pulp suspension.

Refining exposes more fiber surface, thus increasing the water absorption capability of a fiber [84]. The primary effects of refining are known to be irreversible [85]. Although refining has been a topic of study for several decades, there is no universally accepted theory which relates the process to structural fiber cell wall changes [85]. Three main effects of refining have been observed [85] –

1. Creation of new surfaces
2. Creation of new particles
3. Structural damage and modification.

Refining causes breakage of covalent and hydrogen bonds [82]. Fibrillation causes formation of new internal and external surfaces. Fiber cutting or splitting of loose ends leads to creation of new particles such as fines and crills. New particles are also created through dissolution or cutting away of individual polymers from the cell wall [82]. The third major effect of refining is structural damage and fiber modification. This is due to cutting of the fibers and lamellae, partial cleavage of the cell wall, the generation of axially compressed zones, creation of invisible weak zones and changes in crystalline sites and micro-fibril orientation.

Refining action is measured as freeness or the ability of a suspension to drain. A low value of freeness would mean a lower drainage or better bonding between fibers.

Freeness also serves as a measurement factor for fiber swell and the surface area of fiber. The effects of refining on the strength properties of paper sheet were studied by making handsheets and are shown in Figure 2.16 [74]. Water acts as a swelling medium in refining. Increased refining cause fibers to swell thus increasing the amount of water present inside the fibers. Although freeness is a widely used parameter in the industry, it is a pulp-specific property and cannot be used to correlate the different fibers, pulp types or pulping techniques.

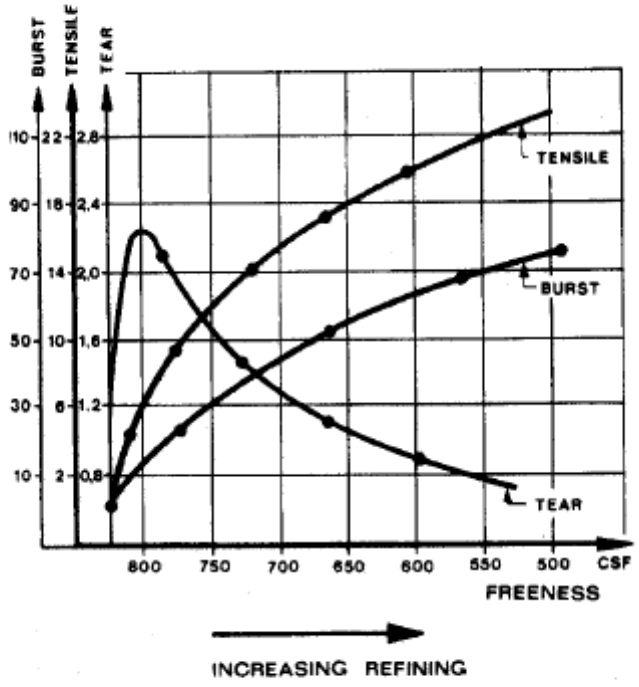

Figure 2.16 Changes in strength properties with refining [74]

At low degrees of beating, swelling enhances the strength of the resulting paper sheet [86], but at high degrees of beating, swelling can actually correlate with a decrease in strength. The freeness measurements also are not consistent at the high refining end of

the spectrum. The BET surface area measurement is another technique used to relate refining effects to fiber surface area [86]. BET is a dry technique and hence does not account for the swollen structure of fiber during the pulping process [87].

2.3.2 Moisture in paper

Paper readily absorbs water since wood fibers are hygroscopic. The moisture content in the sheet can be calculated as the ratio of absorbed water to the mass of oven dry paper. Moisture in the paperboard depends on the relative humidity and temperature of the atmosphere around it. Relative humidity (RH) determines the amount of vapor in air and is calculated as the ratio of vapor pressure to the saturation vapor pressure [88]. Moisture in paper can vary between extremes. The water retention value, WRV, which is the amount of total water retained by wet pulp, can range from 50 to 200% depending on the type and degree of beating of the pulp [89]. Water in paper can be present in one of the following forms [90]-

1. Free water
    a. Inter-fiber free water in the pores between fibers
    b. Intra-fiber free water in the lumen of fibers
2. Bound water
    a. Freezing bound water in the pores of fiber wall
    b. Nonfreezing bound water, chemically bonded to the hydroxyl and carboxylic acid groups in fibers

A more detailed discussion of the moisture content and different types of water is given by [91]. Figure 2.17 illustrates the different fractions of water present inside the paperboard at different levels of moisture content.

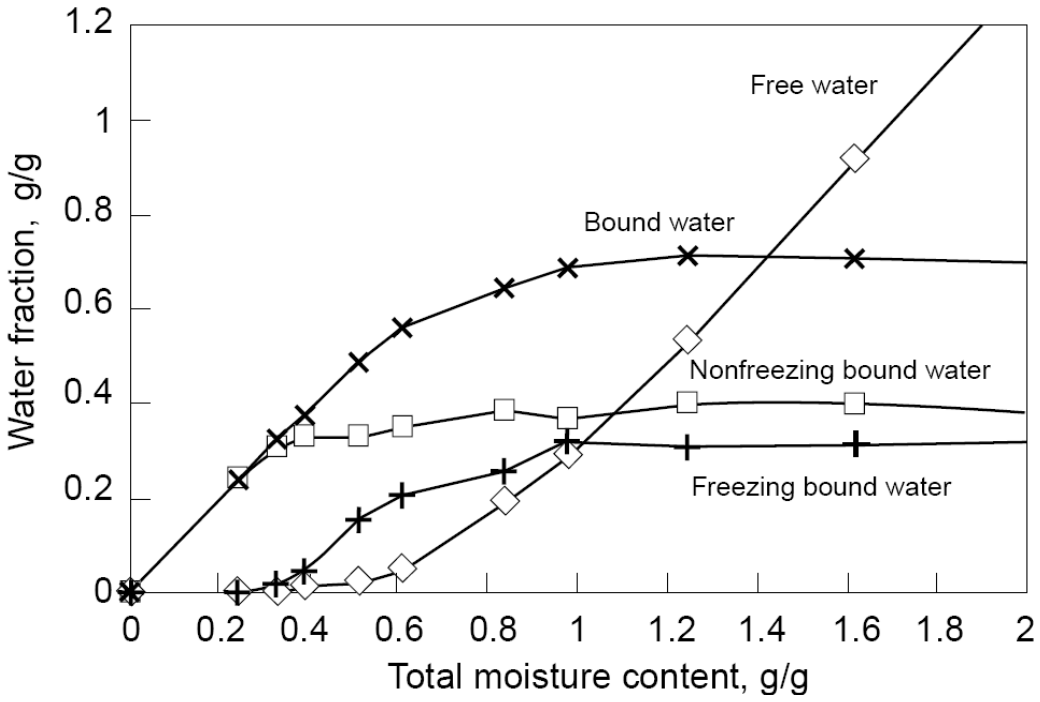

Figure 2.17 Relative proportions of different free and bound water fractions vs. moisture content. Total moisture content on the x-axis is water mass per dry solids mass. Symbols: diamonds = free water, x = total bound water, squares = nonfreezing bound water, plusses = freezing bound water [88]

Paper loses most of its free water at about 50%-60% solids content during drying [91]. At moisture levels of 20%, all the water present is bound water. The reduction in moisture during drying decreases the level of fiber swelling due to closure of pores in the fiber cell wall. The water molecules thus get absorbed onto the inner and outer surface as a molecular layer. The moisture contents in the current study were maintained between 6 and 8% percent and hence all the moisture would be present as bound water. Several techniques have been used to determine the amount of bound and free water in

paperboard. These include Differential Scanning Calorimetry (DSC) [92, 93], solute exclusion [91], and bound water measurements using tritiated water [85]. Typical bound water values as measured by several researchers are shown in Table 2.2.

Table 2.2 Typical values of bound water [85]

Material	FSP[1] ($g\ g^{-1}$)	Interfacial water ($g\ g^{-1}$)	Determination	Method	Reference
Sulfite pulp		0.17	Bound water	Thermal expansion coefficient	Goring 1977
Cotton, bleached Spruce, bleached Poplar, bleached Straw		0.05–0.07	Monolayer coverage	Water vapor adsorption	Hernadi 1984
Cotton, rayon		0.04–0.19 0.14–0.31	Bound water Total non-freezing water	DSC	Magne et al. 1947
Unbleached kraft	1.35	0.34	Non-freezing bound water	DSC	Maloney et al. 1998
Cotton	0.36	0.24			
Microcrystalline cellulose		0.20			
Hardwood pulp		0.21	Bound water	DSC	Nelson 1977
Softwood pulp		0.26			
Whatman #1 filter paper		0.27			
Cotton yarn		0.14	Non-freezing bound water	DSC	Nakamura et al. 1981
Cotton lint		0.18			
Wood cellulose		0.19			
Cotton	0.50	0.15	Maximum bound water value	NMR	Carles and Scallan 1973
Cotton	0.45	0.23			
Sulfite pulp	1.34	0.30			
Kraft pulp	1.66	0.33			

FSP, fiber saturation point.

Bound water can be present on the fiber surface as a monolayer or as multiple layers of adsorbed molecules. For the case of multiple layers of molecules, the mobility of the first layer is severely restricted and the successive layers become less bound [85, 94]. Several studies have focused on estimating the amount of bound water which directly bonds to the fibers surface as a monolayer. Walsh and Banerjee [95, 96] developed a new technique using tritiated water and estimated the amount of bound water present as a monolayer in wet pulps to be 10%. The monolayer coverage was found to occupy an area of 183 m^2/g. Other studies have reported similar values [97, 98]. In comparison, the present study employs a dry paper sheet with 6-8 % moisture content. Thus, it is fair to

assume that the moisture inside the sheet is present as a monolayer adsorbed onto the fiber surface.

2.3.3 Moisture Transport

Fluid transport in porous media has been a topic of study for several decades. As discussed earlier, moisture transport inside the paperboard plays an important role in a variety of processes. In the present work, the moisture transport serves as the driving force for the foaming.

Moisture transport involves two different processes – sorption and transport [99]. Sorption is the process of attaining a steady state moisture content or equilibrium state with the surrounding [99]. Transport on the other hand is the rate at which moisture travels within the cellulose network. In the present case, impermeable polyethylene is extruded on both sides of the paperboard thus exposing only a small fraction of the paperboard surface (the edges of the board) to the environment. The process of board conditioning to attain 6-8% moisture occurs by sorption. During the foaming process, moisture vaporizes leading to a pressure build up inside the sheet. This drives the transport process within the paper network and into the polymeric layer. The pressure build up occurs because the flow is restricted between the two polymeric layers that sandwich the paperboard. A good example of vapor flow in paperboard is in the paper drying process. Although the current case differs from the processes observed in drying in several ways, a discussion on the transport mechanisms in drying will lay out the

fundamental principles that will help understand the transport mechanism that applies here. Vapor transport in paperboard can occur by diffusive or convective processes.

2.3.4 Water Vapor Transport - Paper Drying

Two drying processes are well known in the industry - conventional and high intensity [100]. For the case of conventional drying, moisture removal is dominated by vapor diffusion. For high intensity drying, the moisture removal is dominated by convective bulk flow [100]. Convective bulk flow in conventional drying may dominate if a pressure differential exists across the sheet [100]. The action of water and vapor leaving the sheet leaves void spaces in the sheet, which affect the sheet porosity and pore size distribution. The fluid flow thus takes a continually changing tortuous path inside the sheet. Several models have been proposed to account for the different transport processes inside the paper sheet for both conventional and high intensity drying.

For conventional drying, fluid flow occurs via different mechanisms such as liquid capillary flow, diffusion and bulk vapor flow [101]. Liquid flow occurs via capillary flow if a pressure differential is created by a non uniform pore structure of the sheet. Darcy's law controls this process. Vapor concentration gradients due to non-uniform temperature across the sheet as explained by Fick's law are responsible for the diffusive process. Two types of diffusive processes have been observed. Stephan diffusion dominates and is caused by a gradient in the vapor partial pressure. Knudsen diffusion, the other diffusive process, occurs due to the small sizes of the capillaries and pores. The diffusive processes

hence primarily occur when the total pressure is constant across the web i.e. equal to atmospheric pressure [101].

The convective bulk flow or the laminar vapor flow process on the other hand is due to a pressure gradient across the board, i.e. the pressure inside the board is higher than the atmospheric pressure [102]. This usually occurs at temperatures higher than 100^{o}C [101]. The pressure inside the sheet increases when the rate of vaporization exceeds the diffusive transport rate. The vapor flow in such a case can be explained by Darcy's law [101]. Since pressure builds up inside the sheet in the current case, convective bulk flow dominates. The process of convective bulk flow in drying was first proposed by Holm, et al [102]. Ahrens, et al. [103] studied the drying of laboratory sheets at high temperatures and pressures and observed a dramatic increase in drying rates as the sheet temperature increased as illustrated in Figure 2.18 [103].

They reasoned that this increase in rate was due to a change in the transport mechanism from diffusive to convective and called the process high intensity drying. Impulse drying is a form of high intensity drying where the wet sheet is simultaneously heated and pressed for a very short period (e.g., 5-35 milliseconds) in a heated press nip. Burton verified the process of convective vapor flow for the case of impulse drying [104]. For vapor convection to occur, a pressure gradient must be present. Ahrens and Burton measured vapor phase pressures at the hot side of the sheet during their experiments [104, 105]. Ahren's pressure data is shown in Fig. 2.19 [105].

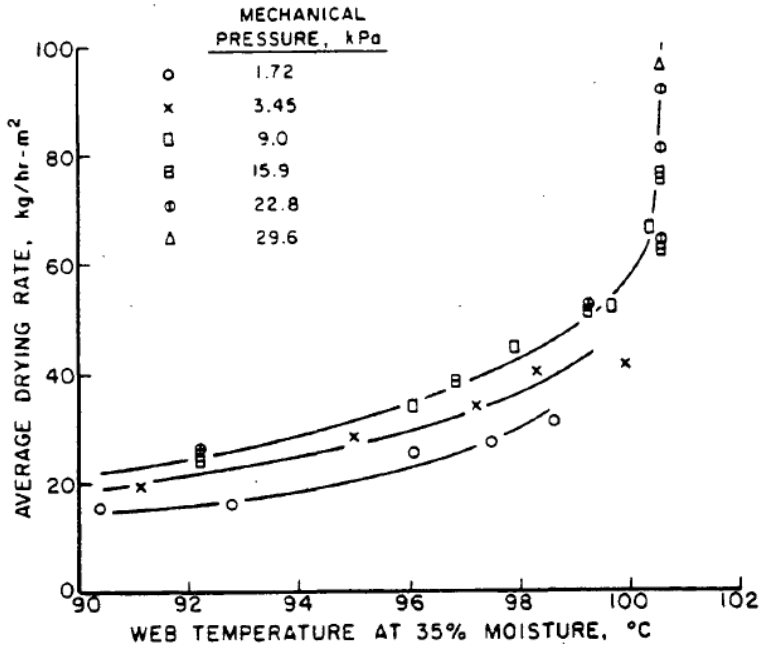

Figure 2.18 Correlation of average drying rate with typical web temperatures for unbleached southern softwood Kraft handsheets (42 lb/1000 ft^2 basis weight, 60% initial moisture content) [103]

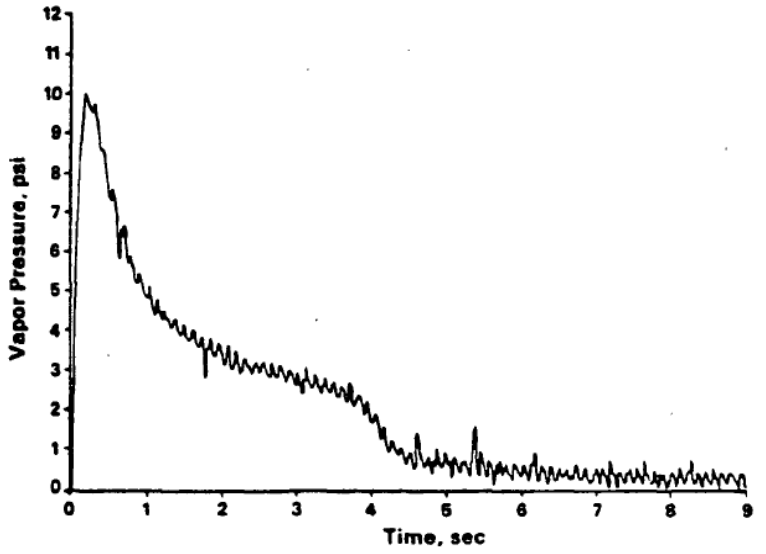

Figure 2.19 Vapor phase pressure at hot surface for an unbleached softwood Kraft handsheet, (42 lb/1000 ft^2 basis weight, 60% initial moisture content, 149^{o}C surface temperature and 320.6 KPa applied gage pressure) [105]

They noted that the magnitude of the vapor phase pressure peak increased with higher surface temperatures and applied pressures[104,105]. Pounder [98] was the first to come up with a complete model for high intensity drying by extending the model of Ahrens [106]. The model divides the sheet into different zones containing fractions of fiber, liquid, water and water vapor during the various stages of drying and further accounts for the different processes of liquid convection, vapor convection and higher applied pressures occurring in these zones [98]. Pounder's model gave good predictions of drying rates in impulse drying. Lindsay used a moving boundary approach to examine the role of vapor pressure generation and phase change heat transfer in both impulse drying and in other displacement dewatering processes [107]. To further understand the convective vapor flow process and its relation to the porosity of paperboard, a brief discussion on Darcy's law and the Kozeny-Carman equation is given below.

2.3.4.1 Darcy's law and the Kozeny-Carman equation.

Darcy's law is widely used and is an accepted theory to account for fluid flow inside a paper sheet [108-110]. Mokadam was one of the first to theoretically derive the general form of Darcy's law [111]. The superficial velocity in a steady state, isothermal, incompressible flow through a homogenous porous medium is given by -

$$u = \frac{Q}{A} = \frac{K_o \cdot \Delta P}{L} \tag{2.18}$$

where:

u = superficial linear velocity (m/s)

Q = volumetric rate of flow (m^3/s)

A = cross-sectional area of the test specimen (m^2)

ΔP = frictional pressure drop (KPa)

L = thickness (m)

K_o = a proportionality factor relating to fluid and porous medium properties.

The frictional pressure drop in the above equation ignores any inertial effects in the medium and is entirely due to the viscous drag of the fluid. Experimental investigations later revealed the flow to be independent of the fluid density. Thus the equation can be rewritten to give the well known form of Darcy's law-

$$u = \frac{Q}{A} = \frac{K \cdot \Delta P}{\mu \cdot L} \tag{2.19}$$

where

K is permeability coefficient dependent on the porous medium (independent on fluid properties. (m^2)

μ - Viscosity of the fluid (Kg/m-sec).

Hence, the permeability according to Darcy's law is defined as the volume of fluid with unit viscosity that can pass through a unit area when a pressure gradient is applied across the thickness of the medium. Permeability can be measured experimentally and depends on the porosity of the sheet. Porosity is defined as the void volume inside a paper sheet and can be calculated as –

$$\varepsilon = 1 - CV \tag{2.20}$$

where

C- apparent density of the paper sheet (kg/m^3)

V – fiber specific volume (m3/kg).

Several studies have focused on empirically relating the permeability of a sheet to its porosity. These include the hydraulic radius theory; analytical approaches with drag theories and statistical approaches have also been described [73]. For the case of paperboard, the "hydraulic radius theory" or the Kozeny-Carman approach is widely used. The Kozeny-Carman approach considers paper as a system of capillaries. The Poiseuille equation to viscous flow through a long straight cylindrical tube is given as

$$u = \frac{Q}{A} = \frac{R^2 \cdot \Delta P}{8 \cdot \mu \cdot L} \tag{2.21}$$

where

R – radius of capillary (m)

u – velocity (m/s)

Q – flow rate (m^3/s)

A- cross sectional area of flow (m^2)

L – length scale (m)

ΔP = frictional pressure drop (KPa)

For the case of paperboard, the channels are not necessarily of circular cross section; hence for channels with a non circular cross section a hydraulic radius can be defined as

$$m = \frac{\text{volume of Channel}}{\text{Wetted area of Channel}} = \frac{\pi \cdot R^2 \cdot L}{2\pi \cdot R \cdot L} = \frac{R}{2} \tag{2.22}$$

Thus equation 2.22 can be rewritten as –

$$u = \frac{Q}{A} = \frac{m^2 \cdot \Delta P}{K_o \cdot \mu \cdot L} \tag{2.23}$$

Kozeny [112] further related the permeability coefficient to the size, shape, and mode of packing of the solid material making up the porous medium. The total cross-sectional area of the pore space was shown to be equal to

$$A = \varepsilon A^{o} \tag{2.24}$$

where

A^{o} is the cross sectional area of the porous medium (m^2)

ε is the void volume of the medium.

By assuming the medium to be a group of parallel channels with similar cross sections oriented in the macroscopic flow direction, the mean hydraulic radius was calculated as

$$m = \frac{\varepsilon}{S_o} \tag{2.25}$$

where

S_o is the surface area per unit volume of the medium.

Carman [113] further studied this process and stated that since the flow through the medium is restricted and does not follow a straight line, the average velocity of the fluid is given as

$$u_e = \left(\frac{u}{\varepsilon}\right)\left(\frac{L_e}{L}\right) \tag{2.26}$$

where

u – superficial velocity (m/s)

L – actual thickness (m)

L_e – apparent thickness of channels in the direction of flow (m).

Combining equations 2.24, 2.26, 2.27 leads to the following

$$u = \frac{Q}{A} = \varepsilon^3 \cdot \frac{\Delta P}{K_o (L_e / L)^2 \cdot S_o{}^2 \cdot \mu \cdot L} \tag{2.27}$$

Thus the Kozeny factor 'k' is defined as

$$k = K_o \left(\frac{L_e}{L} \right)^2 \tag{2.28}$$

By assuming that the area of contact between particles is negligible, the surface area per unit volume (S_o) can be related to the surface area per unit volume of particles (S_v) as

$$S_o = S_v (1 - \varepsilon) \tag{2.29}$$

Substituting 2.29 and 2.30 in equation 2.28 gives the well known form of the Kozeny-Carman equation

$$u = \frac{Q}{A} = \varepsilon^3 \cdot \frac{\Delta P}{k \cdot S_v{}^2 (1 - \varepsilon)^2 \cdot \mu \cdot L} \tag{2.30}$$

Comparing with the Darcy's equation the permeability coefficient is defined as

$$K = \frac{\varepsilon^3}{k \cdot S_v{}^2 (1 - \varepsilon)^2} \tag{2.31}$$

The specific surface area can further be replaced by S_w on a mass basis by using

$$S_w = V \cdot S_v \tag{2.32}$$

where

S_w is the hydrodynamic surface area per unit mass of solid material

V is the hydrodynamic specific volume particles which compose the porous medium.

The Kozeny factor (k) for complex structures such as paperboard is experimentally determined. A value of k = 5.55 has been widely used for paperboard with porosities less than 0.8 [114, 115].

2.4 Infrared Thermography (IR)

Thermography is a non-contact non-destructive technique widely used in a variety of applications to measure temperatures and heat transfer profiles [116]. The current study employs the IR technique as a tool to understand the mechanism of foaming as detailed in Chapter 3. This section gives a brief overview on the various theoretical aspects of IR measurements.

All objects emit radiation above a temperature of absolute zero. Some of this radiation falls in the infrared spectrum which has a wavelength between 0.7 μm and 1000 μm [117]. The IR spectrum lies between the visible and microwave regions of the electromagnetic spectrum as shown in Figure 2.20 [117].

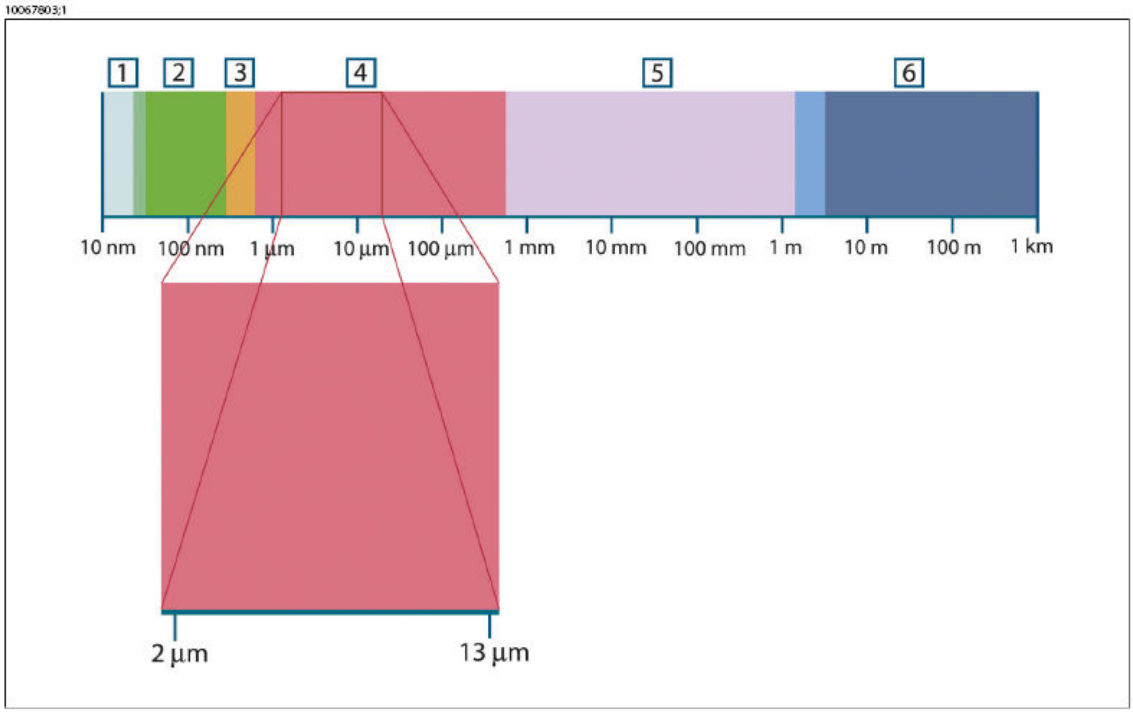

Figure 2.20 Electromagnetic spectrum [151] 1: X-ray; 2: UV; 3: visible; 4: IR; 5: microwaves; 6: radiowaves. [117]

Infrared thermography measures the amount of energy emitted by an object to determine its temperature. Since different objects emit different amounts of radiation, the physics of the process is better understood by defining the concept of a black body. A black body is an ideal object which is considered to absorb all the incident energy (radiation). The opposite end of a black body would be a perfect mirror which would reflect all the radiation [117]. The energy absorbed is emitted into the atmosphere as given by Kirchoff's law which states that at equilibrium the total energy emitted must be equal to the energy absorbed [117].

Most objects lie in between these extremes of a black body and a perfect mirror and are hence called gray bodies. A gray body would thus emit a fraction of the radiation which

is emitted by a black body. The radiation emitted depends on the temperature of the object and the material properties. Planck's law relates the amount of energy emitted to the temperature and wavelength as -

$$W_{\lambda o} = \frac{2\pi hc^2}{\lambda^5 \cdot \left(e^{hc/\lambda k T_a} - 1 \right)} \tag{2.33}$$

where

$W_{\lambda o}$ = emittance at wavelength λ (watts/m^2 * m)

c – speed of light $3E^8$ m/ws

h – Planck's constant – $6.6E^{-34}$ J/s

k – Boltzman constant $1.4E^{-23}$ J/K

T_a – absolute temperature (K)

λ – wavelength (m)

The energy emitted at different temperatures and wavelengths calculated using equation 2.34 is shown in Figures 2.21. The emittance increases with increasing temperatures and peaks at lower wavelengths. The Stephan-Boltzman equation relates the amount of energy emitted by a radiating blackbody at each wavelength to the absolute temperature [117].

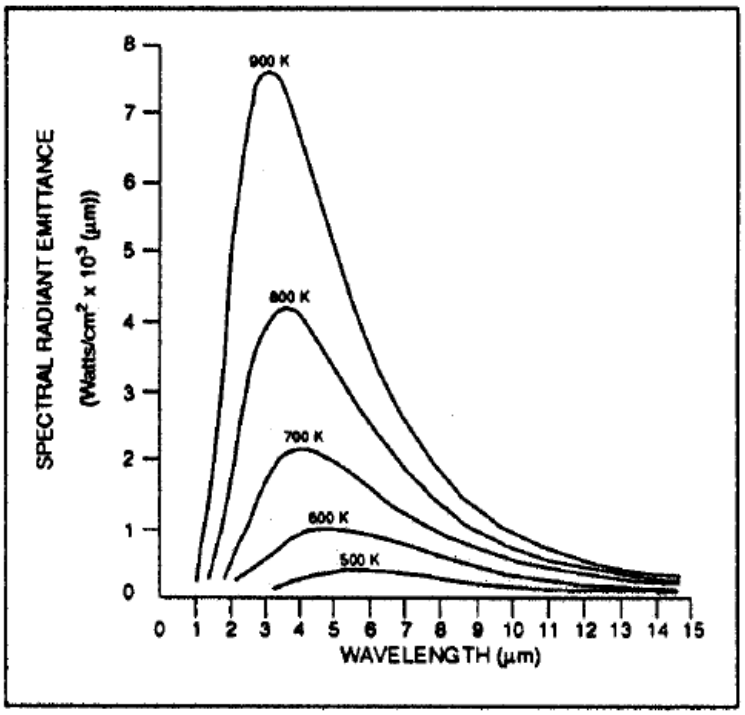

Figure 2.21 Planck's equation solved for different temperatures [117]

This is found by integrating Planck's equation at a particular wavelength of interest.

$$W_b = \sigma T_a^{\ 4} \tag{2.34}$$

where

W – total radiant emittance of a blackbody (W/m^2)

σ – Stefan Boltzman constant – 5.67 E^{-8} ($W*m^{-2}*K^{-4}$)

The IR camera measures the total amount of energy emitted by an object and further uses the Stephan-Boltzman relationship to determine its temperature. The expressions discussed so far assumed the object to be a black body that absorbs all the incident radiation. Most objects deviate from black body behavior by absorbing, reflecting or transmitting radiation. This deviation is wavelength-dependent implying that the same

object could be a black or gray body at different wavelengths. The deviation from black body behavior can be expressed as the emissivity of the object, which is defined as the ratio of emission of an object ($W_{\lambda o}$) to that of a blackbody ($W_{\lambda b}$) at a particular wavelength.

$$\varepsilon = \frac{W_{\lambda o}}{W_{\lambda b}} \tag{2.35}$$

Thus, the emissivity of a black body is one while a perfect mirror has an emissivity of zero. Emissivity is empirically determined and changes with temperature and the geometry of the objects. The Stephan-Boltzman law can be corrected to accounted for the gray body deviation by including the emissivity as

$$W_b = \varepsilon \sigma T_a^{\ 4} \tag{2.36}$$

The value of emissivity input to the camera is important to the accuracy of the temperatures measured. This is illustrated in Figure 2.22 where temperature measurements made during the drying of paper using different emissivity values lead to very different temperature readings [118,119]. To eliminate the effect of emissivity, Fike et. al. [118,119] used the Coefficient of Variance (COV) in their studies to measure the point of film breakage in drying. This is illustrated in Figure 2.23 which shows the COV values to be independent of the emissivity values input to the system. They also found COV to be a much more sensitive parameter than temperature itself for identifying subtle thermal effects, such as the point at which a surface just begins to dry [118]

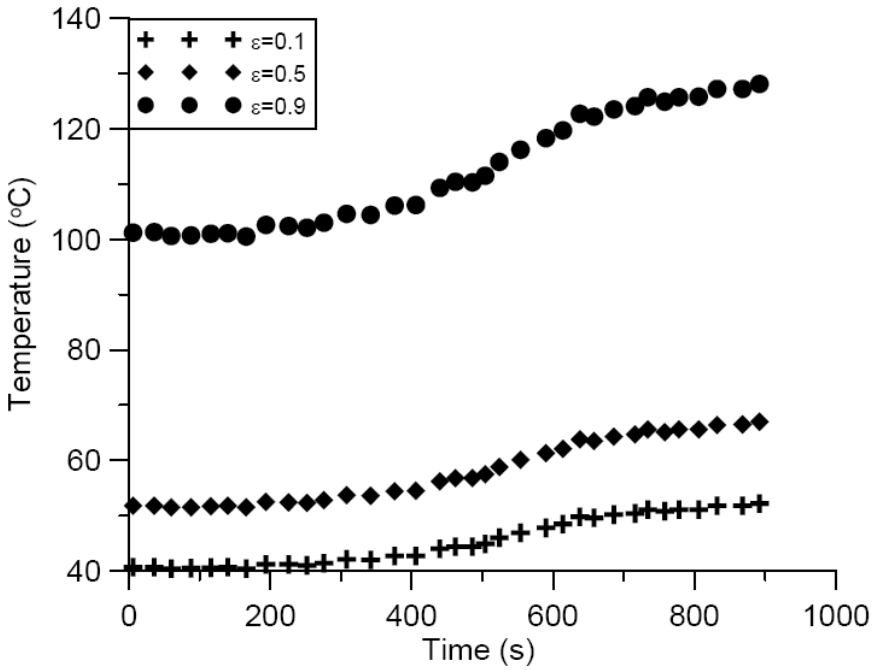

Figure 2.22 Temperature Vs. drying rate for paper at different emissivities [118]

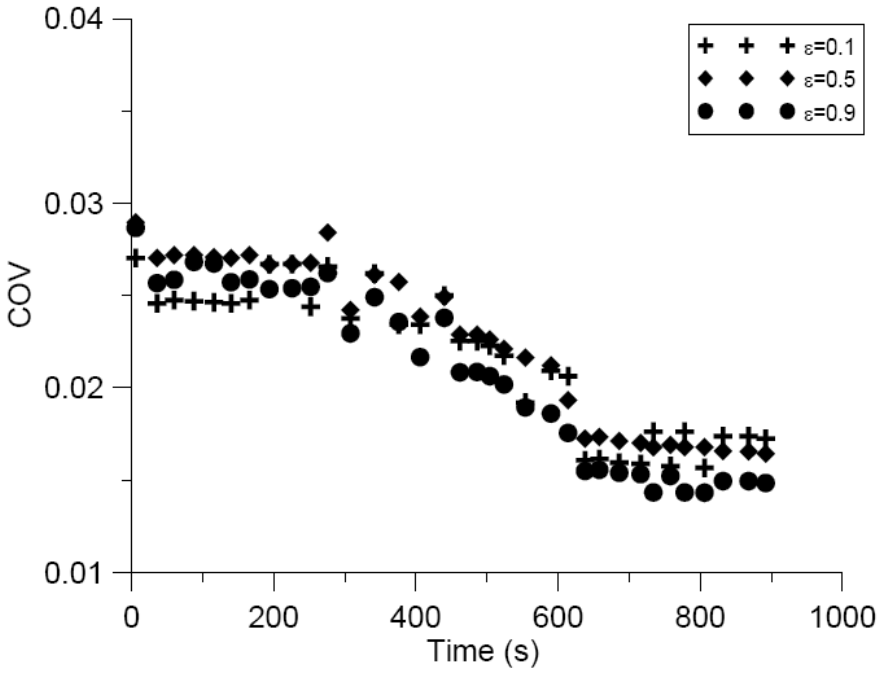

Figure 2.23 COV Vs. time for drying of paper at various emissivities [118]

CHAPTER 3: EXPERIMENTAL METHODS

Experimental investigations constituted an important part of the present investigation. The polymer-paper composite was manufactured both in a commercial facility and in laboratory and further foamed. The foaming mechanism was analyzed using a combination of high speed imaging and the infrared (IR) thermography technique. An image analyses technique was developed to determine the foaming mechanism. Lastly, SEM (scanning electron microscopy) images were analyzed to determine the bubble growth mechanism and the SEM surface uniformity of the uncoated paperboard. This chapter elaborates on the different experimental techniques used.

3.1. Polymer-paperboard composite

The board composite was produced by sandwiching a paperboard layer between two polymers of different densities. The lower density polymer with a lower melting point foams, while the density higher melt polymeric material serves as a barrier layer. Paper sheets were both made on a commercial paper machine (machine-made sheets) and also in a lab scale Formette Dynamique (handsheets).

3.1.1 Commercial sheets (Machine-made sheets)

Sheets were prepared at 250 g/m^2 basis weight using a 75% southern hardwood and 25% southern softwood bleached Kraft pulps. Pulp (11 kg) was refined for 10 minutes at 6 net

hp on a Jordan refiner to approximately 500 ml Canadian Standard Freeness (CSF). Commercial samples were prepared on a full-scale paper machine. These sheets were further pressed, dried, and calendered.

3.1.2 Laboratory sheets (Handsheets)

The laboratory pulp was refined at 2% consistency in a 5 lb Valley beater refiner to freeness levels of 300 ml CSF and 500 ml CSF. The handsheets were formed using a Formette Dynamique which constructs a sheet layer-by-layer [107]. The Formette Dynamique is discussed in more detail in the next section. In one instance, laboratory sheets were prepared from the same pulp used to make the machine-made paper. Handsheets were prepared from various combinations of softwood and hardwood pulps. The softwood and hardwood pulps were refined separately and later mixed in different ratios to form the sheets. A 2% starch by weight was added to the sheets to improve their strength properties. In two instances, kaolin clay from IMERYS (< 2 μm) was added at 5% (based on fiber weight) to pulp suspensions used to make laboratory formed sheets. A set of multi-ply sheets were also made by spraying the pulp in the order desired. The sheets were pressed at 7 KPa and dried on a rotary drum drier for 20 minutes. Sheet basis weight was measured using TAPPI Test method T-410 [120] from 3 different locations of sheet.

3.1.3 Formette Dynamique

The Formette is a centrifugal sheet former which has the capability of producing oriented and multi-ply handsheets to closely simulate commercial production [121]. It consists of a centrifugal bowl with an oscillating spray gun which is supplied with the pulp suspension. The pulp is sprayed onto the rotating drum; the mat is, therefore, built up incrementally [122, 123]. The drum includes a perforated inner wall and a solid outer wall in a concentric arrangement. Two fabrics, one coarse and another fine, cover the perforated wall over which the fiber is sprayed. A second drum serves as a mixing vessel where the pulp suspension is diluted to the required consistency. The arrangement of the two drums and the oscillating spray gun is shown in Figure 3.1. The forming process involves diluting the pulp suspension to less than 0.5% consistency in the mixing drum. The stirrer speed in the mixing drum is held constant in order to keep pulp suspension uniformly dispersed. The actual sheet forming starts by constructing a water wall by spraying about 5 liters of water at high speeds onto the fabrics of the rotating drum. The completion of the water wall is determined by change in color of the forming fabric. It should be noted that the pulp is thus sprayed onto the water wall instead of the fabric surface during the sheet forming process. The position and angle of the nozzle determines the direction of fibers sprayed onto the fabric surface. The nozzle emits a 25-degree, fan-shaped spray pattern at a rate of 60ml/sec when pressurized to 2 bars in a plane perpendicular to the direction of the drum. The direction of fibers and hence the MD:CD ratio is influenced by the speed of the centrifugal drum. Table 3.1 lists the different MD:CD ratios and the corresponding speeds needed.

Figure 3.1 Formette Dynamique. (a) Shows the centrifugal bowl on the left used to spray the pulp onto the mat and (b) the mixing vessel on the right shows the arrangement of spray gun in the centrifugal bowl.

Table 3.1 MD: CD ratios and corresponding drum speeds [124]

MD:CD ratio	Drum Speed
Low	730 m/min
Middle	825 m/min
High	1500 m/min

Once the bowl (drum) attains the required speed, the oscillating action of the spray gun leaves a uniform layer of pulp suspension onto the mat. In the current study the following conditions were used –

1. Pump pressure: 2 bars.

2. Centrifuge bowl speeds - 800 m/min
3. Spray nozzle - Vee Jet H 1/8VV 2504
4. Dryer temperature – 113^{o}C
5. Press pressure – 276 KPa

A radial weir present underneath the perforated inner wall of the centrifugal drum helps maintain the water level thickness. The water continuously flows through the forming fabric through the perforated walls and to the radial chamber at the bottom. The water overflows the radial weir to collect in the drainage section while the handsheet is being formed. Purge water is used at the end to flush any pulp from the tubing or drum to the spray gun. A scoop is present at the bottom of the centrifugal bowl and moves into the chamber between the perforated wall and the weir when engaged. Once the handsheet is formed, the scoop helps to deflect the water from the radial chamber into the drainage section thereby using the centrifugal force of the drum to dewater the sheet. The wet sheet along with the wire is removed from the drum after it comes to a complete halt. The wire and felt side are marked on the wet sheets and is further wet pressed between two blotter sheets. The process is repeated with fresh dry blotter sheets. The pressed sheets are further placed between two dry blotter sheets and dried in a drum dryer maintained at 113^{o}C.

3.1.4 Extrusion

Extrusion involves forcing a molten polymer onto the paper to allow adhesion of the polymer to the surface [54, 55]. All boards were extruded with low density polyethylene of different grades as shown in Table 3.2.

Table 3.2 Properties of polymers used.

	Melt Index (gm/10 min)	**density (gm/cc)**
Low density		
EC 479	5.7	0.921
EC 482	12	0.918
EC 476	13.7	0.9165
Barrier Layer		
Blend of 90% LDPE + 10% HDPE, Packaging tape		

Extrusion was done on one side of the sheet at speeds ranging between 61 and 213 m/min to give a polymer layer thickness between 17 and 45 μm. For the handsheets, LPDE was extruded onto the wire side. The opposite side of the sheet was sealed using a barrier layer as shown in Figure 1.1. In one case with handsheets, the LDPE was extruded onto the felt side. The barrier for the commercially obtained paperboards was a high-melting polyethylene blend consisting of 90% LDPE and 10% HDPE. Packaging tape was used for the handsheets and one set of machine-made sheets. A heavy roller was used to expel any air trapped between the board and the tape.

3.1.5 Board Moisture Conditioning

The board-polymer composite was conditioned in a moisture-controlled room under TAPPI standard conditions of 50% relative humidity and 23^{o}C until the moisture content reached between 6 and 8% [125]. This usually took about 48 hrs after which no significant change in moisture content was observed. To estimate the percentage of moisture in the board, the conditioned sheets were dried for 12 hrs in a convective oven and further weighed. The moisture content was determined from the difference between the weight of conditioned and the dried board.

3.2 Foaming experiments

The boards were foamed in a convective oven at 132^{o}C. The oven temperature was tracked using a thermocouple and further verified by an FLIR Thermovision A20 infrared camera. The sample was suspended in the oven as shown in Figure 3.2. The oven was allowed to attain the required temperature before the start of each experiment. The oven temperature profiles mimicked those used in a commercial set up. Samples were removed from the oven after foaming and allowed to cool for at least 3 minutes before any measurements were made.

3.3 Imaging Experiments

Imaging constituted an important part of the study and was aimed at understanding the bubble growth processes on the sheet. Foaming involves complex bubble processes. In this study an innovative technique to track and analyze these bubble growth processes across the board surface during the foaming was developed. The imaging experiments employed the convective oven along with the high speed camera. The oven door was replaced by a glass slab for these experiments. The sample was suspended at the center of the oven (away from the glass door) to avoid any effects due to heat loss through the door. A Phantom v4.2 high-speed camera from Vision Research was used in the process. The camera incorporates a SR-CMOS sensor for high speed use balancing sensitivity and resolution [126]. The camera allows for camera speeds up to 2100 pictures per second (pps) at maximum resolution of 512 pixels x 512 pixels. Higher speeds up to 90000 pictures per second could be obtained at lower image resolutions (32 pixels x 32 pixels). Exposure times could be varied between 2 and 10 microseconds independent of the camera speeds used. In the current study videos were recorded at 100 frames per second, and individual snapshots at different times were recorded as well. An exposure time of 10 microseconds was used. A Nikon Micro-Nikkon 105 mm f/2.8 lens was used in combination with a high magnification bellows to study the bubble processes. The imaging experimental set up is shown in Figure 3.2.

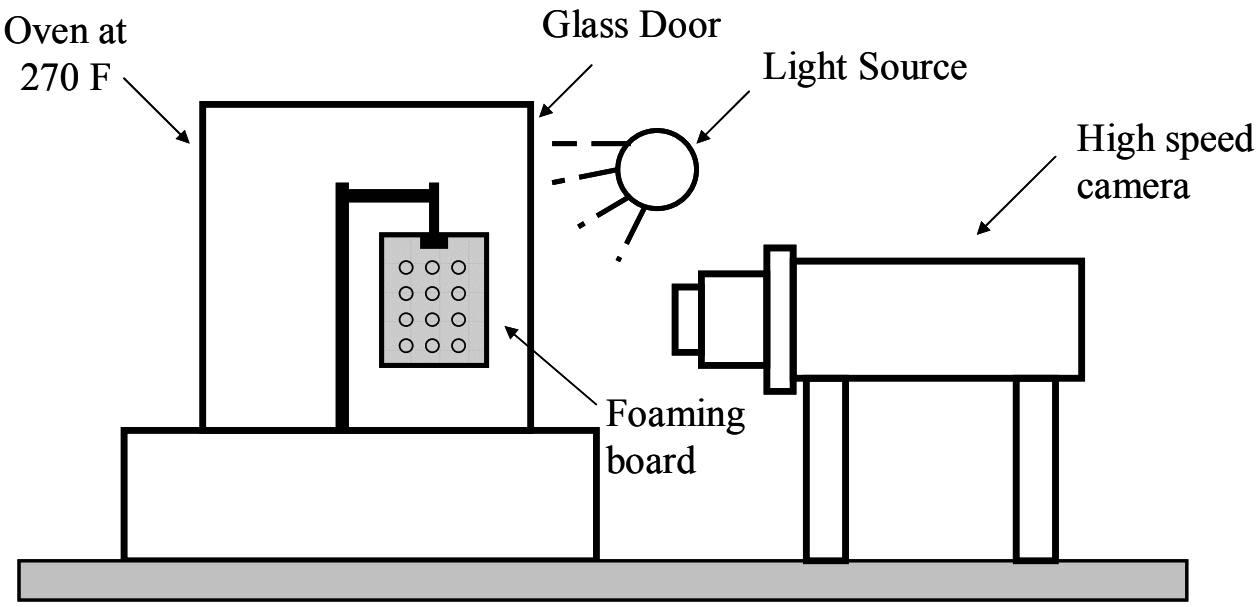

Figure 3.2 Foaming experimental set up

The Phantom research image analysis software [127] was used in conjunction with the camera to record the videos and grab individual frames. The light source was adjusted to be uniform across the area of interest. The Phantom software also allows changing brightness, contrast and exposure time settings during the experiments thus reducing any variation in light across the image sequence. A length scale was obtained by taking a screen shot of a ruler placed in the focal plane of the camera. The area of observation at a resolution of 512 x 512 pixels was determined to be 5 x 5 mm. The onset of foaming was indicated by the light reflected from the bubble surface as shown in Figure 3.3a. The number of reflected light spots varied with the number and size of the bubbles formed. Frames were grabbed from the beginning of the process until 90 seconds after the first bubble appeared in the video. On average, the first bubble appeared in the video at 30 seconds from the time at which the sample was placed inside the oven. Hence the total residence time of all samples inside the oven was 120 seconds. The images were

processed with Image J software [128]. The correspondence between the light reflected and the number of bubbles was manually verified.

Each image was converted to a gray scale 8 bit image. The brightness and contrast of the image was adjusted and further thresholded as shown in Figure 3.3 b, c. The complete image analysis sequence is illustrated in Figure 3.3. The number of bubbles, area of each bubble and their x, y positions were determined using the *analyze particle function* in the Image J software. The edges were ignored in the measurements due to high noise. Table 3.3 lists the different parameters used in the image analysis. The Image J results were processed using a MATLAB program. Bubble growth causes a change in the focal point and is a potential source of error because of the very small depth of the field at the high magnifications. This needed constant manual adjusting of the lens/bellows combination. All measurements were made at least in duplicate. The image analysis steps were further repeated once for each set of measurements. Error bars were calculated from the deviation from average values between the repetitions of experiments. In order to relate the size of the reflected light spots to the circumference of the bubbles, the area of a square that enclosed a bubble was measured manually for 50 bubbles of different sizes. The area of the square was ten times that of the spot created by the reflected light. The factor of ten was then applied to the spot area to obtain the area of the bubble. All measurements were at least made in duplicate. The volume of the bubble was further calculated by assuming all bubbles to be spherical.

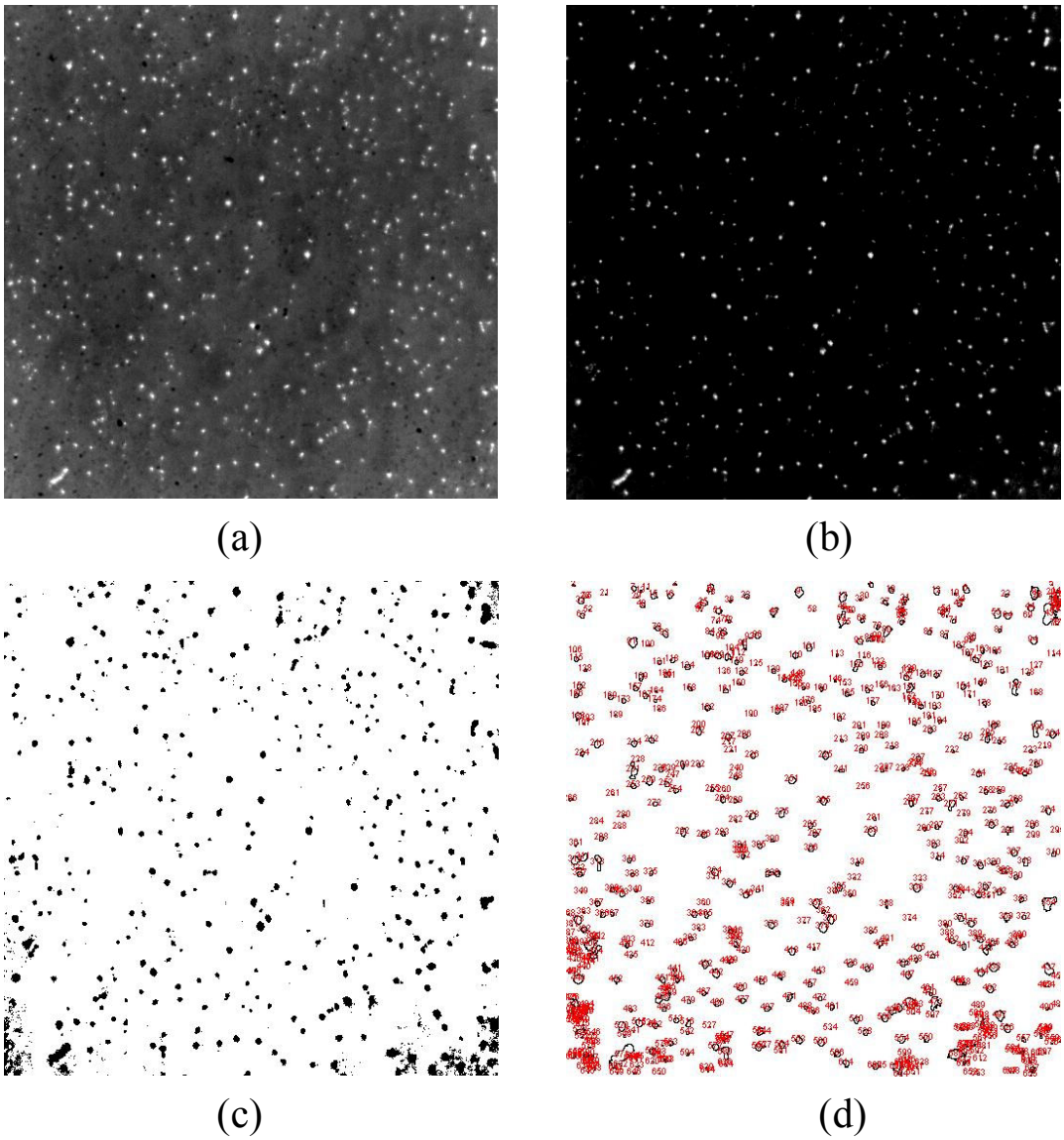

Figure 3.3 Image Analysis Procedure (a) Original image from the camera (b) Image with contrast/brightness adjusted (c) Threshold image (d) Final image showing the counted bubbles

Table 3.3 Parameters used in image analysis

Parameter	Value
Threshold	0 - 255
Size (pixel^2)	0 - infinity
Circularity	0.00 - 1.00

3.4 Vapor Loss Measurements

Vapor loss measurements were made by foaming board samples of 90 mm X 70 mm size in the convective oven at 132^{o}C to different times between 0 and 1000 seconds. The loss of moisture was determined from the difference in the weights of board before and after the foaming process. Samples were allowed to cool for 3 minutes before the weight measurements were made to remove any effects of re-condensation. The moisture lost through the surface ($M_{surface}$) was determined after sealing the edges of the board with epoxy. The moisture lost through the edges (M_{edges}) was then calculated by difference. The moisture accumulated inside the foam (M_{foam}) was estimated from the foam volume assuming that bubbles were comprised entirely of water vapor.

3.5 Infrared Thermography

Infrared thermography was used to determine the coefficient of variance (COV) of the board surface temperature during foaming. Thermography also helped determine the

temperature profiles during the foaming process. A FLIR A20 camera with an un-cooled microbolometer FPA detector was coupled to a lens with a 25° x 19° field of view and a minimum focal distance of 0.3 m [117]. This arrangement provides a thermal sensitivity of 0.12°C at 30°C. The system can analyze images at single pixel resolution and compensates for errors due to reflected radiation. The camera/oven arrangement was similar to that shown in Figure 3.2, with the high speed camera being replaced by an IR camera. Thermacam research software was used in conjunction with the camera to make the measurements.

The camera compensates for any reflections in the atmosphere between the camera and the object. The reflected ambient temperature was measured by placing an aluminum foil between the camera and the oven; an emissivity value of one was assigned to the foil, and the foil temperature measured. The camera also compensates for the relative humidity of the air between the oven and the camera. A 50% relative humidity was used; this is considered standard for short distances [117]. The atmospheric temperature between the camera and the oven was found to be 132^{o}C with a thermocouple.

The emissivity of the polymeric material was determined to be 0.97 by measuring the temperature of a black electric tape of known emissivity (0.96). The emissivity assigned to the board surface was adjusted so that the temperature of the board surface corresponded to the tape temperature. The IR camera was also used to confirm that the temperature of the polymer exceeded its melting point during foaming.

The following parameters were used in the camera while making the measurements -

1. Object Emissivity (ε) – 0.97
2. Relative humidity of atmosphere-50%
3. Atmospheric temperature – 132^{o}C.
4. Distance between camera lens and object – 0.3 meters
5. Reflected ambient temperature – 27^{o}C

The glass door of the oven was replaced with an aluminum foil and thermograms were taken through a small square window in the foil. The oven was allowed to attain the required temperature before each experiment. Thermograms of the board surface were taken during the foaming process inside the oven; the camera was located outside the oven at a distance of 0.3 m from the object. Measurements were recorded from the time the sample was placed inside the oven for a period of 120 seconds. A unit area was marked using the Thermacam researcher software and its average temperature and standard deviations were calculated. The camera along with the Thermacam software measures the temperatures of each pixel and calculates the average temperature for the marked unit area. The average temperature and standard deviation were recorded at different times of foaming. Data from the Thermacam researcher software was extracted into Microsoft excel sheet using a Visual Basic program. The COV is calculated by dividing the standard deviation of all of the temperatures in the area of interest by the average temperature. Standard deviations (COV) for all measurements were found to be less 2%.

3.6 SEM studies

A scanning electron microscopy was used to study the cross section of the board during the foaming process. This was also used to analyze the surface uniformity of the foaming. Scanning electron microscope (SEM) images were collected with a LEO 1550 instrument. The cross-section of pre-foamed boards at different times between 0 and 120 seconds was studied to determine the bubble formation and growth mechanism. Images were also collected from the surface of the board before the extrusion process. These were analyzed using a new surface uniformity technique as described in Chapter 4.

Some of the conclusions presented in this thesis are based from the difference in trends observed between all machine-made sheets and laboratory handsheets. Table 3.4 illustrates the number of experiments conducted in order to confirm this difference.

Table 3.4 Number of measurements used to determine the differences in trends between machine-made sheets and handsheets.

Experiment	Sample	No. of samples	No. of repetitions	Total No. of measurements
Imaging experiments	Handsheets	17	4	68
	Machine paper	28	4	112
Infrared Camera Experiments	Handsheets	17	2	34
	Machine paper	28	2	56
SEM Uniformity technique	Handsheets	18	20	360
	Machine paper	1	60	60

3.7 Other Methods

3.7.1 Valley Beater Refining [129]

Pulp was obtained in the form of dried sheets and was disintegrated in a 5 lb Valley beater for 15 minutes. The TAPPI T-200 was used to further refine the pulp at a consistency of 2%. A 12.7 kg of weight was used on the base plates for refining. Refining was carried out in 20 minute cycles until the required freeness was attained.

3.7.2 Freeness

TAPPI Test method T 227 om-99 was used to determine the Canadian standard freeness (CSF) [130]. A schematic of the freeness tester is shown in Figure 3.4

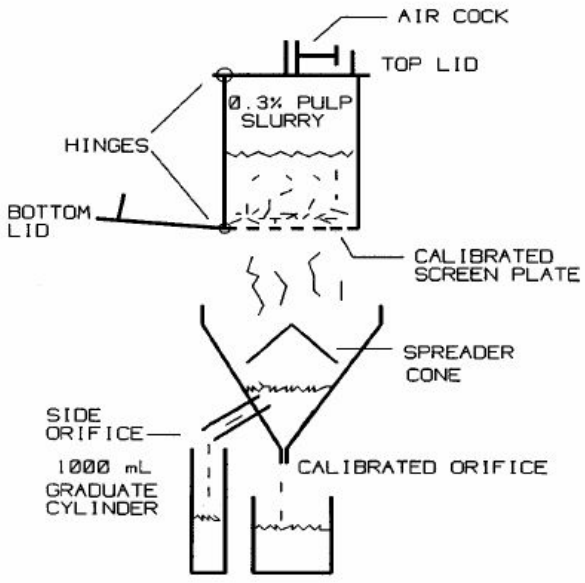

Figure 3.4 Freeness Tester [76]

The freeness values were further corrected for temperature and consistency using Equation 3.1 and Equation 3.2 [130].

$$CSF_T = CSF_U + 4.6(20 - T)\left[1 - \frac{(400 - CSF_U)^2}{61000(CSF_U)^{0.25}}\right] \quad (3.1)$$

$$CSF = CSF_T + 590(C - 0.3)\left[1 + \left(\frac{0.4 - C}{0.2}\right)\left(\frac{CSF_T}{1000}\right)\right]\left[\frac{1 - (CSF_T - 390)^2}{87000(CSF_T)^{0.2}}\right] \quad (3.2)$$

where - T is temperature in Celsius

C is consistency of the sample.

3.7.3 Permeability measurements (Gurley test) [131]

TAPPI Test Method T 460 om-06 air resistance of Paper (Gurley Method) [130] was used to determine the permeability of paperboard. The Gurley method measures the air resistance of the sheet by determining the time needed for a unit volume of air to pass through the thickness of the sheet under a unit pressure differential. A circular area of 6.45 sq. cm is used in the measurements. Permeability of a paperboard can be calculated using Darcy's law [115] as

$$K = \frac{V \cdot \mu \cdot L}{A \cdot \Delta P \cdot t} \quad (3.3)$$

where K – permeability (m^2)

V –Volume of air ($1*10^{-4}$ m^3)

μ – Viscosity of air ($1.8*10^{-5}$ kg/m-sec)

L – Thickness of the board (m) – obtained from sheet caliper data

A – Area of the board ($6.45 *10^{-4}$ m^2)

ΔP – pressure drop across the sheet – (1.22 KPa)

t – Time (sec) measured using the Gurley Test apparatus.

Ten measurements were made from different areas of the sheet for each sample. Errors reported represent percent standard deviation.

3.7.4 Caliper (Hard platen and soft platen test)

The final foam thickness was measured by the TAPPI 551 soft platen method [132], which compensates for surface roughness effects and also partially compensates for compressibility due to more uniform distribution of pressure across the platen [132]. This method gives the effective thickness which is the theoretical thickness calculated from the relation between extensional stiffness to bending stiffness [132]. Results reported in this thesis are from the soft platen measurements made on a 200 (±5) mm^2 area of the sheet. Ten readings were taken from different areas of the foamed board and the mean was calculated. Error bars shown represent the percent standard deviation. Foam thickness measurements were also made by the TAPPI 411 hard platen method [133]. This method gives the perpendicular distance between the two surfaces. Measurements made with either soft or hard platens gave similar trends within 5%. The soft platen method was also used to measure the board caliper before and after the polymeric film was extruded.

CHAPTER 4: MECHANISM OF FOAMING

4.1 Introduction

In this chapter, the mechanism of foaming is addressed and the characteristics of a board that lead to a product with evenly distributed bubbles of a uniform size are determined. Paperboard plays an important role in the final foam quality; various parameters of the paper sheet are varied to determine its influence on foaming. The type and composition of the sheets employed in the study are listed in Table 4.1. The bubble formation step is first analyzed by employing a scanning electron microscopy technique where the board cross section is examined. The growth process during the foaming is further investigated by tracking individual bubbles using an imaging technique as described in Chapter 3. An infrared thermography technique is used to study the heat transfer profiles on the sheet surface, which is used to further understand the foaming mechanism. A new SEM uniformity technique was developed and employed to study the paperboard surface properties. Results presented in this chapter have been accepted for publication in the *AIChE Journal.*

4.2 Results and Discussion

4.2.1 Bubble formation – cross-section analysis

Typical SEM images of the cross-section of board taking during foaming are illustrated in Figure 4.1. A bubble begins to grow at the paper/polymer interface (Figure 4.1 a) and then expands into the polymer layer (Figure 4.1 b).

Table 4.1 Composition of paper boards studied

Sample ID	Hardwood (%)	Softwood (%)	CSF (ml)	Filler (%)	Refining
M[1]	75	25	500	-	Jordan refiner
H1	100	0	300	-	Valley beater
H2	75	25	300	-	
H3	50	50	300	-	
H4	0	100	300	-	
H5	75	25	500	-	Jordan refiner
H6[2]	80	10, 10	300	-	Valley beater
H7[2]	10, 10	80	300	-	
H8[3]	100	0	300	-	
H9[3]	0	100	300	-	
H10	0	100	300	5	
H11	75	25	500	5	Jordan refiner

M – machine-made paper made on a commercial machine, H- Laboratory handsheets made on a formette; 1 - sheets calendered, 2-stratified (multi-ply sheets), 3 - sheets extruded on felt side (all other handsheets were extruded on wire side). All samples were extruded with EC 482 polymer at 61m/min to 42.2µm thickness.

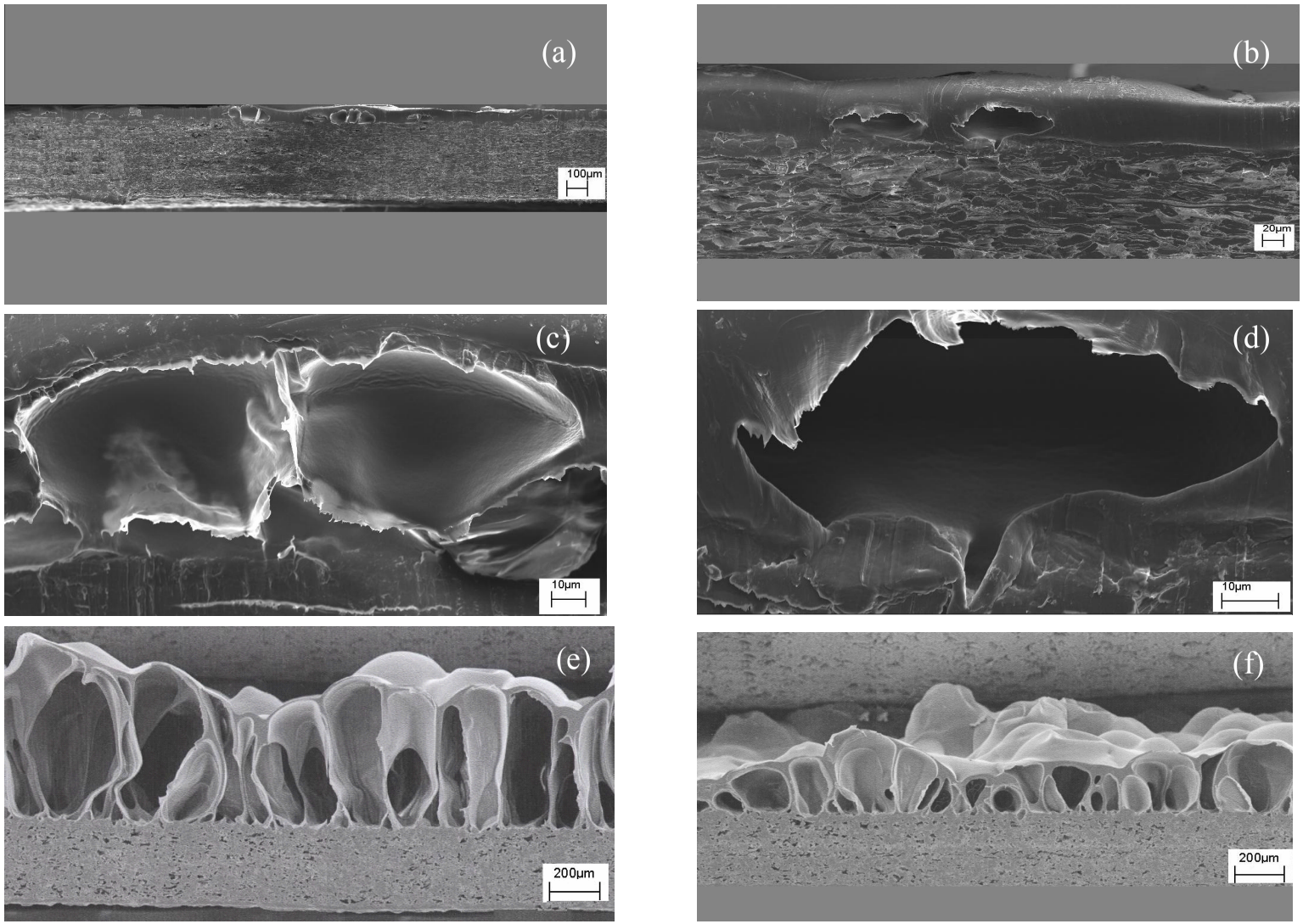

Figure 4.1 Bubble growth profiles and SEM analysis of cross sections. (a), (b) (c), (d) were foamed for 10 secs; (e), (f) were foam for 120 secs; (e) and (f) represent uniform and non-uniform bubble size distributions, respectively.

It is clear that a bubble originates at a pore, which implies that water vapor travels through the sheet structure, emerges at a pore opening and then foams the polymer. The images in Figure 4.1 also suggest that the pore shape is conical. It follows, therefore, that the surface properties of the sheet, especially the pore distribution, will be a major component of the bubble profile of the finished product. Paper board is a non homogenous complex structure with a wide distribution of pore size depending on the composition of the sheet. The pore shape and size could influence the shape of bubbles formed as seen in Figure 4.1 (c) and 4.1 (d). The final foam bubble size distribution at 120 seconds as seen in Figures 4.1 (e) and 4.1 (f) illustrates a uniformly foamed board and a poorly foamed board, respectively.

4.2.2 Bubble growth profiles

Wood fibers are hygroscopic which allow paper to absorb water. The moisture content in the sheet can be calculated as the ratio of absorbed water to the mass of oven dry paper. The water (moisture) in the fiber is present between 6 and 8% by weight, which means that all the moisture would be present as bound water [91]. Walsh and Banerjee [95, 96] estimated the amount of bound water present as a monolayer in wet pulps to be 10%. The present study employs a conditioned dry paperboard and hence the moisture would be present as a monolayer adsorbed onto the fiber surface. At these low concentrations, nucleation of water vapor to form a vapor bubble is improbable. Transport of water into the polymer layer through simple convective flow of vapor through the pore is much more likely.

The imaging experiments were used to determine the bubble growth profiles for different cases. An example of a bubble growth profile is presented in Figure 4.2. These bubble profiles were observed in all samples investigated as listed in Table 3.4. The bubble growth rate and the maximum number of bubbles are higher for the machine-made paper as compared to the handsheets.

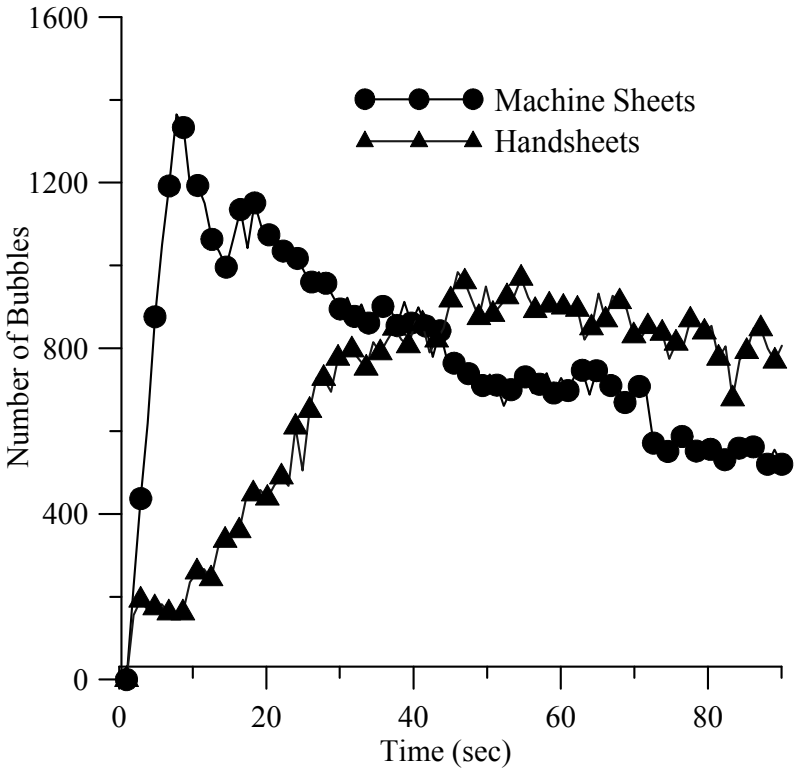

Figure 4.2 Growth profiles for laboratory handsheets and machine-made paper.

The paperboard has many more pores than the number of bubbles created. A more elaborate discussion on pore size distribution is given in Chapter 6. The maximum number of bubbles seen in the bubble growth profile should directly correspond to the number of active pore openings that lead to bubble formation. The growth rate should

depend both on the rate of vaporization and on the resistance offered by the porous sheet to its transport. The growth and decay of the bubbles is due to bubble coalescence and bubble collapse, respectively.

4.2.3 Variation in Paper properties

The difference in the growth profiles observed indicates that the properties of the paper sheet would influence foaming. A series of experiments were conducted with the different sets of handsheets and machine-made listed in Table 4.1. Figure 4.3 summarizes the maximum number of bubbles formed, the final bubble count at 90 seconds, and the degree of coalescence for several handsheets and a machine-made paper.

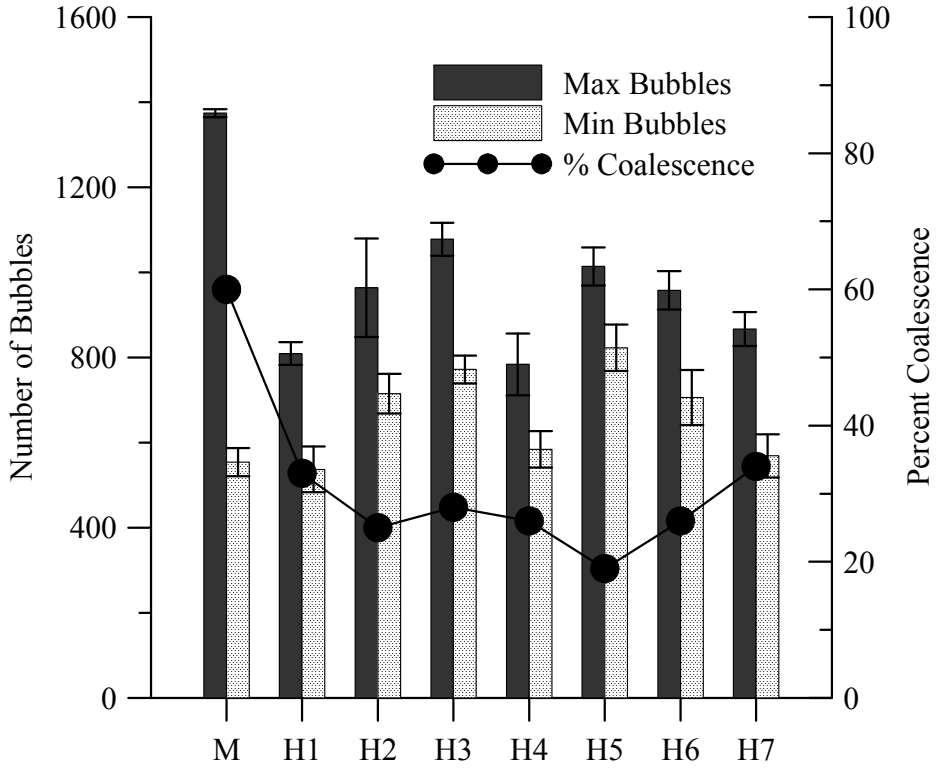

Figure 4.3 Variation of paper board properties in foaming.

The bubble count shown here is for a foaming time of 90 seconds from the time the first bubble appeared in the imaging studies. On average, the first bubble in the imaging experiments was observed at 30 seconds after the board was placed in the oven; thus the total foaming time was 120 sec. The degree of coalescence was calculated from the maximum and final bubble count. There is a clear difference in the maximum number of bubbles and the degree of coalescence between the machine-made sheets and any of the handsheets. The higher degree of coalescence for the machine-made sheet is consistent with the larger number of bubbles initially formed. The higher bubble density would reduce the distance between bubbles and promote coalescence.

The two primary types of wood fibers widely used in papermaking are softwood and hardwood. Softwood (SWD) fibers are longer with fiber lengths of 2.5 – 7 mm while hardwood fibers have a length of about 1-1.5 mm [76]. Changing the percentage of softwood and hardwood in the sheet would also change the number of fiber crossings, and thus the number of pore openings and the internal structure of the porous web. The behavior of the various handsheets was remarkably similar, despite the differences in fiber composition, the presence of additives, and the nature in which the sheet was prepared. These properties would also change the nature and number of potential nucleation sites.

Sheets H6 and H7 in Figure 4.3 were prepared in a Formette Dynamique sheet former where a multi-ply sheet is built up layer by layer and is, therefore, more stratified than the

other laboratory-made sheets. A multi-ply sheet will have a different internal structure as compared to a single ply sheet. Again, no differences in bubble profile were observed. H2 and H5 represent samples prepared from pulps refined to different freeness values. Refining exposes more fiber surface and causes breakage of covalent and hydrogen bonds and further causes structural damage and fiber modification [82, 85]. Refining should affect the bonding between fibers; the lower freeness represents a higher degree of refining, and thus leads to better bonding. The freeness values did not affect the number of bubbles or the coalescence rates. Nucleation agents are frequently used in traditional polymer foaming [134, 135]. Figure 4.4 compares bubble profiles of handsheets (H10 and H11) containing 5% clay with their clay-free counterparts. The clay had no effect on bubble distribution, confirming that nucleation is unimportant.

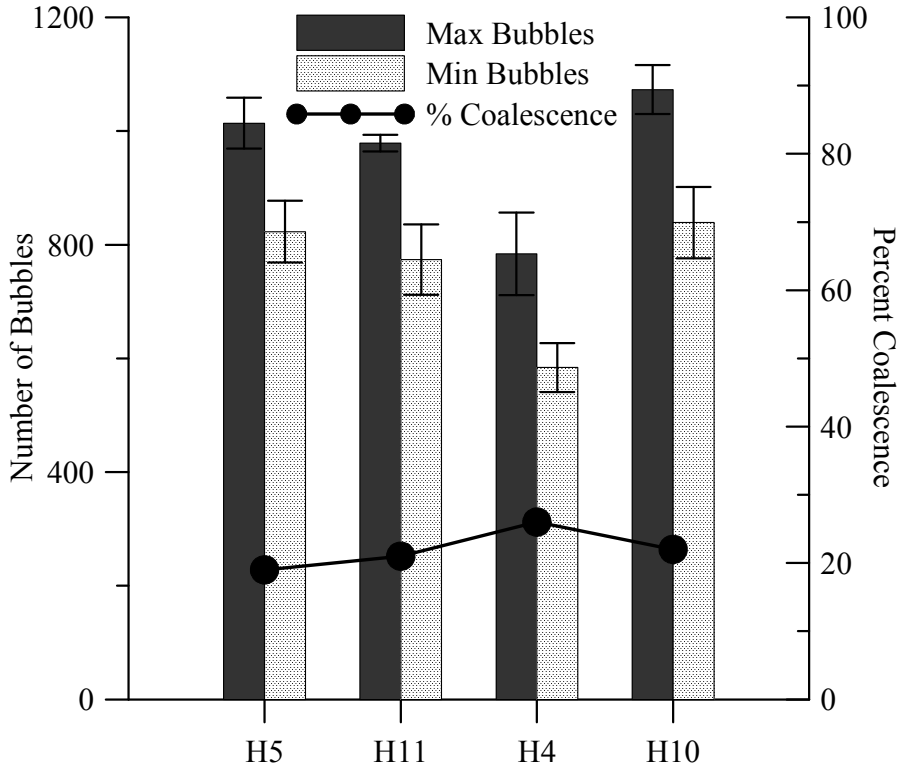

Figure 4.4 Effect of filler on foaming.

The wire and felt sides of handsheets are known to have different surface properties [136]. The foaming behavior of sheets extruded on the felt (top) side and wire (bottom) side was also very similar as shown in Figure 4.5. Clearly, bubble formation is insensitive to the composition of the sheet and to some of the operational variables used to make it. The only difference observed was between sheets made on a machine and on the Formette.

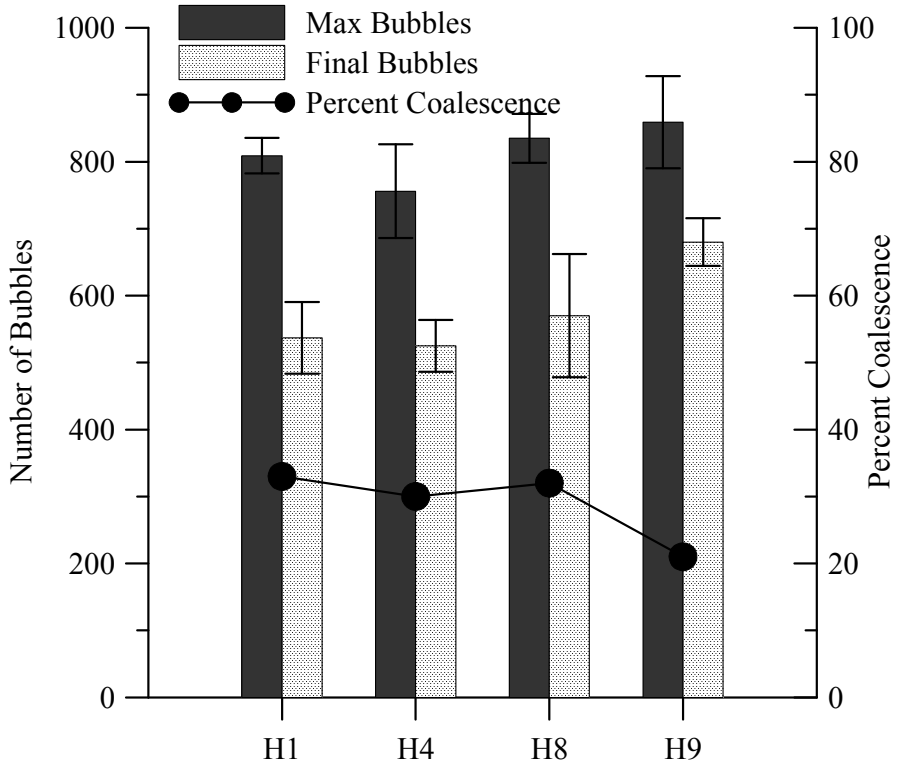

Figure 4.5 Comparison of growth profiles for foaming on wire and felt side. H8, H9 extruded on felt side, H1, H4 extruded on wire side.

The barrier layer helps direct the vapor generated in the thickness direction of the paper sheet towards the molten polymeric layer that is foamed. A poorly glued barrier layer

could lead to the moisture escaping to the opposite surface or from the sides, leading to poor foaming. No difference in the bubble growth profile was observed when the extruded polymeric layer was replaced with a packaging tape as illustrated in Figure 4.6.

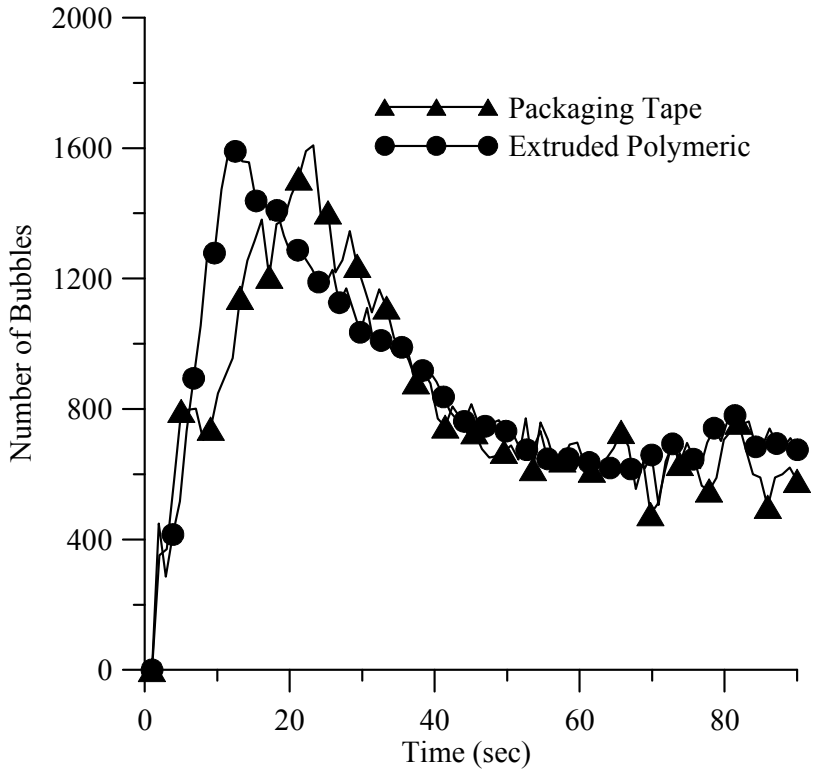

Figure 4.6 Effect of the barrier layer on foaming.

As the sheet warms up the moisture in the board evaporates and the water vapor enters the void space. As long as the volume density of the sheet remains constant the pressure developed within the sheet should be independent of the composition of the sheet. Foaming begins when the pressure builds up to the point where it overcomes the resistance of the molten polymer. The number of bubbles formed should depend on the geometry of the surface of the sheet; well-distributed pores should lead to uniform bubbles. Thus, sheet uniformity should be the critical parameter governing bubble

quality. The rate at which the vapor travels through the porous web should control the pressure build up, which governs the growth rate of the bubbles. This would depend on the resistance offered by the sheet to vapor transport. These two properties are further investigated by studying the surface uniformity and the permeability of the sheet.

4.2.4 Analysis of paperboard properties

The two properties which play an important role in the foaming are the surface properties of paperboard and its internal structure, which controls the permeability or resistance to transport. The surface properties not only affect the pore and fiber distribution but also the interfacial properties between paper and polymer. Factors such as the degree of refining of the fibers, the presence of fillers, and the type of coating applied to the sheet, the amount of wet pressure applied to the sheet, drying conditions, etc. affect the permeability of the sheet [73].

In order to understand the differences in the surface profiles between the machine-made paper and the various handsheets, a new technique for studying the *x*-*y* uniformity of paperboard was used. An SEM image of the surface of the paperboard was taken before extrusion of the polymer. The image was converted to a 0-255 grayscale, ranging from the darkest to the brightest pixel, as illustrated in Figure 4.7. The dark regions represent the pores, while the gray regions represent the fiber surfaces. The white regions on the other hand represent the fiber edges.

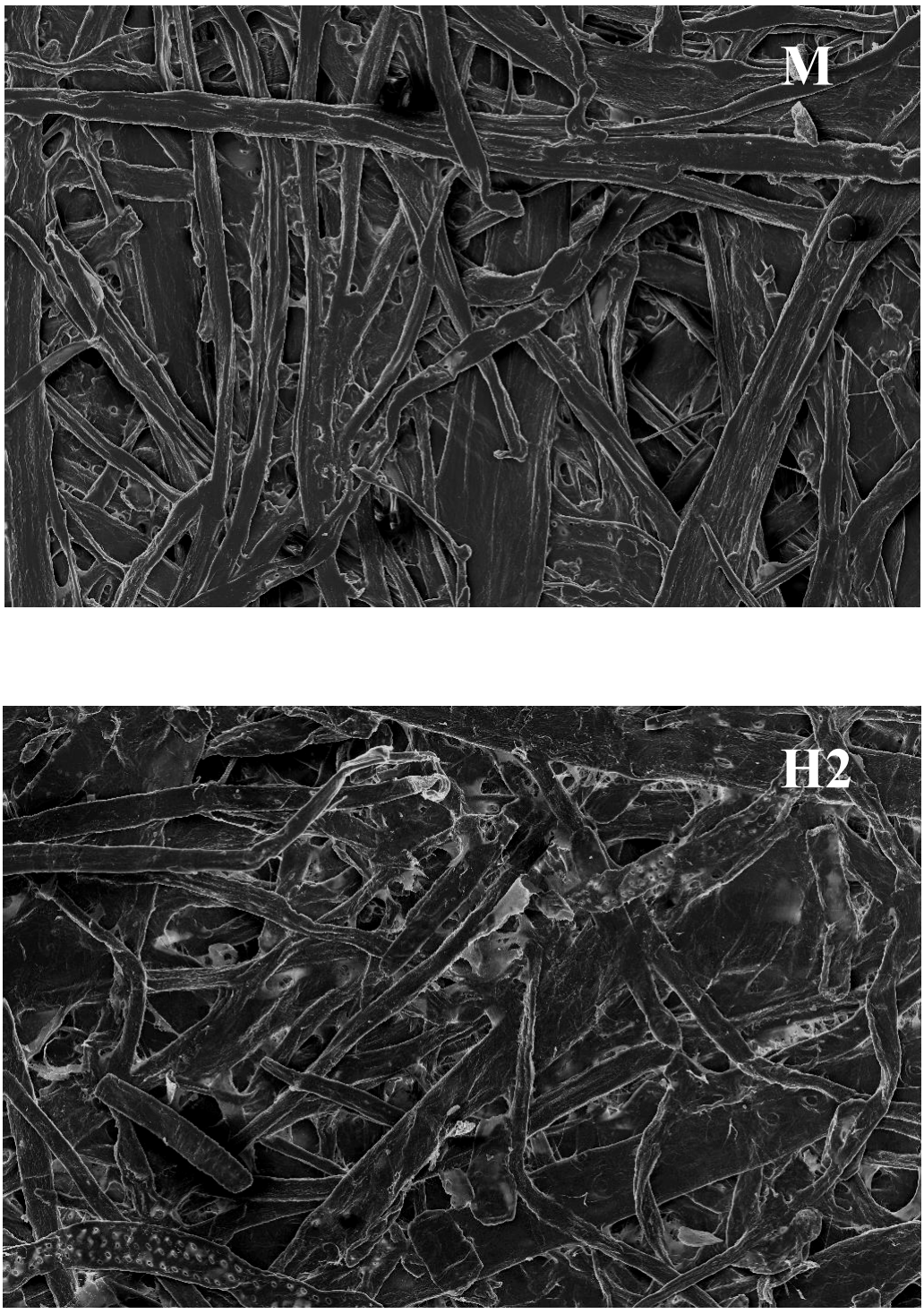

Figure 4.7 SEM images of samples M and H2.

A Uniformity Index was defined (eq 4.1) as the absolute difference between a given pixel and the mean pixel value of an image.

$$\text{Uniformity Index} = \left| (P - P^{*}) \right| \qquad (4.1)$$

Here, P is the number of pixels times a given pixel value.

P^{*} is the weighted mean, *i.e.* ΣP/ (total number of pixels in the image).

A higher Uniformity Index indicates a greater deviation from the mean pixel value and represents a less uniform board surface. Figure 4.8 shows the Uniformity Index plotted with respect to the different pixel values for both laboratory and machine-made samples.

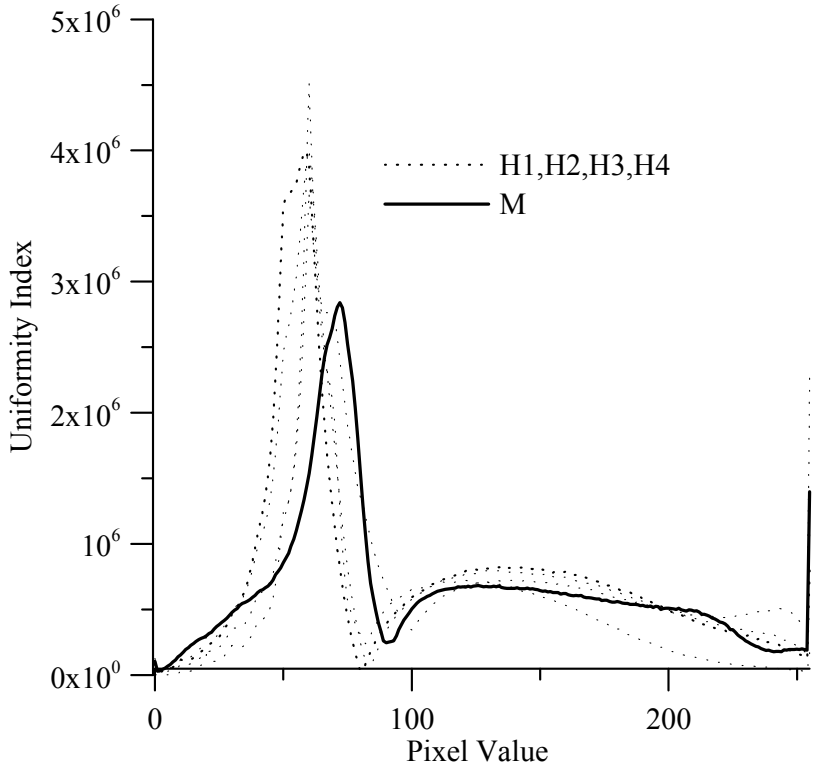

Figure 4.8 Variation in Surface Uniformity Index

The machine-made sheets (M) show a lower Uniformity Index than any of the handsheets (H). This indicates that the machine-made sheets have better surface uniformity, *i.e.* a more uniform layout of the fibers and a more even pore distribution as compared to the handsheets. This is also obvious from the SEM images illustrated in Figure 4.7. The lower Uniformity Index of machine-made paper increases the probability of a pore contributing to a bubble. All the sheets in the present study had similar volume densities as shown in Figure 4.9. With the board density remaining constant, a more permeable sheet would lead to faster foaming. Results from air permeability measurements made with the Gurley Test [131] are shown in Figure 4.10. The results of Gurley test measurements are expressed as Gurley seconds and further converted to permeability (m^2) as discussed in Chapter 3.

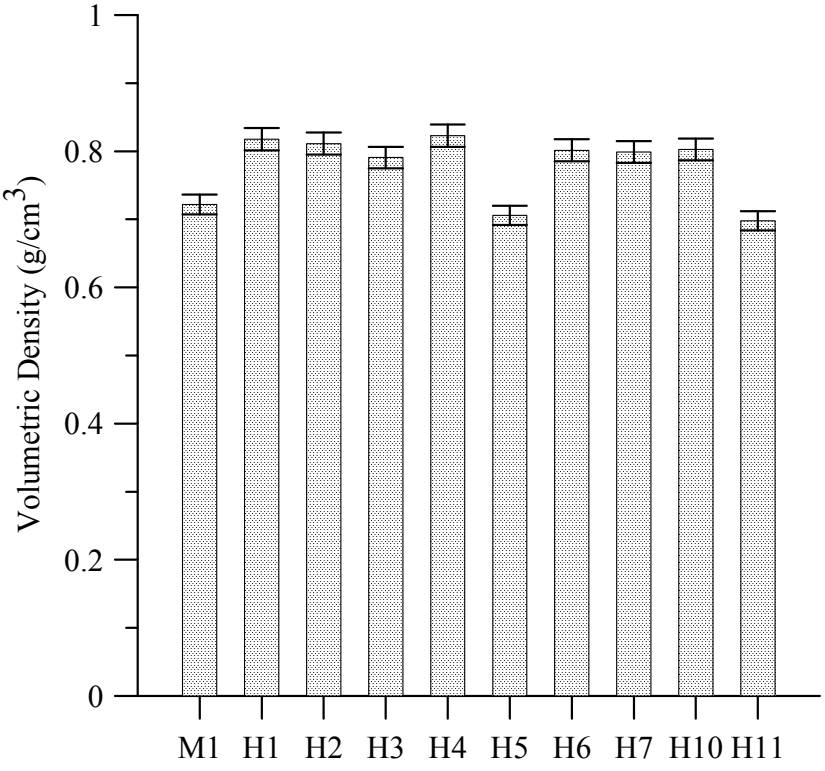

Figure 4.9 Volumetric density of paper sheets used in the study

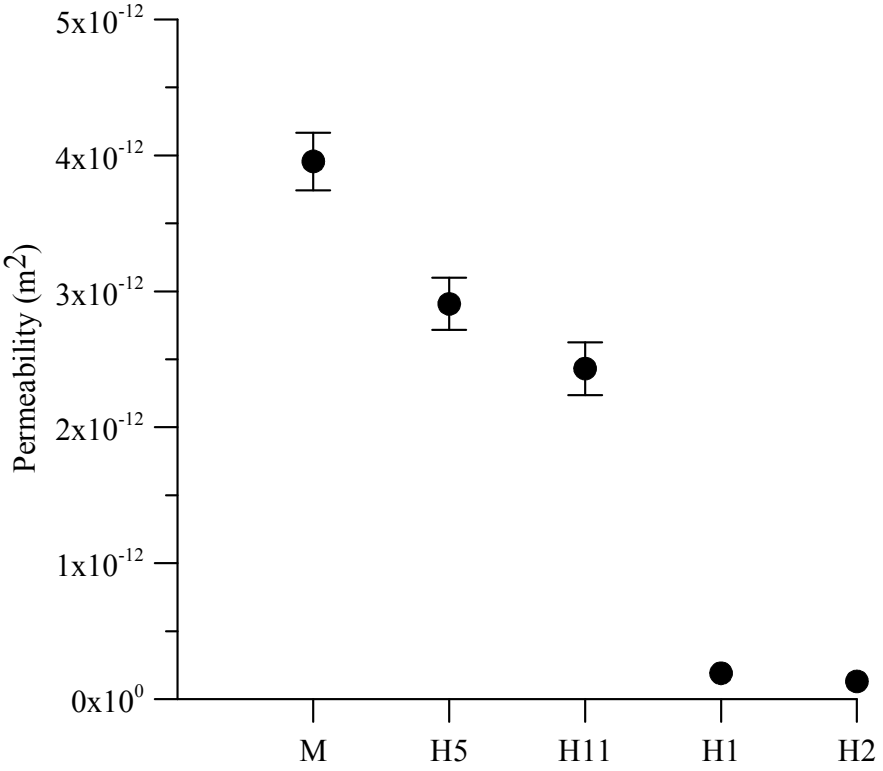

Figure 4.10 Permeability of the sheets.

The laboratory sheets have lower permeability as compared to machine-made sheets. This explains why delayed growth is seen in the bubble profiles. The laboratory handsheets were prepared in the Formette unit where the sheet is constructed layer-by-layer [122, 123]. In contrast, in machine-made paper, a continuous jet of fiber and water is sprayed on the forming wire depositing all the fibers on the wire in a single layer.

Although turbulence and drainage forces lead to some preferential positioning of filler and small fiber particles, the fiber arrangement is not significantly altered after deposition on the wire. Hence, the Formette handsheets should be more resistant towards vapor flow on account of their lower permeability.

4.2.5 Infrared Thermographic Analysis

For foaming to begin pressure needs to build up inside the sheets. The time required for pressure build-up is thus important in controlling the rate of foaming. The imaging experiments do not capture the start of foaming until the first bubble is developed to the point where it can be recognized as such by the camera. The build-up of vapor pressure depends both on the sheet permeability and on the rate at which heat is transferred to the sheet. The point at which moisture exits the board to foam the polymeric layer should change the thermal conductivity of the polymer at the bubble surface and affect its temperature to a small degree. The IR camera determines temperature by measuring the total amount of energy emitted by an object. The procedure used in the IR measurements is described in Chapter 3. Thermograms taken of the board surface from laboratory handsheets and machine-made sheets led to the temperature profiles shown in Figure 4.11, which are very similar for the two materials. Certainly, there is no indication that temperature differences contribute to the differences in bubble formation seen in Figure 4.2.

A much larger difference is seen if the coefficient of variation (COV) of the temperature is considered instead of the temperature itself. It has been shown earlier that the COV is a much more sensitive parameter than temperature for identifying subtle thermal effects, such as the point at which a surface just begins to dry [118, 119]. In this example, “dry spots” begin to form on the surface and the variability in the surface temperature rises more sharply than the temperature itself. Figure 4.12 compares the COV profile for the

machine-made sheets and the handsheets during the foaming process. For the machine-made sheets, the COV initially decreases due to the increase in temperature uniformity across the surface. The onset of foaming causes non-uniformities in temperature and thus increases the COV. Thus, the lowest value of COV (at 24 seconds) is believed to signal the start of the foaming process. The temperature and COV profiles presented in Figures 4.11 and 4.12 were consistently observed in all samples investigated as listed in Table 3.4. The standard deviation of temperatures measured across a unit area at different times was less than 2% for all the cases studied.

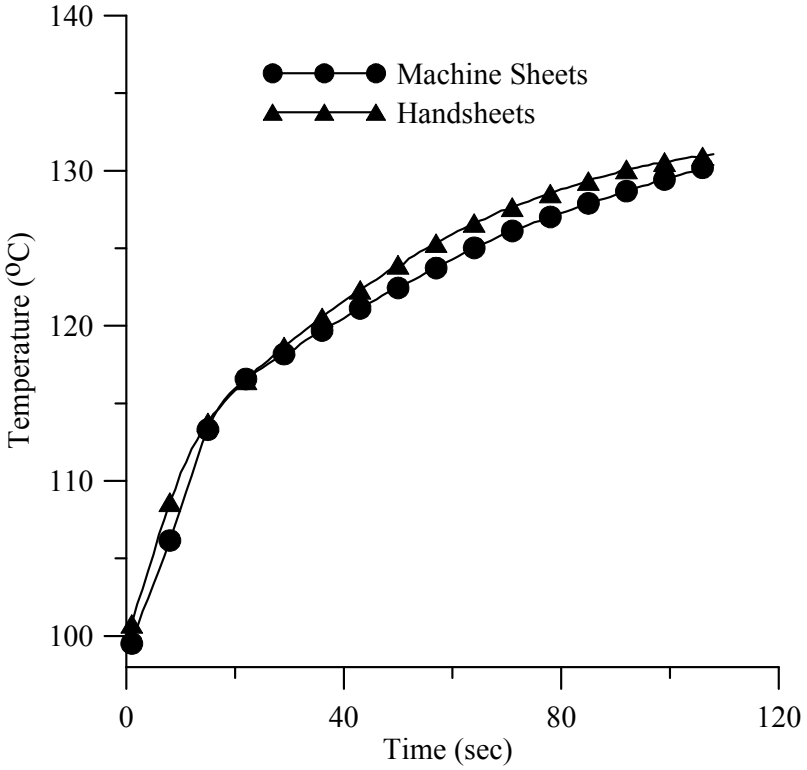

Figure 4.11 Temperature profiles of machine-made sheets and laboratory handsheets.

As in the bubble growth profiles, the COV profiles for all handsheets showed similar trends with changes in sheet composition and other parameters listed in Table 4.1. The

handsheets show an initial increase in COV in the first few seconds. The less uniform surface of a handsheet causes non-uniform heating leading to an initial increase in COV. Upon further heating, the temperature uniformity increases leading to a decrease in the COV.

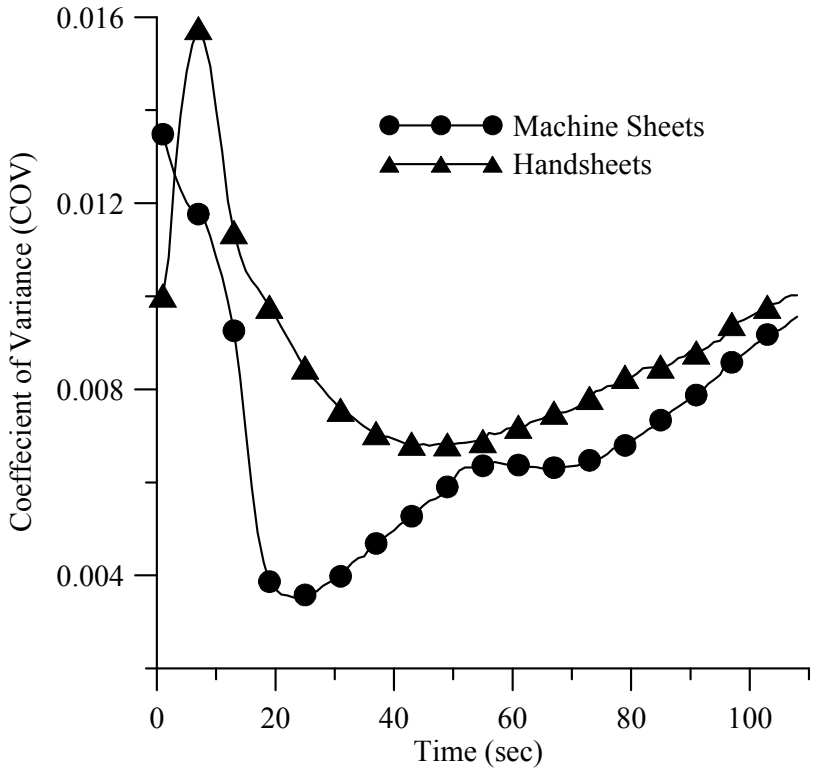

Figure 4.12 Coefficient of variance of temperature profiles for machine-made sheets and handsheets.

However, this decrease is more gradual than that for the machine-made sheets. This implies a slower build up of pressure (corresponding to lower permeability of sheets) leading to slower foaming as observed in the imaging experiments. Since the heating rates for the two sheets were similar, the lower permeability of the handsheets is the reason for the slower growth rate observed.

Traditional foaming, a process well studied in the literature [1-4], involves saturating the polymer with a blowing agent under high pressure. A reduction in pressure leads to nucleation of dense gas bubbles (blowing agent) in the polymeric melt solution. These bubbles, in turn, grow to form the foam structure. Nucleation kinetics and the bubble growth dynamics dictate the foam quality. Factors which could affect such a process include temperature, pressure, nucleating agents, melt rheology and the solubility of the blowing agent. In contrast, the foaming of polymer-laminated paperboard is dictated by the ability of the moisture to travel to and escape from the pores on the surface of the sheet into the molten polymeric layer. The Uniformity Index and the COV results both implicate surface uniformity as the parameter responsible for the difference in behavior between the machine-made sheets and the handsheets. The uniformity of the distribution of pores appears to be critical. Evenly sized and spaced pores give rise to well-distributed bubbles in the foamed product. Thus, the sheet structure is critical to product uniformity.

4.3 Conclusion

In conclusion, we have demonstrated that the foam quality of polymer/paperboard composites depend (in part) on the pore distribution of the paperboard surface. Water vapor from the board escapes through these pores and foams the polymer face, so that the final foamed structure depends on the pore distribution on the surface of the underlying paperboard. On the other hand, the growth rate of the bubbles is dictated by the resistance offered to vapor transport by the paperboard

CHAPTER 5: BUBBLE GROWTH DYNAMICS

5.1 Introduction

The discussion in Chapter 4 focused on the role and properties of the paperboard substrate. The bubble distribution is controlled by a combination of the uniformity of pores on the paperboard surface and the ability of the vapor to travel through the paperboard structure. In this chapter, we identify and discuss the variables that govern the dynamics of bubble and foam growth. Bubble growth is a complex process involving mass, momentum, and heat transfer. The impact of process parameters such as polymer thickness, extrusion speed, the polymer Melt Index (MI), various paperboard properties, temperature and moisture content on foam thickness, and on the number and size distribution of bubbles are evaluated here. The impact of coalescence on bubble size distribution during foaming is also studied. All samples studied in this chapter were extruded onto Machine-made sheets (Sample 'M' in Table 4.1) except those discussed in Section 5.2.4 which includes cases of laboratory handsheets.

5.2 Results and Discussion

5.2.1 Effect of Polymer type

The properties of the polymer should influence the degree of foaming. Three different grades of LDPE differing in their MI values were used as listed in Table 3.2. The MI is inversely proportional to molecular weight and to viscosity; it determines the ability of a

polymer to flow [72]. Figure 5.1 shows bubble growth rate curves for the high and low MI polymers. They are similar, which confirms our earlier conclusion that the bubble number profile during the foaming is dominated by the properties of the paperboard rather than that of the polymer over the MI range used.

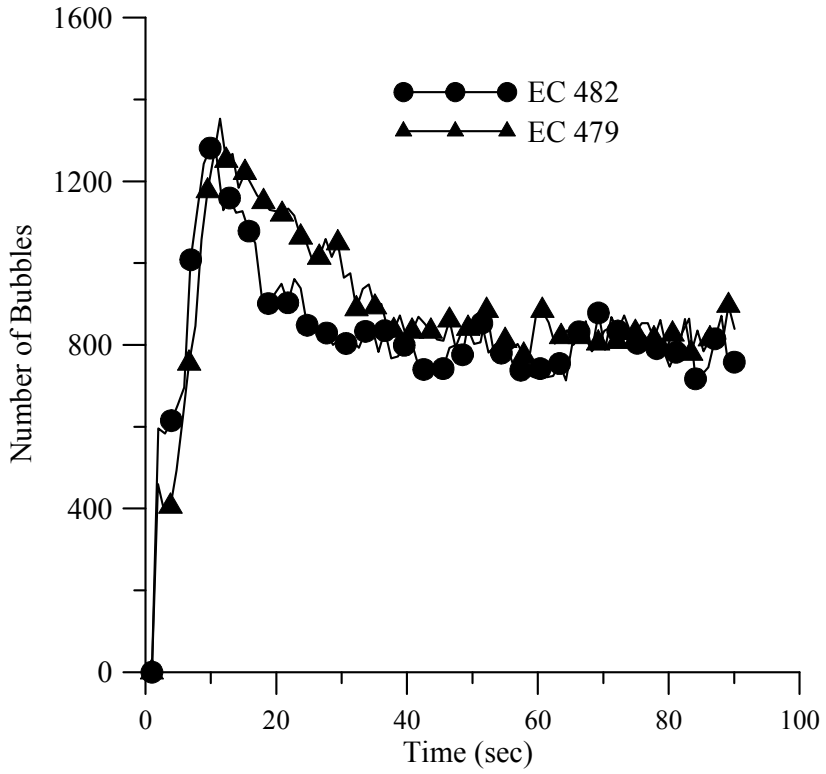

Figure 5.1 Effect of polymer properties on foaming. Melt index for EC 479 – 5.7 gm/10 min and 482 was 12 gm/10 min. Polymer extruded at 137 m/min to 42.2 µm thickness.

The foam thickness values are determined by subtracting the initial from the final thickness and are plotted for the high and low MI polymers in Figure 5.2; the thickness values are similar, implying that the polymer melt index (which would directly affect the viscous forces opposing the bubble growth) play an insignificant role in the foaming process in the range of MI values studied here.

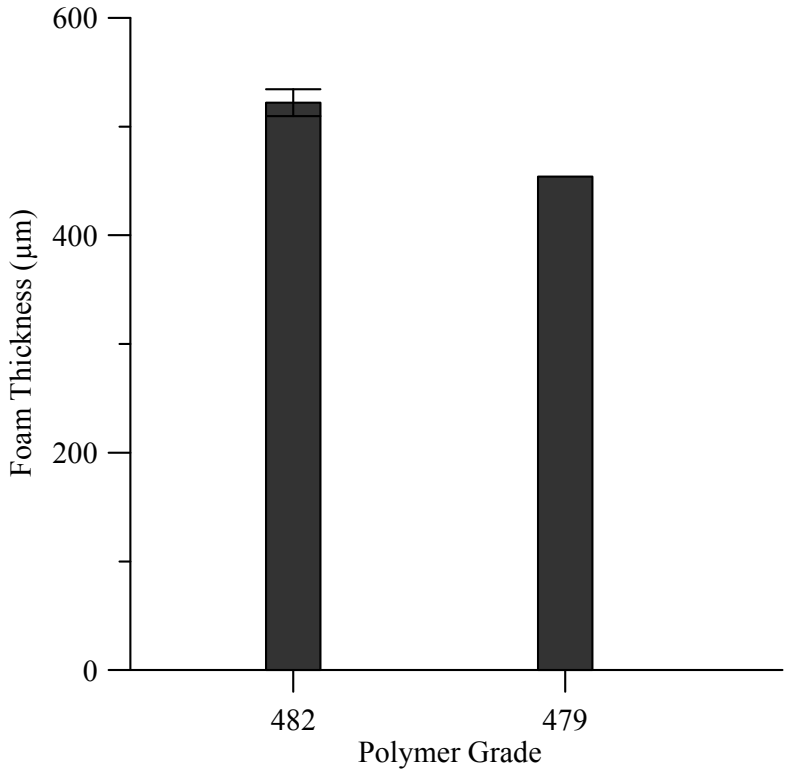

Figure 5.2 Effect of polymer melt index on the foam thickness. Melt index for EC 479 – 5.7 gm/10 min and 482 was 12 gm/10 min. Polymer extruded at 137 m/min to 42.2 µm thickness.

5.2.2 Effect of Polymer Film thickness

LDPE grades were extruded to different thickness values ranging between 17.7 µm and 42.2 µm to study its effect on foaming. The maximum and final bubble count and the degree of coalescence were measured as a function of initial thickness of the polymer film. The results, shown in Figure 5.3, demonstrate that these values are largely independent of film thickness. This is expected because the pore distribution of the paperboard surface controls the bubble distribution, and the effect of film thickness should be small, at least within the range used. In principle, a thicker polymer would

cause fewer or smaller bubbles to grow on account of the larger resistance forces. This is not the case in Figure 5.3 implying vapor driving force dominates over all resistance forces.

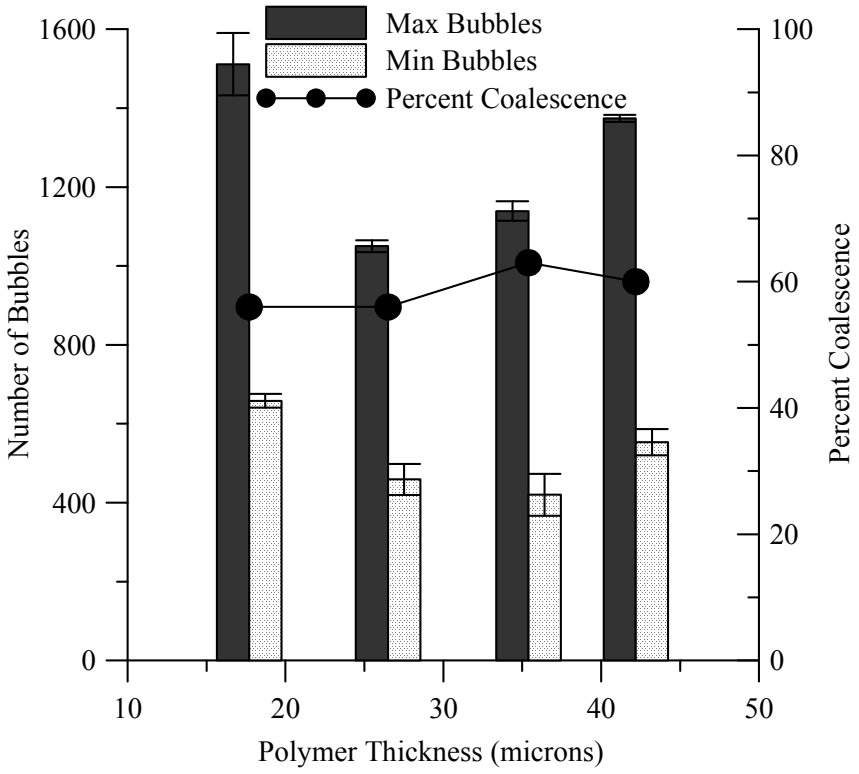

Figure 5.3 Effect of polymer (EC-482) thickness on bubble growth. The extrusion speed was 61 m/min.

Figure 5.4 illustrates the relationship between the final foam thickness and the thickness of the initial polymer film. Surprisingly, the thicker film gives rise to the thicker foam even though it must offer greater resistance to foaming. Since, the vapor force dominates, the opposition force does not play a role in stopping the bubble growth. On the other hand, the bubble size is limited by the bubble wall thickness which balances the bubble pressure. A thicker polymeric film leads to thicker bubble (cell) wall, reduces the fraction of the bubbles that burst. This is further elaborated on in Chapter 6.

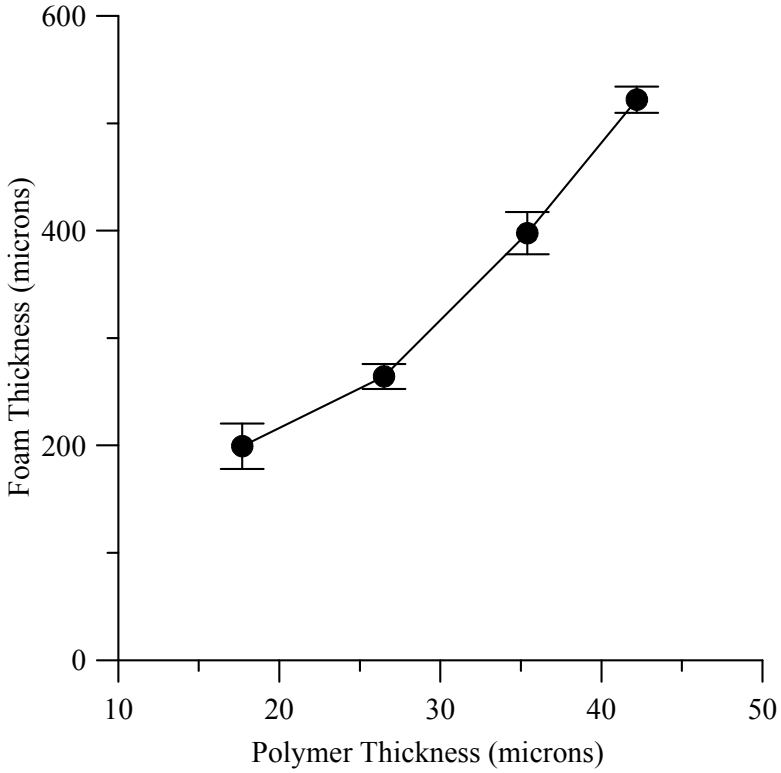

Figure 5.4 Effect of polymer (EC482) thickness on foam thickness. The extrusion speed was 61 m/min

The foam thickness would also be reduced if some of the bubbles had burst. However, this did not occur to any significant extent; the images showed that the majority of the bubbles retained their integrity during foaming.

Polymer adhesion also plays a role in the foaming process. Adhesion occurs by both mechanical and chemical bonding. Mechanical adhesion dominates for porous substrates such as paper or paperboard where the polymer physically penetrates the fibers or the pores. Higher coat weights increase adhesion due to a closer contact between the polymer and the fibrous surface [56]. The amount of polymer that gets nipped between the voids of the fibers also increases. Heavier coating weights carry more heat to the paperboard

leading to better adhesion [56, 57]. This leads to better bonding with the paper surface. A higher level of bonding would increase the vapor driving forces causing an increase in foam thickness with higher coated weights (thicker polymeric films).

Also, most likely, the foam thickness reflects the maximum rather than the average thickness because the platen surface would contact the larger bubbles. Measurements made with either soft or hard platens gave similar trends within 5%, indicating that the foam was not significantly crushed during the measurement. Again, this indicates that it is the maximum foam thickness that is being measured.

5.2.3 Effect of Extrusion

The physical properties of the interface between polymer and paperboard depend upon the method of extrusion [63-65]. A polymer extruded on the board experiences a number of changes to its structure. During extrusion, a thin film of molten polymer is pressed on to the paperboard. Parameters such as line speed, extruder temperature profile, chill roll temperature, and press roll pressure all affect the properties of the interface. Different morphological properties of the polymer are also influenced by variations in these process conditions [63-65].

LDPE is known to have excellent adhesion to kraft paperboard. LDPE is non-polar in nature and the melt oxidizes in the air gap between the die and the nip to form oxidized polar functional groups [54]. Oxidation leads to the formation of stronger bonds between

the paper and the polar surface groupings. The extrusion speed determines the residence time of polymer in the air gap. The residence time directly relates to the degree of oxidation that the polymer melt undergoes [59]. At very high line speeds (low residence times), the degree of oxidation deteriorates to a point where there is not enough time for the oxidation process to be initiated, and the adhesion drops. Line speed also affects the shear forces applied to the polymer and influences the orientation of polyethylene chains [63].

SEM images of paper/polymer interfaces showed the presence of open flat bubbles at the interface, which was attributed to the evaporation of water from the paper caused by heat flow during extrusion which could affect the pore activity in foaming (Figure 2.10). These effects are discussed further in Chapter 2. The three extrusion line speeds used here were chosen to mimic those employed commercially. IR thermography was used to confirm that the temperature of the board during foaming exceeded that of the DSC melt point (varied between 106^{o}C and 110^{o}C) of the polymer. Figure 5.5 shows the effect of extrusion speed on the coalescence rates, which decreased at the higher extrusion speed of 213 m/min compared to 137 m/min.

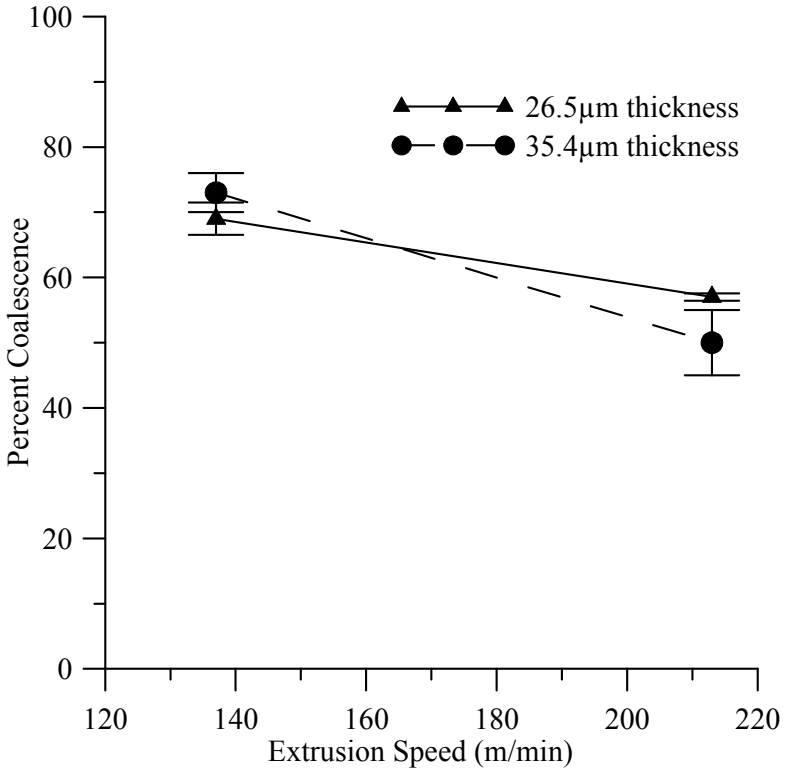

Figure 5.5 Effect of extrusion speed on bubble growth for the EC 476 polymer.

The extrusion speed did not have a significant influence on the number of bubbles formed, which implies that any changes in interfacial properties caused by differences in extrusion do not affect the pore activity during foaming. However, Figure 5.6 shows that foam thickness decreases with increasing extrusion speed, which is known to decrease the adhesion of the polymer to the board [58, 59]. Poorer bonding between polymer and paperboard would promote vapor leakage from the interface during foaming and lead to smaller bubbles. As expected, the thinnest foam was observed at the highest extrusion speed and with the lowest polymeric thickness. The vapor leakage could also be a reason for the decreased coalescence at higher extrusion speeds.

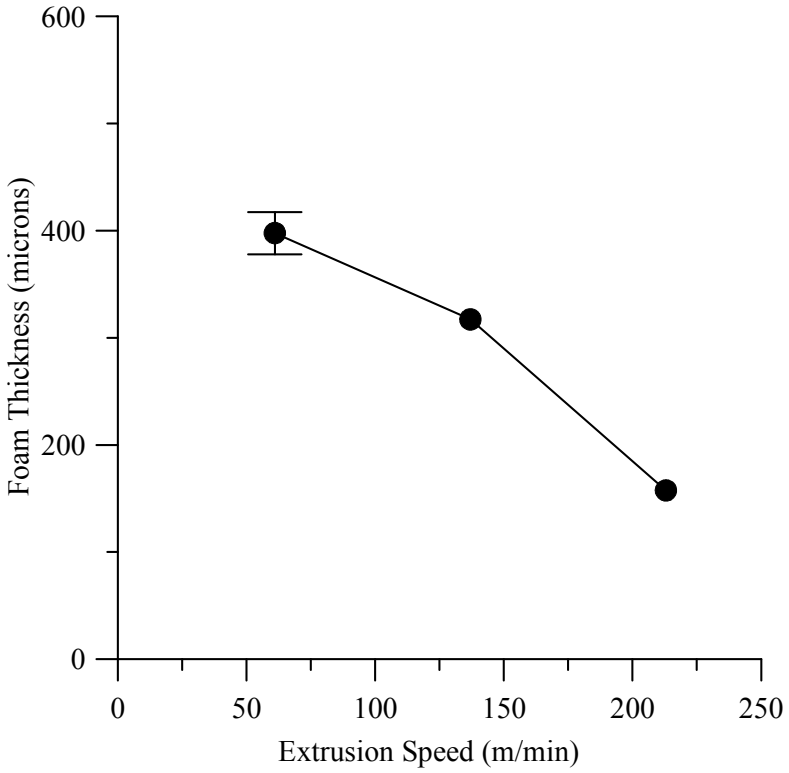

Figure 5.6 Effect of extrusion speed on foam thickness for EC 482 polymer. The film thickness was 35.4 µm.

5.2.4 Effect of paper substrate properties

In Chapter 4 it was shown that the number of bubbles formed is related to the surface uniformity of the pores and the resistance to vapor transport inside the board. Images of bubbles generated under two different conditions are shown in Figure 5.7. The paperboard used in Figures 5.7a and 5.7b were made in the laboratory as described in Chapter 3 and was less uniform than the machine-made board which is represented by Figures 5.7c and 5.7d. The furnish used in both cases was a mixture of 75% southern hardwood and 25% southern softwood.

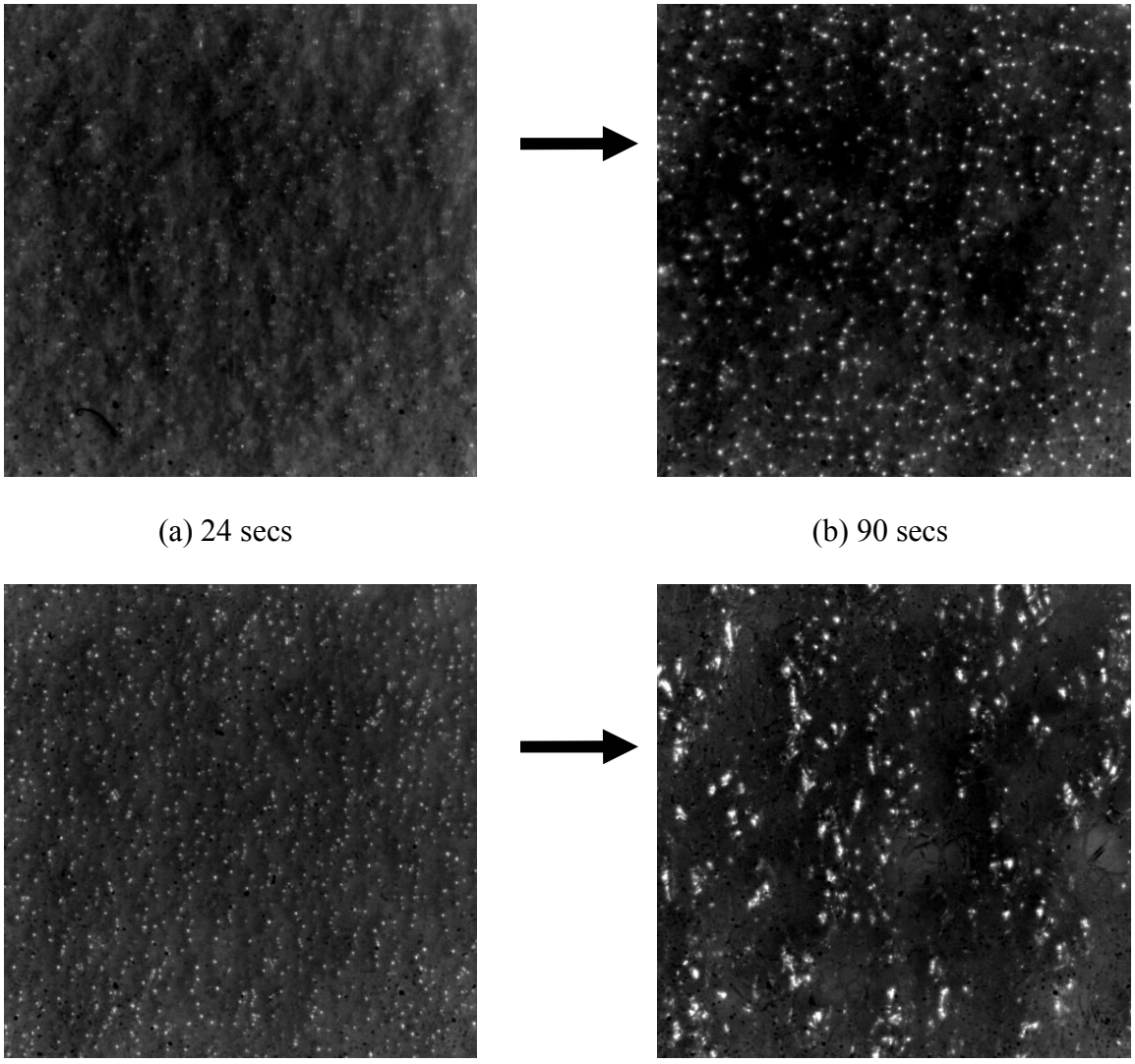

(a) 24 secs (b) 90 secs

(c) 20 secs (d) 90 secs

Figure 5.7. Effect of coalescence on the bubble size distribution. Panels (a) and (b) represent handsheets; panels (c) and (d) represent machine-made paper. Both sheets were made from a mixture of 75% hardwood and 25% softwood and refined under the same conditions to freeness levels of 500 ml CSF.

The bubbles on the machine-made paper coalesced to a greater degree than those on the handsheets due to bubbles being more closely spaced compared to their handsheet counterparts. The more uniform surface and lower resistance to the transport of vapor give rise to a larger number of bubbles and a higher coalescence rate as discussed in Chapter 4.

Figure 5.8 shows that the foam thickness is less sensitive to paper properties than it is to properties of the polymer such as film thickness (Figure 5.4). The machine-made paper leads to thicker foam as compared to the handsheets because of its lower resistance to vapor transport.

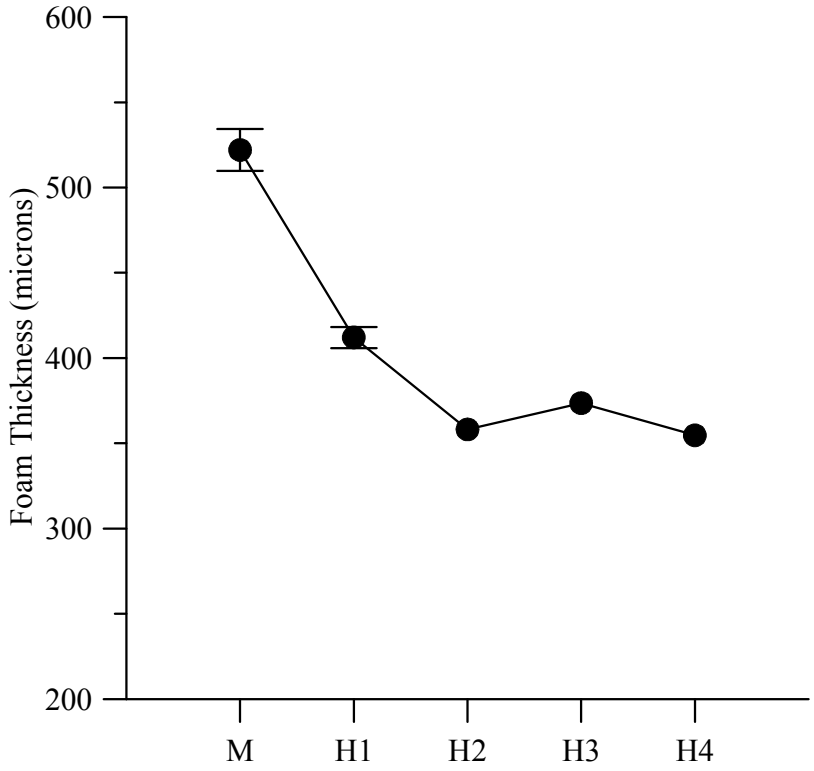

Figure 5.8 Effect of paperboard (M: machine-made, H: handsheets) properties on foam thickness. The hardwood:softwood ratios are 1-100:0, 2-75:25, 3-50:50, 4-0:100. 'M' sheets were refined to 500 ml CSF. 'H' sheets were refined to 300 ml CSF. LDPE EC 482 polymer was extruded at 61m/min to 42.2 µm thickness.

5.2.5 Effects of temperature and moisture content

Foaming experiments were carried out at different oven temperatures ranging from 120°C to 150°C. The DSC melt point of the polymers employed in this study varied between 106°C and 110°C. Once the board is placed inside the oven, foaming does not begin until the polymer begins to melt. As long as the operating temperature lies above the DSC melt point of the polymer no significant differences in foam quality were observed with variation in foaming temperature as shown in Figure 5.9.

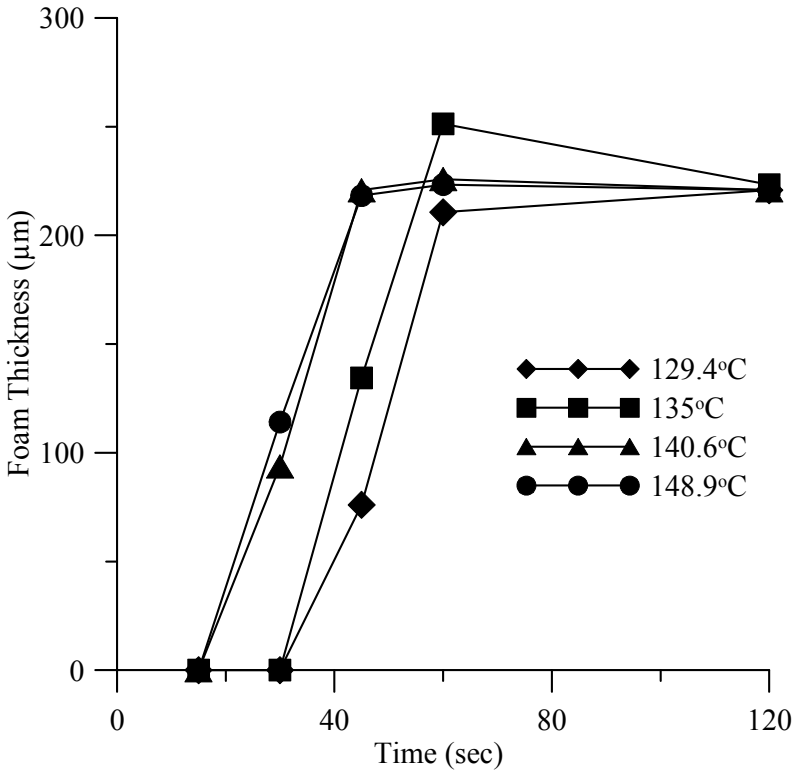

Figure 5.9 Variation of foam thickness at different temperatures. LDPE EC482 polymer was extruded at 137 m/min to a thickness of 42.2 µm. The time starts from the point at which the board was placed inside the oven.

The data shown in Figure 5.9 are from foaming carried out in a commercial set up. Laboratory results showed similar trends. Experiments were conducted with a conditioned and an unconditioned board. The moisture varied between 4 and 8% for the conditioned board, and was 2% for the unconditioned case. Although, foaming occurred at all moisture contents between 2 and 8%, the best results were obtained for the conditioned case. The role of moisture is further discussed in Chapter 6.

5.2.6 Bubble size distribution

Coalescence involves interaction between bubbles, with small bubbles combining with each other or with a larger bubble. The bubble size at foaming intervals was determined by tracking the reflected light from the bubble surface using the Image J software as described in Chapter 3. An appreciation of the variation in bubble size distribution is obtained by comparing two cases which differ in the degree of coalescence. Figure 5.10 shows the size distribution resulting from two extrusion speeds: 213 m/min (low degree of coalescence) and 137 m/min (higher degree of coalescence).

The bubbles are divided into three bins of increasing size. The bin 1 bubbles are formed early in the process. Each originates from a single pore in the paperboard implying a direct dependence on the pore size distribution of the paper surface. This was confirmed from imaging studies in the early stages of the foaming before the onset of coalescence. The bin 1 bubbles are the most numerous. They decrease rapidly due to coalescence leading to bubbles in bins 2 and 3.

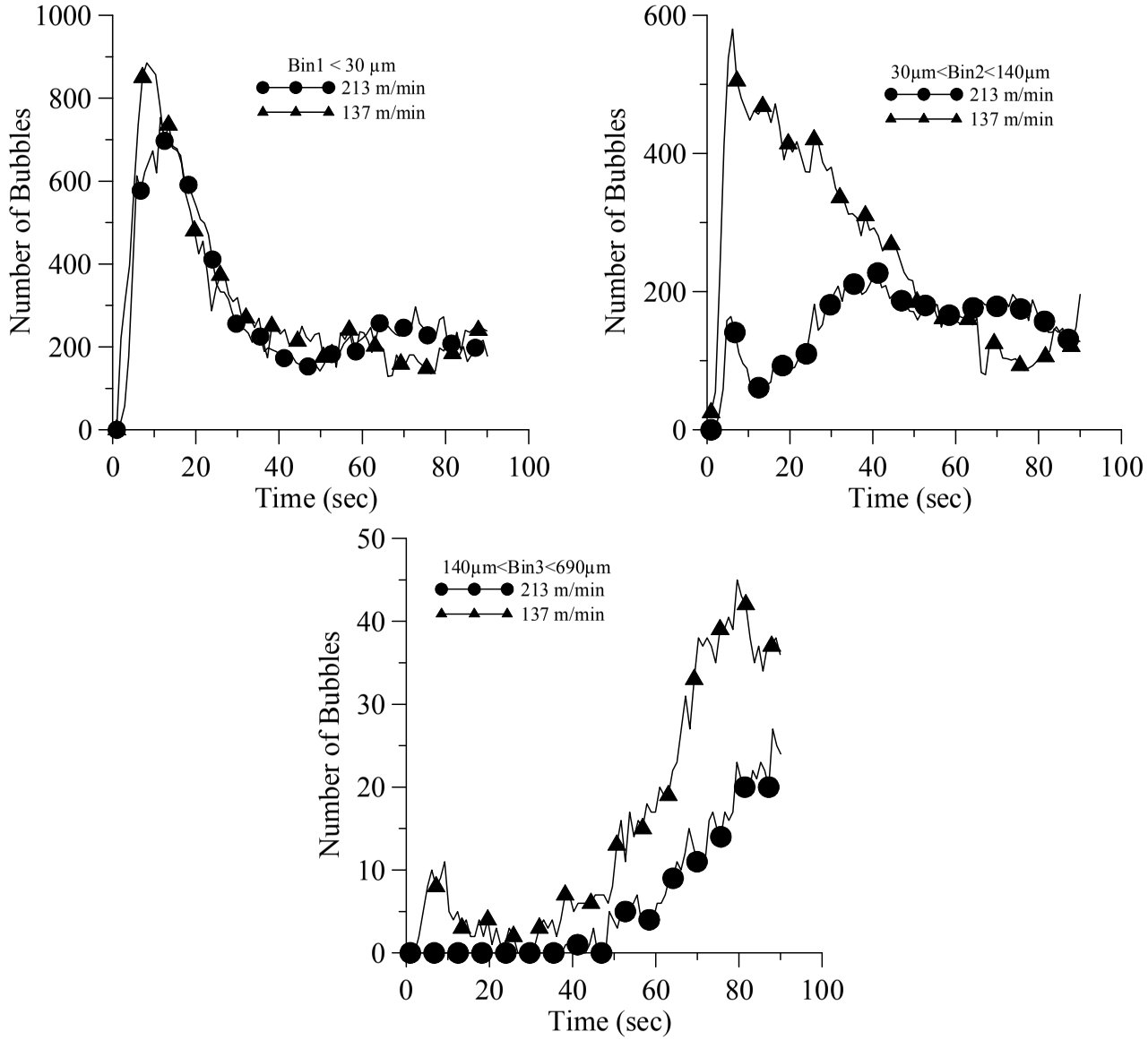

Figure 5.10 Bubble size distribution on board during foaming at low and high extrusion speeds; LDPE EC-476 polymer was extruded to 35.4µm thickness.

Fewer large bubbles are formed at the higher extrusion speed because of reduced coalescence. Some bin 2 bubbles are formed early in the process due to the presence of a few larger sized pores.

The position of each bubble was tracked during foaming. Coalescence is most likely to occur between adjoining bubbles; *e.g.* for the clustered bubbles in Figure 5.7d as opposed to the isolated ones. The distance between a bubble and its nearest neighbor was calculated for all the bubbles in the image. The standard deviation (SD) of the mean of these distances drops sharply and levels off at about ten seconds as shown in Figure 5.11.

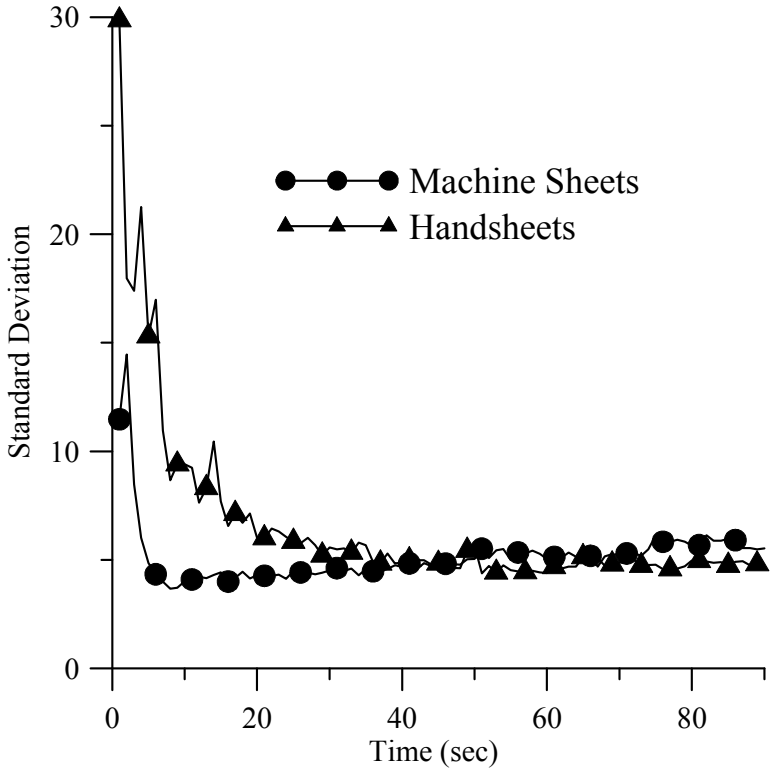

Figure 5.11 Variation of standard deviation of the shortest distance between bubbles

A wide spread of bubbles during the first few seconds causes the SD to be high in the first few seconds. The number of bubbles in bin 1 in Figure 5.10 also peaks at ten seconds indicating that coalescence begins at this point. The machine-made sheets experience a much faster decrease in SD values as compared to handsheets implying a more uniform growth of bubbles across the board, as expected.

5.3 Conclusion

This study elaborates on the mechanism of foaming on paperboard and identifies the different dependencies that the bubble count and foam thickness have on paperboard and polymer properties. There are two elements to foaming: the number of bubbles and the thickness of the foam. The bubble count is controlled by the uniformity of the paperboard surface. Foaming is caused by water vapor escaping from the board through the pores at the interface and into the molten polymer. Thus, the distribution of the paperboard pore structure controls the number of bubbles formed and their distribution. Clustered bubbles are able to coalesce and grow. As expected, the properties of the polymer and the film thickness do not influence the number of bubbles created, at least within the range studied. In contrast, the thickness of the foam depends principally on the bonding ability of the polymer to the paper and on the polymer thickness. The foam thickness fell as the extrusion speed at which the polymer was deposited on the paperboard increased. It is likely that the faster speed caused poorer bonding between the polymer and the paperboard and promoted vapor leakage from the interface during foaming. A thicker extruded polymer film also led to thicker foam.

CHAPTER 6: FACTORS INFLUENCING BUBBLE SIZE

6.1 Introduction

Foam quality plays an important role in the commercial applications of foamed paper-polymer composites. Their quality is dictated by their insulation properties which makes them suitable for food packaging applications such as coffee cups. The density reduction obtained due to the dispersion of gas bubbles at the paper-polymer interface gives foams its insulation properties [27]. The low thermal conductivity due to negligible heat convection in the gas phase leads to the good insulation properties of foams. The cell size distribution determines the amount of gas dispersed.

In previous chapters we have shown that bubble growth is driven by the vapor driving force and is principally controlled by the uniformity of pore size across the paper-polymer interface. The bubble density of the final foamed structure depends on the pore distribution of the surface of the paperboard. The bubble size on the other hand is controlled by the polymer phase and its bonding ability with the paper surface. In this chapter we analyze the role of vapor (moisture), pore size and the degree of coalescence on the final bubble size and foam quality. Table 6.1 lists the properties of the various samples investigated and their respective void volumes. Void percentage was calculated as the fraction of gas volume present in the polymeric phase.

Table 6.1 Properties of Samples Investigated

No.	Polymer Grade	Extrusion Speed (m/min)	Polymer thickness (μm)	Foam thickness (μm)	Void (%)
1	482	61	42.2	522	93%
2	482	61	35.4	401	92%
3	482	61	26.5	271	91%
4	482	61	17.7	205	92%
5	482	137	35.4	292	89%
6	482	213	26.5	191	88%
7	482	213	17.7	168	90%
8	479	137	42.2	404	91%
9	476	137	26.5	302	92%
10	476	137	35.4	296	89%
11	476	137	42.2	114	73%
12	476	213	17.7	136	88%
13	476	213	26.5	162	86%
14	476	213	35.4	204	85%

6.2 Results & Discussion

6.2.1 Vapor loss measurements

Foam thickness is directly related to the bubble size. Figure 6.1 shows that foam thickness reaches a maximum value after which bubble collapse returns it to its initial pre-foamed level. This behavior was also observed in the foaming videos reported in Chapter 4. The maximum bubble size should depend on the balance between the forces that drive growth and those that oppose it.

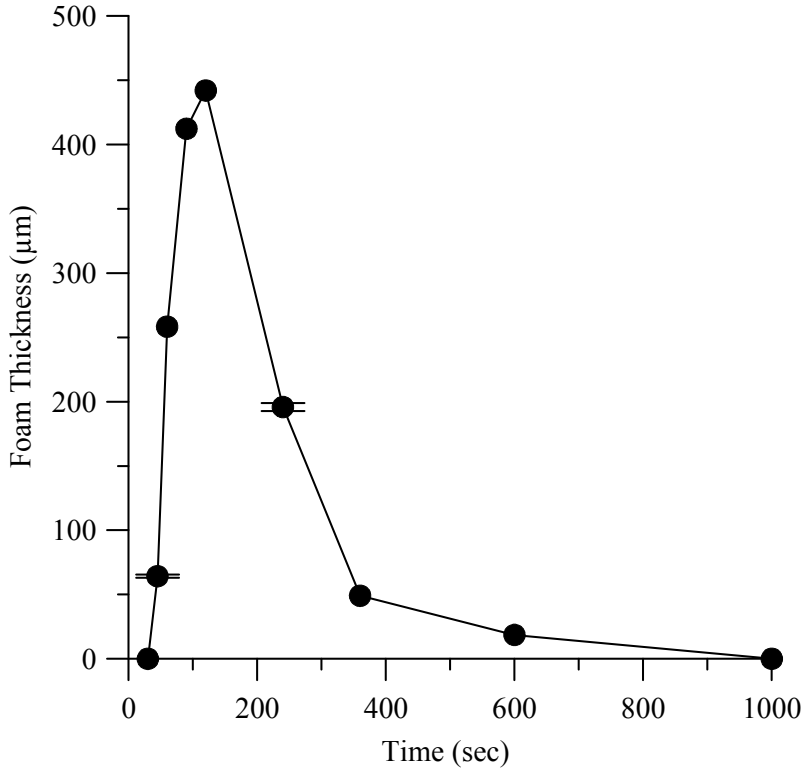

Figure 6.1 Typical variations in foam thickness with time.

During growth, the vapor driving force overcomes the opposing resistance forces as discussed in Chapter 5. The vapor driving force is a function of the rate of vaporization and the sheet resistance to vapor flow. Vapor loss during foaming was measured to gain a better understanding of its role in foaming. Results from the vapor loss measurements are shown in Figures 6.2 and 6.3. Figure 6.3 is a subset of Figure 6.2 and is included here to highlight changes in moisture levels over the first 120 sec. All the samples listed in Table 6.1 showed similar levels of moisture loss during foaming.

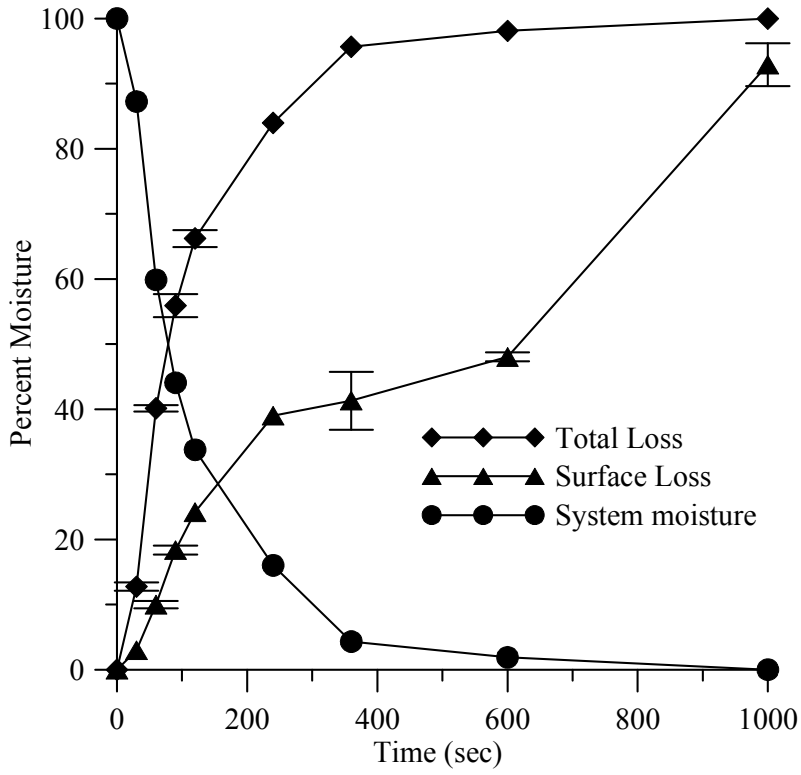

Figure 6.2 Vapor loss measurements during the foaming.

Vapor can escape from the board through two avenues – the paperboard edge or the polymer-paperboard interface. Interfacial moisture can escape either through the edge or the surface of the board. Most of the vapor is lost from the board after about 400 seconds as seen in Figure 6.2. The percentage of vapor lost through the surface is a significant percentage of the total vapor lost; the loss occurs through vapor leaks through the molten polymeric film during foaming. This could happen if some of the bubbles burst or if the vapor diffuses through the polymeric film.

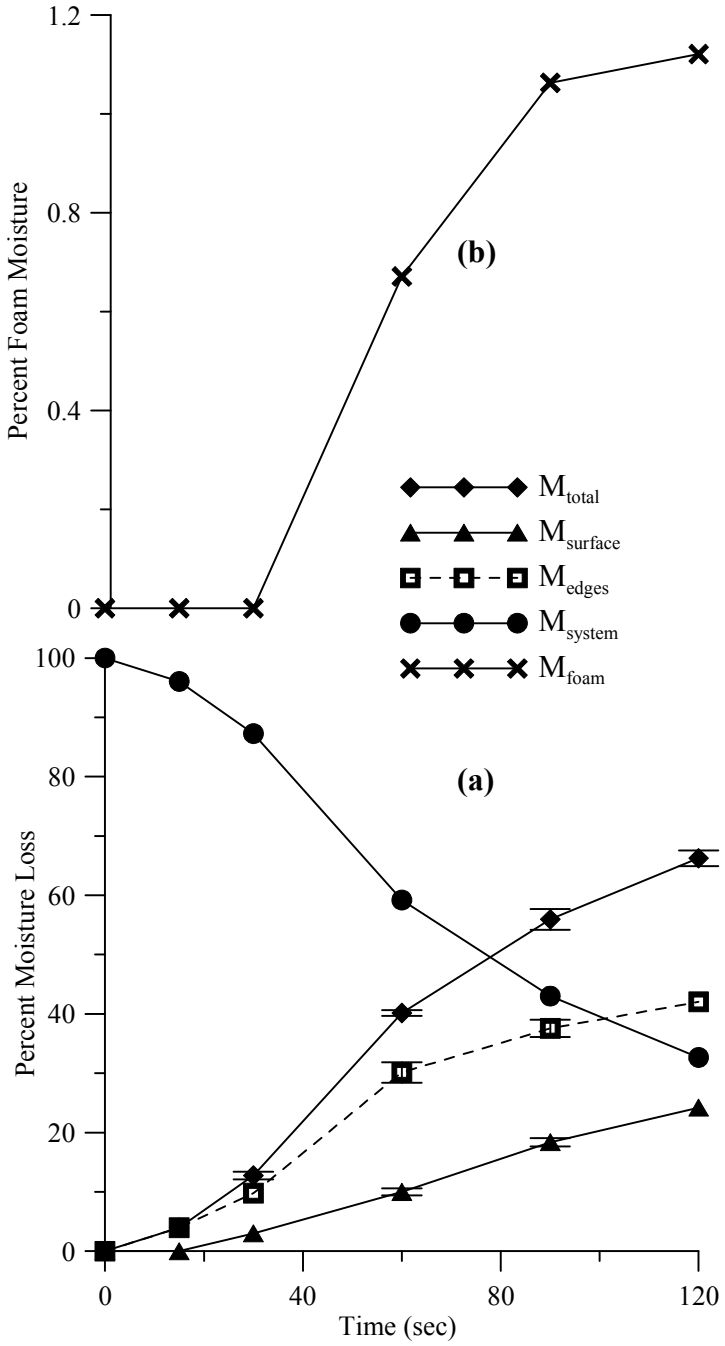

Figure 6.3 Moisture mass balances during foaming. Panel (a) shows the percentage of moisture lost. Panel (b) shows the percentage accumulation of moisture inside the foam.

A mass balance on the different components of moisture in the system can be written as –

$$M_{total} + M_{foam} + M_{system} = M \quad (6.1)$$

Where M_{total} is the sum of loss of moisture through surface ($M_{surface}$) and through the edges (M_{edges}).

A small percent of moisture (vapor) escapes through the surface during the initial stages of foaming. This is mostly due to the smaller bubbles collapsing in the initial stages of the process as observed in the imaging experiments discussed in Chapter 4. Diffusion is not likely to occur over such short time scales. Figure 6.3 also shows that the vapor loss through the edges occurs at roughly the same rate as that through the surface, which is expected because both are governed by the vaporization rate. The DSC melt points of low density polyethylene used here varied between 106 and 110^{o}C. The vaporization starts before the polymeric layer on the foaming side melts and causes the loss from the edges to begin earlier than that from the surface.

Less than 2% of the total initial moisture accumulates inside the board as seen in Figure 6.3b. This implies that there is several times more moisture present inside the board than is needed for foaming. The optimum bubble size is thus not limited by the amount of moisture present inside the board, but by the properties of the polymer film that forms the foam cell (bubble) wall. The vapor flow rate is, in part, controlled by the pore opening which feeds the flow into the bubble.

6.2.2 Pore size analysis

A paper sheet is a complex structure containing several tortuous channels and pores [74]. A typical surface SEM image illustrating the wide distribution of pore sizes in the paperboard used in this study is shown in Figure 6.4a. The exact size distribution of pores is difficult to determine for each of the various paper samples used in foaming. Hence, the pore distribution was approximated by manually determining the areas of 500 individual pores on the paper surface using Image J software [128] from eight different regions of the paperboard. Figure 6.4b shows an example of the different areas in the SEM image identified as pores. The pore sizes were found to vary between 2 and 40 μm as shown in Figure 6.5.

These values represent the sizes of pores on the paper surface. Figure 6.6 shows a typical example of the distribution of maximum number of bubbles formed during foaming. The pore size distribution profile provided in Figure 6.5 is similar to the bubble distribution profile shown in Figure 6.6, which confirms the validity of the assumptions used to construct Figure 6.5. A log normal distribution could be used to fit the pore distribution in Figure 6.5. The cross-section of a pore in paperboard can assume various shapes. Two possible shapes, conical and cylindrical are illustrated in Figure 6.7. The vapor flow rate will depend on the radius ‘r’ of the pore opening.

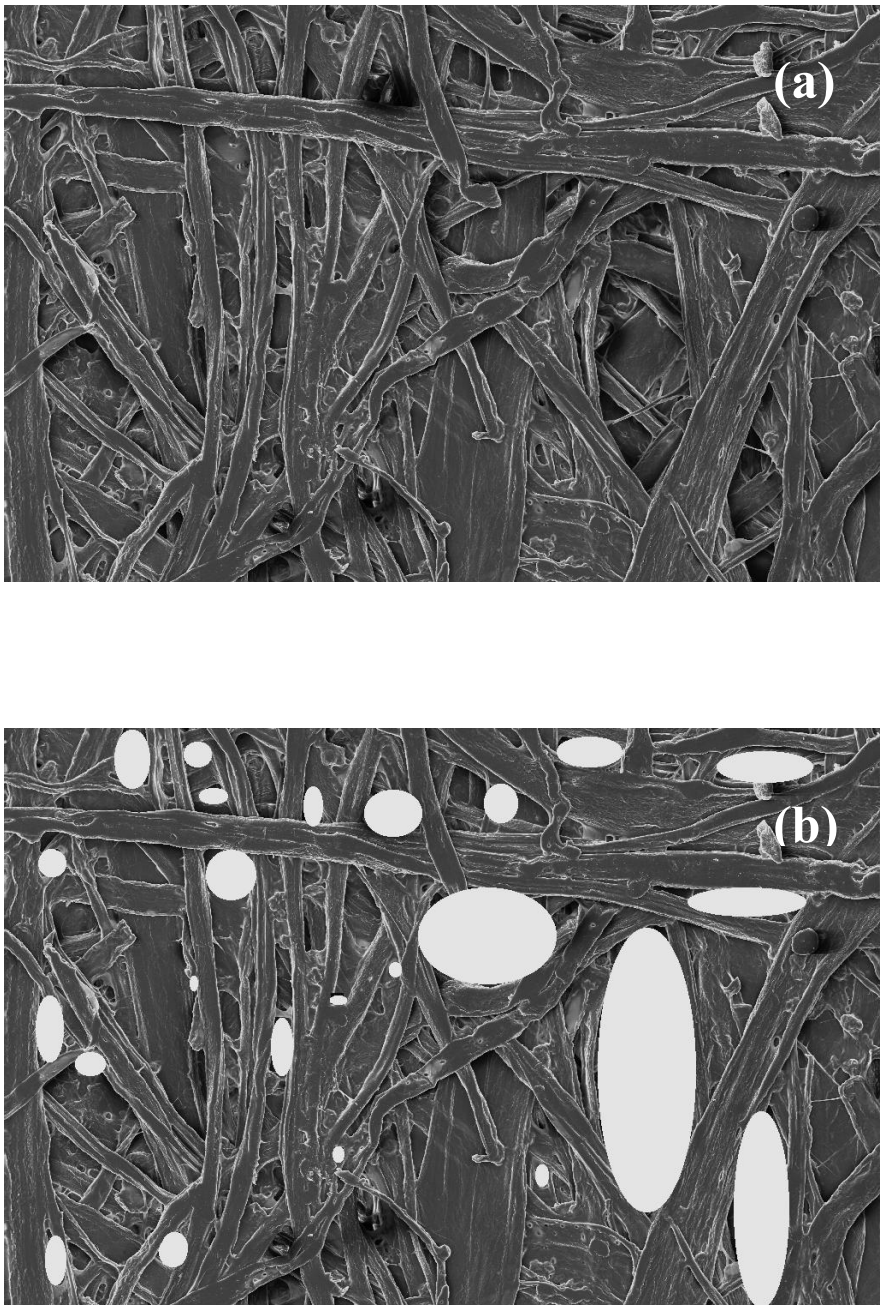

Figure 6.4 (a) SEM surface image of paperboard used in foaming (b) example of pore areas marked and used to determine pore size distribution.

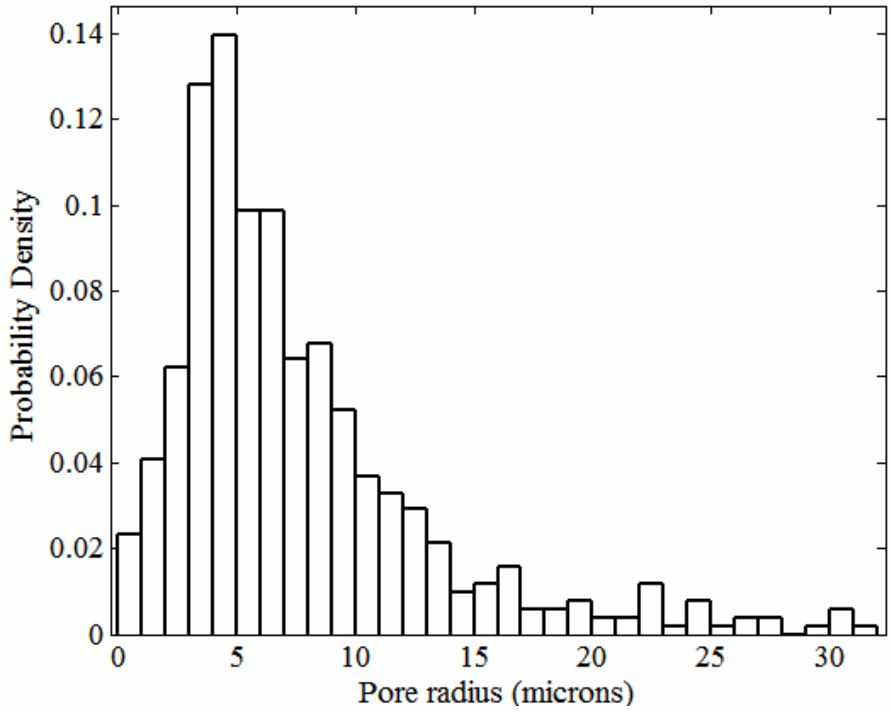

Figure 6.5 Pore size distribution on the surface of paperboard used in foaming.

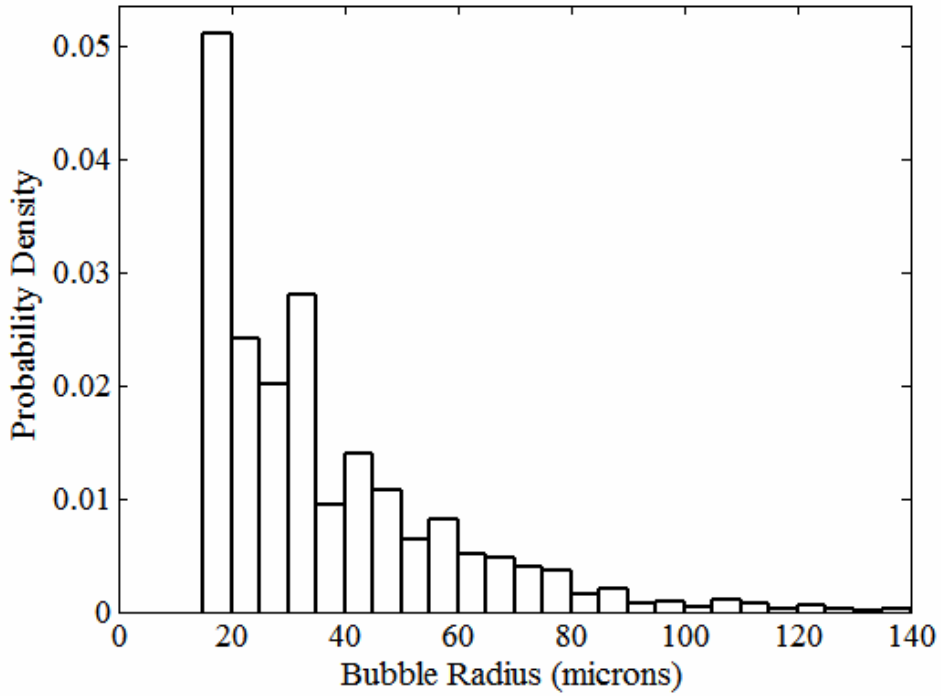

Figure 6.6 Typical size distribution of bubbles formed.

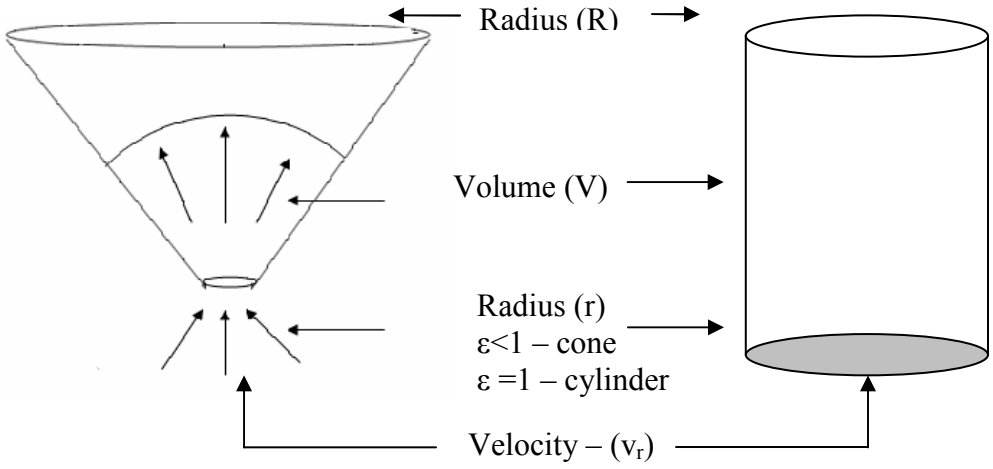

Figure 6.7 Conical and cylindrical pores assumed in the analysis.

The pore base radius 'R' should reflect the amount of polymer that covers the pore at the paper-polymer interface. To determine the pore opening radius 'r' from the surface pore distribution ('R'), we assume a linear relationship as in eq (6.2).

$$r = \varepsilon R \tag{6.2}$$

A value of $\varepsilon<1$ would account for a cone shaped pore while $\varepsilon=1$ would correspond to a cylinder. Thus, different 'ε' values are likely depending on the size and shape of pores. SEM cross sections of pores after 10 seconds of foaming are shown in Figure 6.8; the linearity between r and R is apparent.

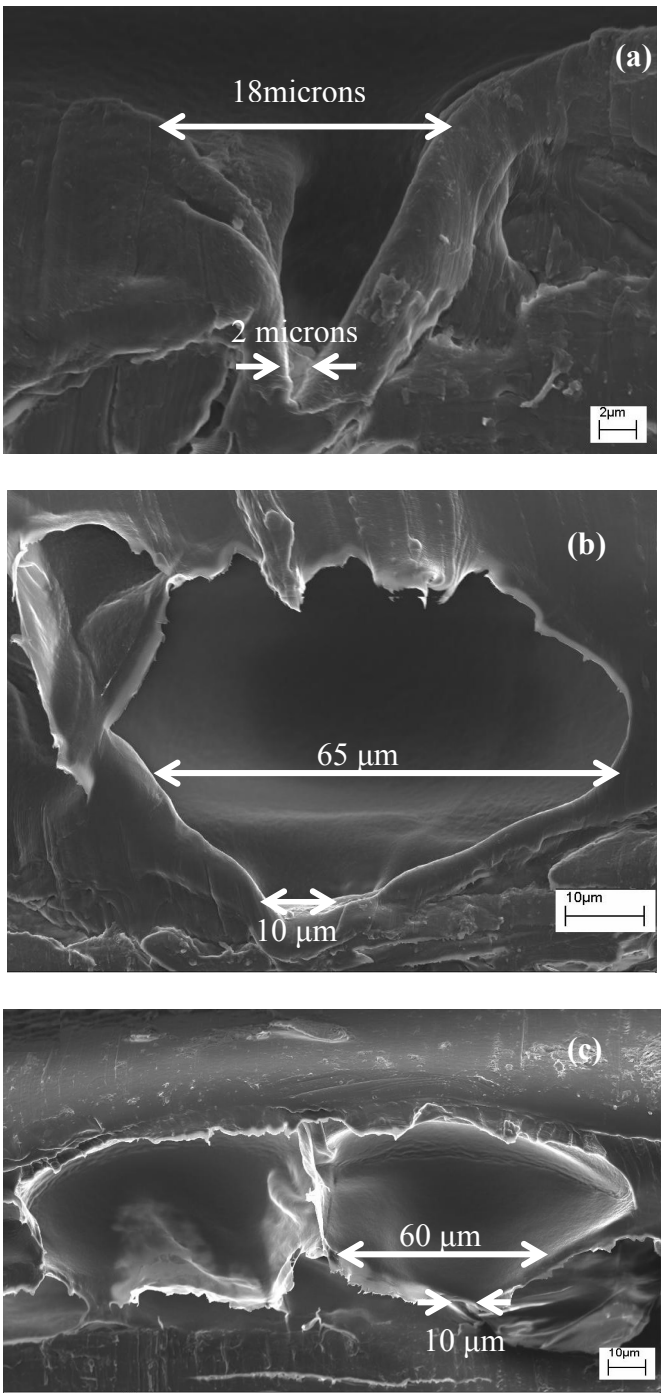

Figure 6.8. SEM cross sections of pore from board foamed for 10 secs. Values of 'ε' are (a) 0.11 (b) 0.15 (c) 0.16

6.2.3 Theoretical Maximum Bubble size

It has been established that the vapor driving force dominates the process. Thus, the maximum bubble size could be predicted from the rate of vapor flow into the pore. Vapor transport in the present case represents restricted flow between two polymeric layers and is expected to create a pressure gradient across the board in the thickness direction. This will lead to a convective bulk flow of the type observed during paper drying [100].

The maximum bubble volume can be estimated from eq (3)

$$\frac{d}{dt}(\rho V) = \rho \cdot v_r \cdot \pi r^2 \qquad (6.3)$$

where V is the volume of the bubble, v_r is the flow rate of the vapor into the pore, ρ is the density of vapor, r is radius of pore opening.

The flow rate was determined from the vapor loss measurements discussed in Chapter 3. The transport rate (v_r) into the pore will depend on the rate of vaporization and the resistance offered by the porous structure, *i.e.* the permeability. This can also be determined by the total mass flow rate of vapor lost in the thickness direction ($M_{surface}$) and the rate of vapor accumulation inside the board (M_{foam}).

The vapor flow rate would thus be equal to -

$$v_r = v_{foam} + v_{surface} \qquad (6.4)$$

where v_{foam} and $v_{surface}$ represent the velocity of vapor accumulation inside the foam and flow through the surface, respectively.

To account for the different sizes of pores on paper surface, we vary the 'ε' values between 0.1 and 10; the maximum bubble radius calculated for the corresponding pore radii between 0.02 and 400 μm is illustrated in Figure 6.9.

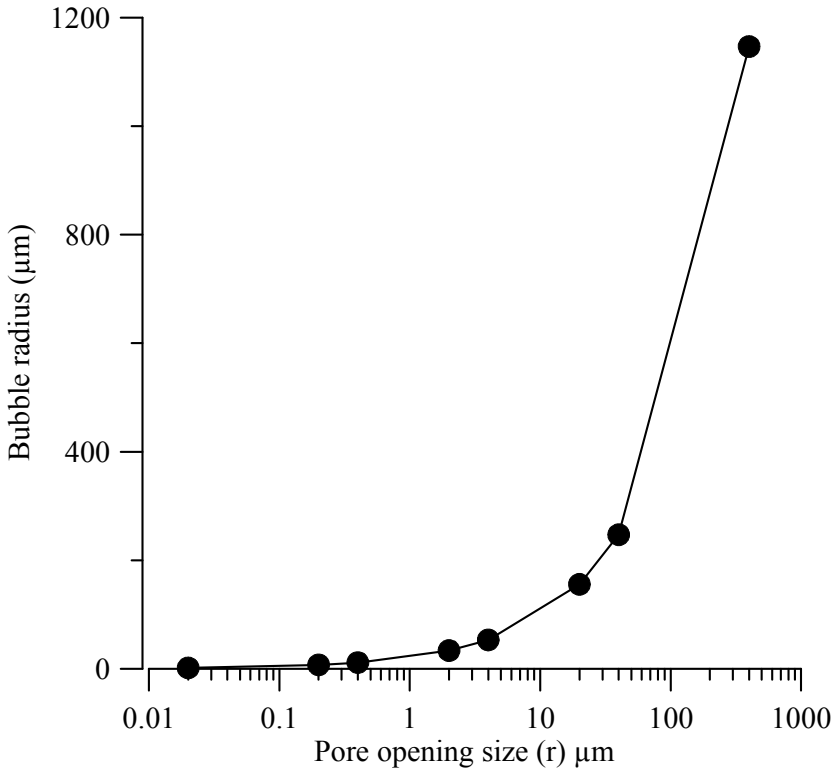

Figure 6.9 The maximum bubble size calculated from convective flow into the bubble for different sizes of pore openings.

The maximum theoretical bubble size varies between 5 and 1200 μm. The average bubble size on the other hand as illustrated later in the chapter in Figure 6.12 varies between 20 μm and 260 μm. Thus all bubbles do not grow to the theoretical maximum bubble size because most of the vapor is lost through the surface.

The void volumes in the final foam directly relate to the bubble sizes and are listed in Table 6.1 for the various cases studied. By and large the void volume remains unchanged for the different extruded polymer thickness values employed. The amount of polymer that contributes to the bubble will depend on the volume of the polymer (thickness and area) which covers the pore opening. A larger pore would have a larger volume of polymer contributing to the bubble; similarly a thicker extruded polymer would lead to a larger volume. As a bubble grows its surface area increases. Since the volume of polymeric material which encloses the bubble remains the same, the bubble (cell) wall thickness decreases with an increase in size. The bubble collapses at the point at which the bubble wall thickness can no longer balance the bubble pressure.

Although the vapor flow rate is important, the limiting size of the bubble is dictated by the volume of polymer which expands as the bubble grows. A larger pore leads to a larger bubble for two reasons – a larger volume of vapor flowing through the pore, and the presence of a larger volume of polymer that allows the bubble to grow larger before the bubble wall thickness reaches the yield point. For the same pore size, a thicker film would lead to a larger bubble for the same reason. The initial loss in vapor discussed earlier occurs because the smaller pores lead to smaller bubbles which have a lower survival rate. Bubble growth is, therefore, a complex process with some bubbles reaching their theoretical maximum, and others collapsing because of limiting cell wall thickness.

6.2.4 Effect of coalescence on final bubble size distribution

The pores on a paperboard can be very closely spaced, which would cause the bubble growth to be controlled, in part, by the growth rate of neighboring bubbles. A collapse of a neighboring bubble could reduce the amount of vapor driving force and thereby inhibit its growth. The degree to which bubbles can grow or make contact with their neighbors affects the rate of coalescence. It is known that inter-bubble contact leading to coalescence is inevitable if the final foam has a void volume greater than 75% (gas) [3]. The void percentages for the different cases studied here as indicated in Table 6.1 are much higher than 75%, implying very high coalescence rates in all cases. In comparison to traditional foaming the probability of bubbles contacting one another is higher in the present study because the paper surface primarily supports a single layer of bubbles. Coalescence, therefore, plays an important role in controlling the final foam thickness as well as the cell structure. Spherical bubbles provide the best insulation and strength properties [2]. For the same volume of gas, a higher number of bubbles would give better insulation properties.

The degree of coalescence is calculated as the percentage decrease in the number of bubbles from the maximum number seen in the imaging experiments. The increase in foam thickness decreases the number of bubbles as shown in Figure 6.10 because of coalescence. The bubbles were divided into three different size bins (Bin 1: 0-30μm, Bin 2: 31 - 140 μm, Bin 3: 141 – 690 μm) for analyzing the effect of coalescence on foam thickness. Their distribution in the final foam is illustrated in Figure 6.11.

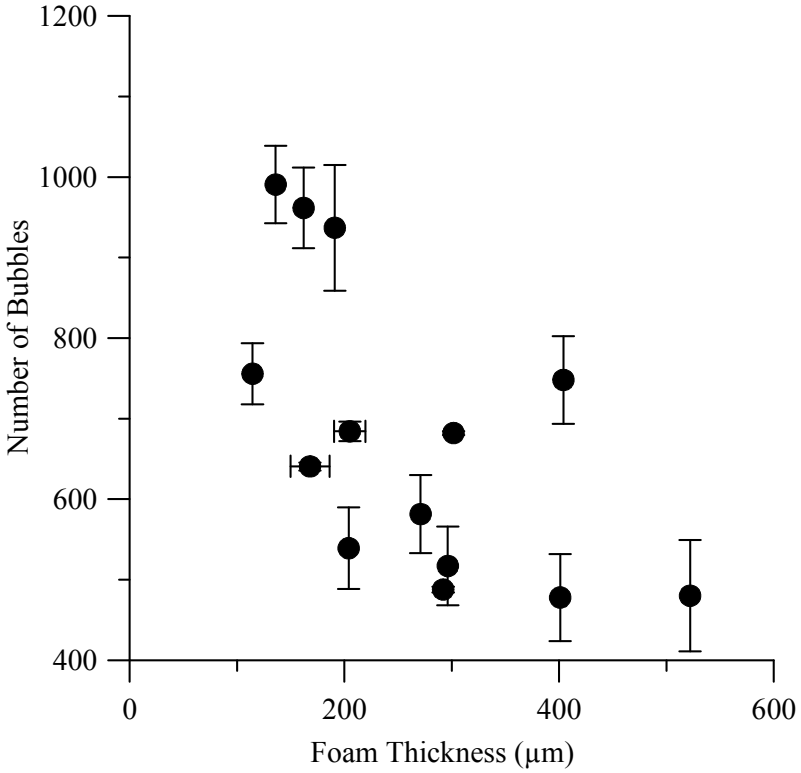

Figure 6.10 Variation in the number of bubbles with foam thickness.

The foam thickness has no dependence on the number of bin 1 bubbles. On the other hand, the percentage of bin 2 bubbles decreases with increasing foam thickness, while the corresponding percentage of bin 3 bubbles increases. In Chapter 5, we have shown that bin 1 bubbles are mostly formed from the pores present on the paper board, while those in bins 2 and 3 are formed by coalescence. Thus the coalescence of bubbles in bin 1 to bin 2 and of bin 2 to bin 3 controls the final foam thickness.

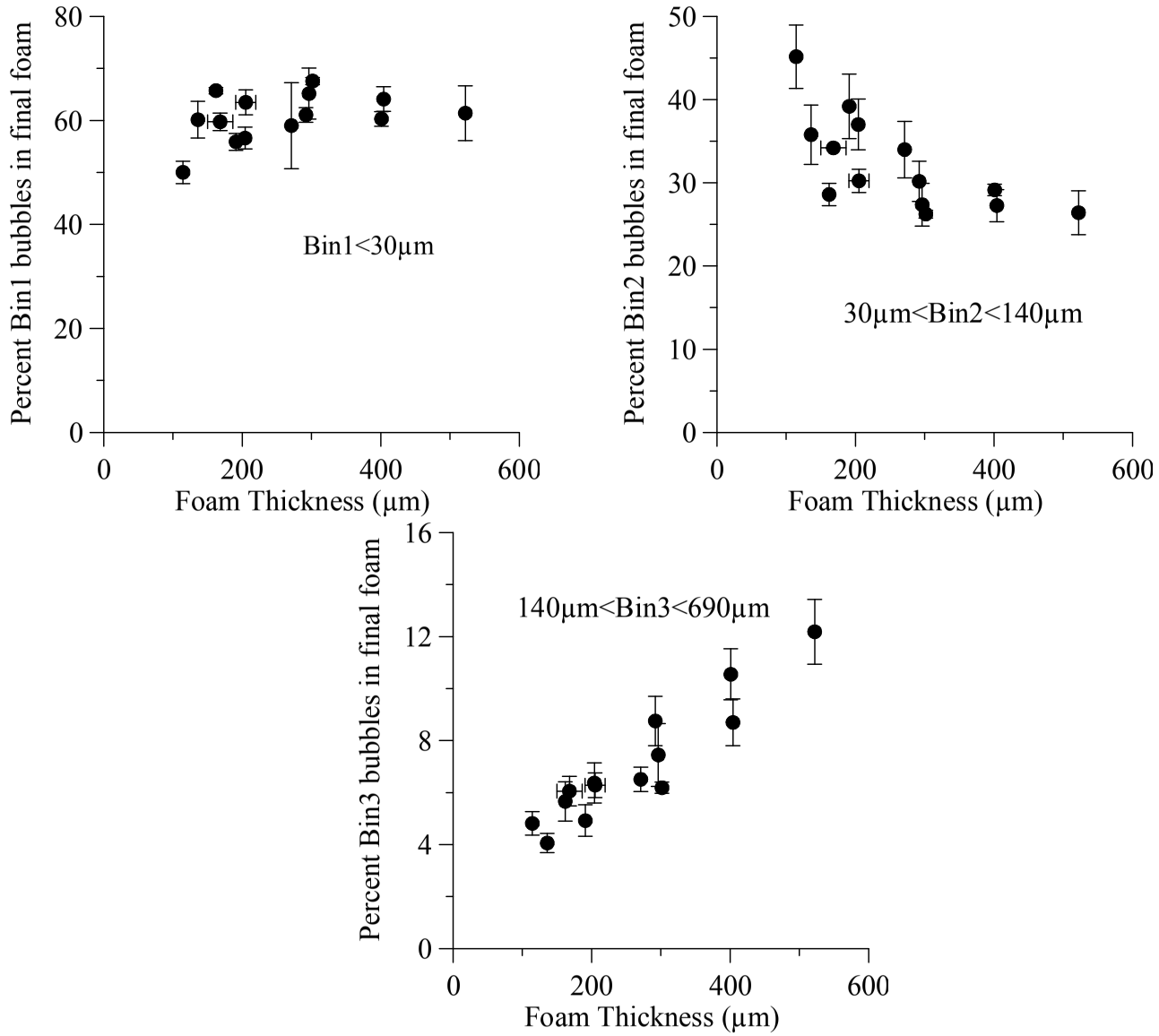

Figure 6.11 Percent bubbles in each size bin of the final foam (120 secs) for the samples listed in Table 6.1.

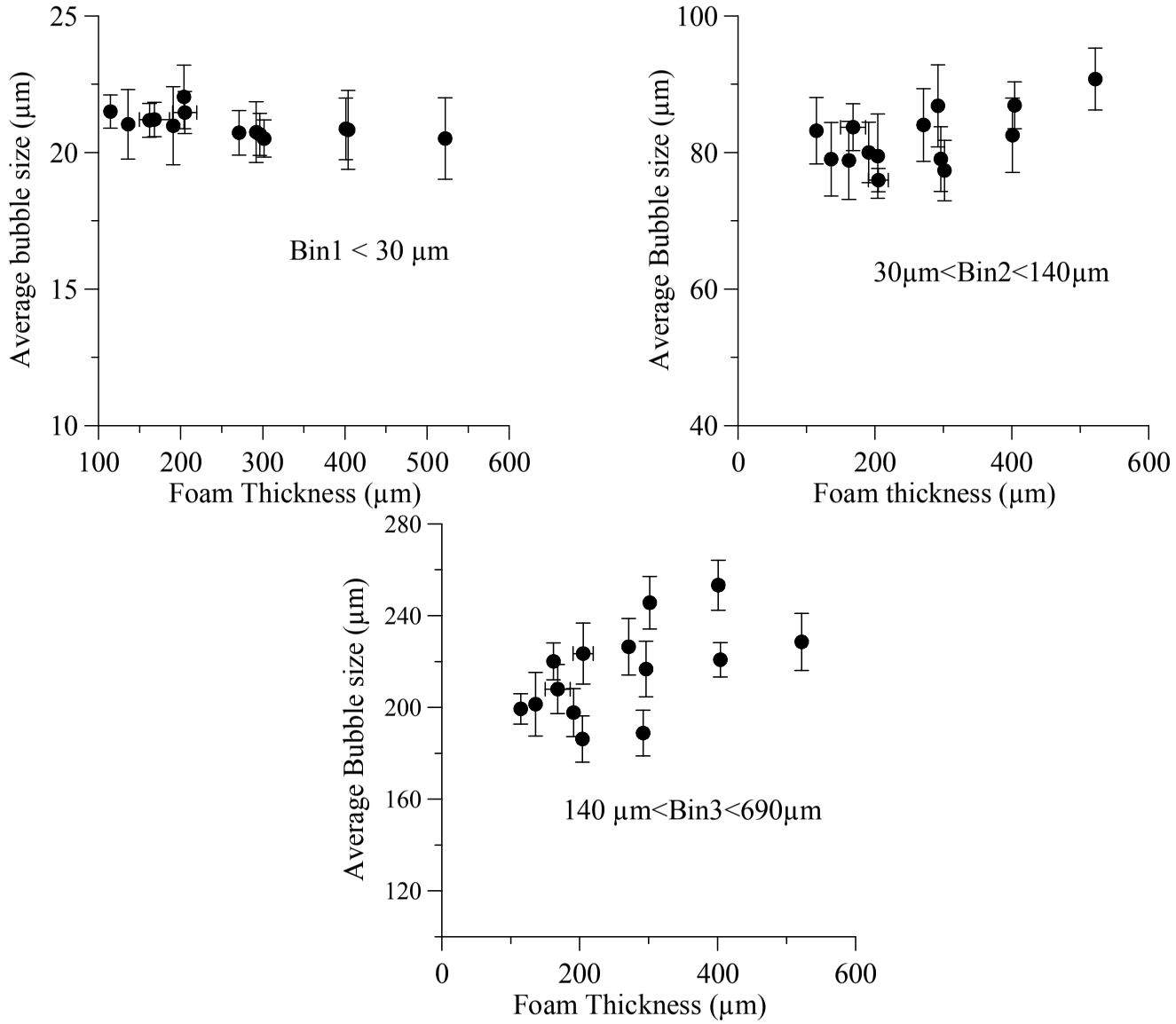

Figure 6.12. Variation of average bubble size in each size bin of the final foam (120 secs) for the samples listed in Table 6.1.

1The average bubble sizes for the different size bins are shown in Figure 6.12. The average size of the smallest bubbles in bin 1 remains constant for the different foam thickness values implying that the increase in foam thickness was a result of coalescence. The second set of larger bubbles in bin 2 shows a small increase in average size with increasing foam thickness while the largest bubbles of bin 3 show a much greater increase in bubble size with increasing foam thickness. This implies that the higher coalescence rates leads to larger sized bin 2 and bin 3 bubbles which contribute to the increased foam thickness. Thicker foam would thus be expected to have a smaller number of large sized bubbles (bin 2 and bin 3 bubbles) as evident in Figure 6.11.

6.3 Conclusion

Only a small percent of the moisture in the board contributes to the final foam. This is the reason for the process being dominated by the vapor driving force and the insignificant role of opposition forces in bubble growth. The maximum bubble size is limited by the point at which the cell wall can no longer balance the pressure inside the bubble. The pore size controls the volume of polymer available for each bubble and hence its wall thickness. A larger pore leads to a larger sized bubble. A thicker polymer also results in a larger bubble for the same reason. This is also due to larger volume of vapor flowing through the pore opening. The final bubble size on the other hand is controlled by the degree of coalescence. The larger sized bubbles which increase the foam thickness result primarily from coalescence.

CHAPTER 7: CONCLUSIONS & FUTURE WORK.

In this chapter, we summarize the findings of research presented in this thesis. We further present the applicability of the results to a commercial process. Possible avenues for future work are also discussed.

7.1 Conclusion

In summary, foaming on paper-polymer composites is caused by water vapor escaping through pores present in the paperboard substrate and then foaming the polymer. The vapor driving force dominates foaming and overcomes the less significant opposition forces (viscoelastic and surface tension forces). The growth rate of bubbles is controlled by the resistance offered to vapor transport by the paperboard substrate. The final bubble size distribution depends on two separate processes. The first is the formation of bubbles at the pores present at the paper-polymer interface. The second process involves the coalescence of these bubbles to form larger sized bubbles. The different parameters that play key roles in the foaming process are summarized in Table 7.1.

The bubbles initially formed are primarily controlled by the pore size distribution, the vapor driving force and the polymer thickness. The pore size distribution depends on the uniformity of the paperboard surface. The pore size controls the amount of polymer that contributes to each bubble, which, in turn, limits the size to which a bubble can grow. The extruded polymer thickness also relates to the amount of polymer available to expand each bubble; hence a thicker polymer and a larger pore would lead to larger

bubble. Larger pore openings allow more vapor flowing into the pore leading to a larger bubble. The vapor driving force depends on the bonding ability of the polymer with the paperboard; poorer bonding of polymer with paper leads to a lower driving force, thus reducing the bubble size. Higher extrusion speeds and lower coated weights contribute to poorer bonding of paper with polymer.

The larger bubbles are principally created by coalescence and depend on the vapor driving force, the distance between bubbles and the size of bubbles initially formed. The smallest bubbles participated most in coalescence and did so in clusters of nearest neighbors.

Coalescence leads to thicker foams due to the formation of larger sized bubbles. The insulation properties directly relate to the amount of gas dispersed in the foam; hence thicker foam gives better insulation. But coalescence also produces a wider distribution of bubbles and leads to a reduction in bubble count. Much better insulation could be obtained if the degree of coalescence was reduced and the individual bubbles allowed to grow larger.

Other factors such as temperature, polymer Melt Index (MI) and moisture content played less significant roles in the foaming process.

Table 7.1 Significance of various parameters in foaming

No.	Parameter	Effect on no of bubbles	Effect on foam thickness
1	Polymer Type	No	**Yes**
2	Extrusion Speed	No	**Yes**
3	Polymer Thickness	No	**Yes**
4	Paper Properties	**Yes**	No
5	Temperature	No	No
6	Moisture	**Yes**	**Yes**
7	Time	**Yes**	**Yes**

7.2 Applicability of findings and future work

The work presented in this thesis is motivated by the commercial significance attached to understanding the fundamentals of the foaming process. The foamed board is currently used to make coffee cups; the industry is seeking to cut costs and to make the manufacturing process more efficient. This work is the first of its kind and hence serves as a springboard for studies to help develop newer applications.

Results from foaming in the lab and in the mill showed similar trends with regard to foam thickness as illustrated in Figure 7.1. The conclusions drawn in the present study are thus directly applicable to a commercial scale foaming set up.

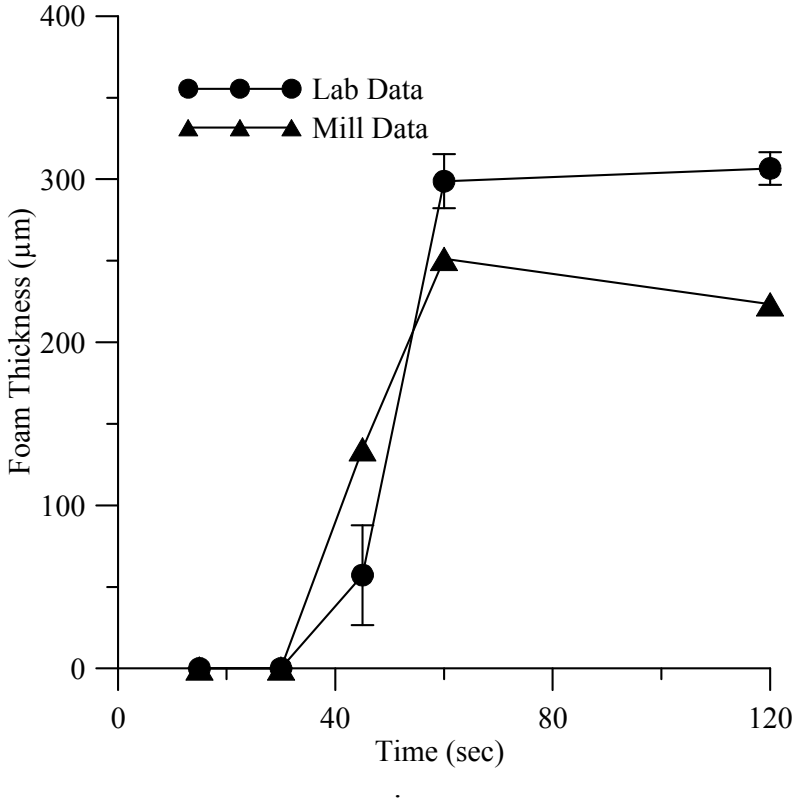

Figure 7.1 Comparison of foam thickness from mill and lab data LDPE EC-482 polymer was extruded at 137m/min to give a thickness of 42.2 µm.

A key conclusion presented in the thesis is with regard to the role of the paperboard substrate. An ideal case of foaming would be one in which a uniform bubble distribution is obtained with all bubbles growing to a constant large size. The pores were closely spaced in the samples used in this work, which was a primary reason for the high degree of coalescence. Coalescence could be reduced by controlling the pore distribution at the interface, which is difficult to do because of the complex nature of the paperboard structure.

A possible way to dictate the pore distribution would be to imprint a predetermined pore shape and size onto the sheet before the polymer is extruded. This could be achieved by

modifying the calendar roll surface on the paper machine. The sheet composition could also be varied on a full scale paper machine and its effect on foaming studied. Techniques such as mercury porosimetry, X-ray microtomography etc. could be used to better understand the effect of pore size and shape on the corresponding bubble size in the foaming process. Foaming of thicker (>42.2 μm) extruded polymers could be studied. The vapor driving force could also be theoretically estimated and the maximum bubble size predicted.

Use of stratified sheets (multi-ply) did not affect the foaming results in the present study. A multi-ply sheet with recycled fiber sandwiched between layers of virgin fibers would make the product more environmentally friendly. Studies in this area could be further pursued. Biodegradable polymers such as starch, polylactic acid, polyvinyl alcohol, polycaprolactone, ethyl vinyl alcohol etc. could be foamed on a paper surface to give a complete environmentally friendly solution to food packaging. The current work could also be expanded by employing a different porous substrate to give newer applications.

REFERENCES

1. Lee, S. T. and Ramesh, N. S., "Polymeric foams: mechanisms and materials", *CRC press*, Boca Raton, FL, 2004.

2. Lee, S. T., Park, C. B., and Ramesh, N. S., "Polymeric Foams: Science and Technology", *CRC press*, Boca Raton, FL, 2007.

3. Weaire, D. and Hutxler, S., "The physics of foams", *Oxford University Press*, New York, 1999.

4. Benning, C.J., "Plastic Foams", Vol I and II, *John Wiley and Sons*, New York, 1969.

5. Cook, J., "http://seattlepi.nwsource.com/venture/260741_vc24.html", Accessed Oct 10th, 2007.

6. Lippner, G. J., Johnston, S., Combs, K., and Walter, D. M., "Storm Water Program: Results of the Caltrans Litter Management Pilot Study", California State University, Sacramento, Office of Water Programs, 2001.

7. Center for Marine Conservation, International Coastal Cleanup, www.cmc-ocean.org/cleanupbro/, Accessed Oct 10th, 2007.

8. Rosario, M., Paparian, M. M. P., Linda, P. C., Mule, R., and Washington, C., (Integrated Waste Management Board), "Use and Disposal of Polystyrene in California", *A Report to the California Legislature*, 2004.

9. "By the Numbers", *Plastics Recycling Update*, 14 (1), 2–3, 2001.

10. Iioka, A., "Method for Producing a Heat-Insulating Paper Container from a Paper Coated or Laminated with a Thermoplastic Synthetic Resin Film", *US Patent, 335346*, 1984.

11. Arefmanesh, A., Advani, S. G. and Michaelides, E. E., "A Numerical study of bubble growth during a low pressure structural foam molding process", *Polymer Engineering and Science*, 30(20), 1330-1337, 1990.

12. Feng, J. J. and Bertelo, C. A., "Prediction of bubble growth and size distribution in polymer foaming based on a new heterogeneous nucleation model", *Journal of Rheology*, 48(2), 439-462, 2004.

13. Colton, J. S. and Suh, N. P., "Nucleation of microcellular foam: Theory and Practice", *Polymer Engineering and Science*, 27(7), 485-492, 1987.

14. Cole, R., ''Boiling nucleation,'' *Advanced Heat Transfer,* 10, 85–166, 1974.

15. Han, J. H. and Han, C. D., ‘‘Bubble nucleation in polymeric liquids. Part II: Theoretical considerations’’, *Journal of Polymer Science*, *Part B: Polymer Physics.,* 28(5), 743–761, 1990b.

16. Lee, J. G. and Flumerfelt, R. W., ‘‘A refined approach to bubble nucleation and polymer foaming process: dissolved gas and cluster size effects,’’ *Journal of Colloid & Interface Science,* 184(2), 335–348, 1996.

17. Griffith, P. and Wallis, J. D., ‘‘The role of surface conditions in nucleate boiling’’, *Chemical Engineering Progress Symposium Ser*ies, 56(30), 49–63, 1960.

18. Ramesh, N. S., Rasmussen, D. H. and Campbell, G. A., ‘‘The heterogeneous nucleation of microcellular foams assisted by the survival of micro voids in polymers containing low glass transition particles. Part I: Mathematical modeling and numerical simulation,’’ *Polymer Engineering and Science,* 34(22), 1685–1697, 1994a.

19. Ramesh, N. S., Rasmussen, D. H. and Campbell, G. A., ‘‘The heterogeneous nucleation of microcellular foams assisted by the survival of micro voids in polymers containing low glass transition particles. Part II: experimental results and discussion,’’ *Polymer Engineering and Science*, 34(22), 1698–1706, 1994b.

20. Ramesh, N. S., Rasmussen, D. H. and Campbell, G. A., ‘‘Numerical and experimental studies of bubble growth during the microcellular foaming process,’’ *Polymer Engineering and Science*, 31(23), 1657–1664, 1991.

21. Arefmanesh, A. and Advani, S.G., ‘‘Diffusion-induced growth of a gas bubble in a viscoelastic fluid,’’ *Rheol. Acta.,* 30, 274–283, 1991.

22. Venerus, D. C. and Yala, N., ‘‘Transport analysis of diffusion-induced bubble growth and collapse in viscous liquids,’’ *AIChE Journal*, 43(11), 2948–2959, 1997.

23. Venerus, D. C., Yala, N. and Bernstein, B., ‘‘Analysis of diffusion-induced bubble growth in viscoelastic liquids,’’ *Journal of Non-Newtonian Fluid Mechanics,* 75(1), 55–75, 1998.

24. Amon, M. and Denson, C., “A study of dynamics of foam growth: analysis of the growth of closely spaced spherical bubbles”, *Polymer Engineering and Science*, 24(13), 1026-1034, 1984.

25. Bird, B. R., Stewart, W. E. and Lightfoot, E. N., “Transport phenomenon”, *Wiley publications*, 2nd edition, 2004.

26. King, J. A., Latham, D. D., and Martin, C. A., *Polyurethane Expo 2001*, Proceedings of the alliance for the polyurethane industry, 472, 2001.

27. Priester R. D., and Turner, R. B., "Chapter 4 - The morphology of flexible polyurethane matrix polymers, Low density cellular plastics", Hilyard, NC and Cunningham, A., Eds., *Chapman & Hall,* London, 1994.

28. Gibson, L. J. and Ashby, M. F., "Cellular solids", *Pergamon press*, Oxford, London, 1988.

29. Van-Krevelin, D. W., "Chapter 13 - Properties of Polymers", 3rd Edition, *Elsevier,* New york, 18, 1990.

30. Glicksman, L., "Foams and cellular materials: thermal and mechanical properties", *MIT Summer course notes*, Cambridge, MA, 1992.

31. Oshima, M., "Polymeric Foaming Simulation: Batch and Continuous", *Foam Extrusion*: *Principles and Practice*, Lee. S.T., Ed. Ch 6, *CRC Press* (ex Technomic), 2000.

32. Park, C. B., Behravesh, A. H., and Venter R. D., "Low Density, Microcellular foam processing in extrusion using CO_2", *Polymer Engineering & Science*, 38(11), 1812-1823, 1998.

33. Naguib, H. E., Park, C. B., Yoon, E. and Reichelt, N., "Fundamental foaming mechanisms governing volume expansion of extruded of PP foams", *Foams 2002*, *Society of Plastics Engineering*, 2002.

34. Roberts, A. P. and Garboczi, E. J., "Elastic moduli of model random three-dimensional closed cell cellular solids", *Acta Materials*, 49(2), 189-197, 2001.

35. Volmer, M. and Weber, A., "Nucleus Formation in Supersaturated Systems," *Z. Phys. Chem.*, 119, 277-289, 1926.

36. Frenkel, J., "Kinetic theory of liquids", *Oxford University press*, Oxford, 1941.

37. Shafi, M. A. and Flumerfelt, R. W., ''Initial bubble growth in polymer foam processes'', *Chemical Engineering Science*, 52(4), 627–633, 1997.

38. Barlow, E. J. and Langlois, W. E., "Diffusion *of* Gas from a Liquid into an Expanding Bubble", *IBM Journal*, 329-337, 1962.

39. Street, J. R., Fricke, A. L. and Reiss, L. P., "Dynamics of phase growth in viscous non Newtonian liquids", *Industrial Engineering Chemistry Fundamentals*, 10(1), 54-64, 1971.

40. Narayan, R., "Biobased & biodegradable Polymer materials: Rationale, drivers, and technology", *Exemplars, ACS symposium series*, 2005.

41. Narayan, R., "Drivers for use of biobased and biodegradable polymer materials and emerging technologies", *40th international symposium on Macromolecules - MACRO 2004*, Paris, 2004.

42. Fujitomo, Y., Ray, S. S. and Okatomo, M., "Well controlled biodegradable nanocomposite foams: from microcellular to nanocellular", *Macrom. Rapid Comm*., 24(7), 457-461, 2003.

43. Huneault, M., "Bio Based Polymers: A review", *19th Foamtech meeting*, *IMI NRC-CNRC*, 2005

44. Guan, J., and Hanna, M. A., "Selected morphological and functional properties of etruded acetylated starch-polylactic acid foams", *Industrial Engineering & Chemistry Research*, 44(9), 3106-3115, 2005.

45. Di, Y. W., Innace, S. and Di, M. E., "Poly (lactic acid)/organoclay nanocomposites: thermal, rheological properties and foam processing", *Journal of Polymer science. Part B- Polym. Physics*, 43(6) 689-698, 2005.

46. Lu, L., Peter, S. J., and Lyman, M. D., "In vitro and in vivo degradation of porous poly(DL-lactic-co-glycolic acid) foams", *Biomaterials*, 21(18), 1837-1845, 2000.

47. Nabar, Y., Raquez, J. M., Dubois, P., and Narayan, R., "Production of starch foams by twin screw extrusion: Effect of maleated poly(butylene adipate-co-terepthalate) as a compatibilizer", *Biomacromolecules* 6(2), 807-817, 2005.

48. Nabar, Y. and Narayan, R., "Twin screw extrusion production and characterization of starch foam products for use in cushioning and insulation applications", *Journal of Polymer Engineering and Science*, 46(4), 438-451, 2006.

49. Nabar, Y. U., Draybuck, D. and Narayan, R., "Physico-Mechanical and hydrophobic properties of starch foams extruded with different biodegradable polymers", *Journal of Applied Polymer Science*, 102(1), 58-68, 2006.

50. Guan, J. and Hanna, M. A., "Post extrusion steaming of starch acetate foams", *Trans. ASAE*, 46 (6), 1613 -1624, 2003.

51. Fang, Q. and Hann, M. A., "Functional properties of polylactic acid starch based loose fill packaging foams", *Cereal chem*., 77 (6), 779-783, 2000.

52. Reedy, M. E., "Natural fiber and wood foam composites", *Blowing agents and foaming processes, RAPRA conference*, Germany, 2005.

53. Tatarka, P. D., *SPE ANTEC Proceedings*, Vol. 53, 2225-2231, 1995.

54. Orsini, F. T., and Davis, E., "Chapter 3 - What is Extrusion Coating?", *Extrusion coating manual* edited by Thomas Bezigian, 4th edition *TAPPI Press*, Atlanta, GA, 7-16, 1999.

55. Osborn, K. R., and Jenkins, W. A., "Plastic Films – Technology and packaging applications", *Technomic Publishing company*, Lancaster, PA, 1992.

56. Jerdee, G. D., "Polyethylene for extrusion coating", Chapter. 21, *Extrusion coating manual*, edited by Thomas Bezigian, 4th edition, *TAPPI Press,* Atlanta, GA, 201-207, 1999.

57. Sherman, P. B., "Ozonization of polymer melt for improved adheshion", Chapter 10 75-87, *Extrusion coating manual,* Edited by Thomas Bezigian, 4th edition *TAPPI Press*, Atlanta, GA, 1999.

58. Michiels, D., "Adhesion improvement by Ozone treatment", *Essochem, International Extrusion Coating symposium*, Antwerp, Belgium, 1982.

59. Johansson, C. J., "Some attempt to improve adhesion in extrusion coating by ozone treatment", Neste OY, Petrochemical Division, Finland.

60. Margrave, D. A., "Chapter 17 - Surface Treatment", *Film extrusion manual, Process, Materials and Properties, TAPPI Press*, 363-416, 1992.

61. Markgraf, D. A., "Corona Treatment: An overview", *Coextrusion Seminar Notes,* 85, *TAPPI Press,* Atlanta, GA, 1986.

62. Thompson, K., "Flame surface treatment – new perspectives", *Polymers, Laminations and coatings conference proceedings, TAPPI Press*, Atlanta, GA, 213, 1987.

63. Furuheim, M. K., Axelson, D.E., Antonsen, H.W. and Helle, T., "Phase Structural analyses of polyethylene extrusion coatings on high density papers. I. Monoclinic Crystallinity", *Journal of Applied polymer Science*, 91(1), 218-225, 2004.

64. Furuheim, M. K., Axelson, D. E., Antonsen, H. W. and Helle, T., "Phase Structural analyses of polyethylene extrusion coatings on high density papers. II. Influence of paper surface properties on the polyethylene morphology", *Journal of Applied Polymer Science,* 91(1), 226-234, 2004.

65. Furuheim, M.K., Axelson, D.E., Antonsen, H.W. and Helle, T., "Phase Structural analyses of polyethylene extrusion coatings on high density papers. III. Determination of the crystallite thickness by T_1 measurements", *Journal of Applied Polymer Science*, 91(1), 235-241, 2004.

66. Thomason, J. L. and Van-Rooyen, A. A., "Transcrystallized interphase in thermoplastic composites", *Journal of Material Science*, 27(4), 897-907, 1992.

67. Butler, T. I., "Chapter 19A - Low Density Polyethylene", *Film extrusion manual, Process, Materials and properties*, *TAPPI press*, 453 -470, 1992.

68. Spell. H. L., "Surface Analysis of corona treated polyethylene: Bonding printability problems", *TAPPI Press*, Atlanta, GA, 1978.

69. Blythe, A. R., Kendall, C. R., Rance, D. G. and Ziehy, V. J. I., "Surface modification of polyethylene by electrical discharge treatment and the mechanism of auto adhesion", *Polymer,* 19(11), 1273-1278, 1978.

70. Lekan, S. F., "Corona Treatment as an adhesion promoter for UV/EB Curable coatings", *RadTech proceedings*, 1988.

71. Polymer Science Learning center, The Department of Polymer Science, The University of Southern Mississippi, http://www.pslc.ws/macrogcss/pe.html, Accessed Oct 10th, 2007.

72. Shenoy, A. V. and Saini., D. R., "Melt Flow Index: More Than Just a Quality Control Parameter. Part I.", *Advances in Polymer Technology*, 6 (1), 1- 58, 1997.

73. Bliesner, W. C., "A Study of the Porous Structure of Fibrous Sheets Using Permeability Technique", *PhD Thesis, Institute of Paper Science & Technology,* Appleton, WI, 1963.

74. Smook, G. A., "Handbook for Pulp and Paper Technologists", ed. M.J. Kocurek., TAPPI *and CPPA*, Montreal, Quebec, Canada, 395, 1982.

75. Polat, O., Reinhold, C. H. and Douglas, W. J. M., "Transport Phenomena Analysis of Through Drying Paper", *Industrial Engineering and. Chemistry Research*, 31(3), 736-743, 1992.

76. Biermann, C. J., "Handbook of Pulping and Papermaking", *Academic Press*: San Diego, CA, 754, 1996.

77. Clark, J. D. A., "Pulp technology and treatment for paper", 2nd ed., *Miller Freeman Publications*, Inc., San Francisco, CA, 878, 1985.

78. Karlsson, M., "Papermaking Part 2, Drying", *Papermaking Science & Technology CD-ROM,* TAPPI & Finnish Paper Engineers Association, 2002.

79. Page, D. H., "The beating of chemical pulps - the action and the effects", Fundamentals of Papermaking*, 9th Fundamental Research Symposium,* Cambridge: FRC, 1989.

80. Emerton, H. W., "Fundamentals of the beating process", *The British Paper and Board Industry Research Association*, Kenley, England, 1957.

81. Giertz, H. W., "The effects of beating on individual fibers, in Fundamentals of Papermaking Fibres"*, 1st Fundamental Research Symposium*, F. Bolam, Editor. FRC: Cambridge, 389-409, 1957.

82. Hietanen, S. and K. Ebeling, "Fundamental Aspects of the Refining Process", *Paperi ja Puu*, 72(2), 158-170, 1990.

83. Higgins, H. G. and Yong, J. De., "The beating process - primary effects and their influence on pulp and paper processes", *Formation and Structure of Paper, 2nd Fundamental Research Symposium*, Oxford: FRC, 1961.

84. Campbell, B. W., "Hydration and beating of cellulose pulps". *Industrial and Engineering Chemistry*, 26(2), 218-219, 1934.

85. Walsh, J. F., "An Isotopic study of fiber-water interactions", *PhD Thesis*, *Georgia Institute of Technology*, Atlanta, GA, 2006.

86. Brunauer, S., Emmet, P.H. and Teller, E., "Adsorption of gases in multimolecular layers", *Journal of the American Chemical Society*, 60(2), 309-319, 1938.

87. Child, T. F. and Jones, D. W., "Broad-Line NMR Measurement of Water accessibility in Cotton and Wood pulp Celluloses", *Cellulose Chemistry and Technology*, 7(5), 525-534, 1973.

88. Weise, U., Maloney, T. and Paulapuro, H., "Quantification of water in different states of interaction with wood pulp fibers", *Cellulose,* 3(4), 189-202, 1996.

89. Weise, U., "Characterization and mechanisms of chenages in wood pulp fiber caused by water removal", *PhD Thesis, Helsinki University of Technology*, Finland, 1997.

90. Jayme, G. and Roffael, E., "Die Anwendung des WRV-Wertes zur Erfassung von Strukturanderungen der Cellulose", *Das Papier*, 24 (6), 335-340, 1970.

91. Stone, J. F. and Scallan, A. M., "The effect of component removal upon the porous structure of the cell wall of wood II. Swelling in Water and the Fiber Saturation Point", *TAPPI Journal*, 50(10), 496−501, 1967.

92. Magne, F. C., Portas, H. J. and Wakeham, H., "A calorimetric investigation of moisture in textile fibers", *Journal of the American Chemical Society*, 69(8), 1896-1902, 1947.

93. Maloney, T. C., Paulapuro, H. and Stenius, P., "Hydration and swelling of pulp fibers measured with differential scanning calorimetry", *Nordic Pulp and Paper Research Journal*, 13(1), 31-36, 1998.

94. Caulfield, D. F., "The effect of cellulose on the structure of water: view 2. in Fiber-Water Interactions in Paper-Making", *VIth Fundamental Research Symposium,* Oxford: FRC, 1977.

95. Walsh, F. L. and Banerjee, S., "Characterization of thin water layers in pulp by tritium exchange. Part 1: Methods development", *Holzforschung*, 61(2), 115-119, 2007.

96. Walsh, F. L. and Banerjee, S., "Characterization of thin water layers in pulp by tritium exchange. Part 2: Effect of refining on water absorption", *Holzforschung*, 61(2), 120-123, 2007.

97. Herrington, T. M. and Petzold, J. C., "Surface area of paper making wood pulps used by the British paper industry", *Cellulose*, 2(2), 83-94, 1995.

98. Pounder, J. R., "A mathematical model of high intensity paper drying*", PhD Thesis, Georgia Institute of Technology*, Atlanta, GA,1986.

99. Gupta, H., "Moisture Transport in Paper under Steady and Unsteady Conditions Investigated with a Parallel Diffusion Concept", *Ph.D. Thesis, SUNY College of Environmental Science and Forestry,* Syracuse, NY, 2003.

100. Devlin, P, "An investigation of mechanism of High Intensity Drying", *PhD thesis, Georgia Institute of Technology*, Atlanta, GA, 1986.

101. Redon, S. A., Davis, M. R. and Doe P. E., "Construction of an analytical model of paper drying", *Drying Technology*, 17(4&5), 655-690, 1999.

102. Holm, R. A., Holderby, J. M. and Perry, J. F., "Machine operating conditions and their influence on drying rate", Report Three, Project 2693. *The Institute of Paper Chemistry*, Appleton, WI, 65, 1970.

103. Ahrens, F. W., Kartsounes, G. T. and Ruff, D. L., "A laboratory study of hotsurface drying at high temperature and mechanical loading", *Proceedings of the CPPA Technical Section Annual Meeting*, Vol. B, 93-97, Montreal, 1982.

104. Burton, S. W., "An investigation of dynamic densification under impulse drying conditions", Progress Report Six. *The Institute of Paper Chemistry*, Appleton, WI, 30, 1985.

105. Ahrens, F. W., "Fundamentals of drying", Status Report to the Engineering Project, Advisory Committee, Project 3470, *The Institute of Paper Chemistry*, Appleton, WI, 21, 1984.

106. Ahrens, F., "Wet Pressing Fundamentals", Project 3480 Status report, *Institute of Paper Chemistry*, Appleton, WI, 1984.

107. Lindsay, J. D., "The Physics of Impulse drying: New Insights from numerical modeling", *IPST Technical paper series*, No. 330, Atlanta, GA, 1989.

108. Carson, F. T., "Effect of experimental conditions on the measurement of air permeability of paper", *Bur. Standards J. Research,* 12, 587-60, 1934.

109. Bublitz, W. J., Jr. “A study of the air permeability of paper at high pressures”, *MS Thesis, The Institute of Paper Chemistry*, Appleton, WI, 89, 6, 1947.

110. Coupe, R. R., “Air permeability of paper”, *Proc. Tech. Sect. British Paper & Board Makers Assoc*, 31(2), 383-457, 1950.

111. Mokadam, R. G., “Thermodynamic Analysis of the Darcy law*”, Journal of Applied Mechanics*, 28, 208-12, 1961.

112. Kozeny, J., Sitzungsber. Akad. Wiss. Wien, 136, 271-306, 1927.

113. Carman, P. C., “Fluid flow through granular beds”, *Transactions of the Institution of Chemical Engineers,* 15, 150-66, 1937.

114. Fowler, J. L. and Hertel, K. L., "Flow of a Gas through Porous Media," *Journal of Applied Physics*, 11(7), 496-502, 1940.

115. Knauf, G. H. and Doshi, M. R., “Calculation of aerodynamic porosity, specific surface area and specific volume from Gurley seconds measurements”, *IPC Technical Series*, No 183, *Georgia Institute of Technology*, Atlanta, GA,1986.

116. Mitchell, C., “Thermography is Accurate Tool, Aids in Preventative Maintenance”, *Pulp and Paper*, 61(13), 130-131, 1987.

117. Thermovision, A20 series operator’s manual, “Chapter 15 - Theory of Thermography”, *FLIR Systems*, Danderyd, Sweden, 2003.

118. Fike, G. M., “Using Infrared Thermography to Image the Drying of Polymer Surfaces” *MS Thesis, Georgia Institute of Technology*, Atlanta, GA, 2004.

119. Fike, G. M., Abedi, J., Banerjee, S., “Imaging the drying of surfaces using Infrared Thermography”, *Industrial & Engineering Chemistry Research*, 43(15), 4178-4181, 2004.

120. TAPPI T410 om-02, “Grammage of paper and paperboard (weight per unit area)”, *TAPPI Test methods*, TAPPI Press, Atlanta, GA, 2002.

121. Smith, T., “Investigation of Wet paper viscoelastic structural properties”, *MS Thesis, School of Mechanical Engineering, Georgia Institute of Technology*, Atlanta, GA, 2006.

122. Fleischman, E. H. Jr., “An investigation of the elastic and dielectric anisotropy of paper”, *PhD Thesis, Institute of Paper Science & Technology*, Atlanta, GA, 1981.

123. Waterhouse, J. F., “Effect of some papermaking variables on formation”, *IPST Technical paper series number,* Atlanta, GA, 438, 1992.

124. Hutten, I. M., "Linerboard handsheets for USDA forest products laboratory", Project 3881, *Final Report: A Progress Report to U.S. Department of Agriculture Forest Products Laboratory*, Madison, WI, Georgia Institute of technology, Atlanta, GA, 1994.

125. TAPPI T402 sp-03, "Standard conditioning and testing atmospheres for paper, board, pulp handsheets, and related products", *TAPPI Test Methods*, TAPPI Press, Atlanta, GA, 2007.

126. Phantom v4.2 camera manual, Vision Research Inc., Wayne, New Jersey, 2004.

127. Phantom Camera Control Software Documentation, Version 607, Vision Research Inc., Wayne, New Jersey, 2004.

128. Rasband, W. S., Image J. National Institutes of Health, Bethesda, Maryland, USA, http://rsb.info.nih.gov/ij/, 1997-2004.

129. TAPPI T 200 sp 06, "Laboratory beating of Pulp (Valley beater method)", *TAPPI Test Methods,* TAPPI Press, Atlanta, GA, 2006.

130. TAPPI T 227 om-04, "Freeness of Pulp (Canadian Standard Freeness)", *TAPPI Test Methods*, TAPPI Press, Atlanta, GA, 2004

131. TAPPI T 460 om-06, "Air resistance of paper (Gurley Method)", *TAPPI Test Methods*. TAPPI Press, Atlanta, GA, 2006.

132. TAPPI T 551 om-06, "Thickness (caliper) of paper and paperboard (soft platen method)", *TAPPI Test Methods*, TAPPI Press, Atlanta, GA, 2004.

133. TAPPI T 411 om-05, "Thickness (caliper) of paper, paperboard and combined board", *TAPPI Test Methods*, TAPPI Press, Atlanta, GA, 2005.

134. Park, C. B., Cheung, K. L. and Song, S. W., "The effect of talc on cell nucleation in extrusion foam processing of polypropylene with CO2 and isopentane", *Cellular Polymers*, 17(4), 221-251, 1998.

135. Rodrigue, D. and Gosselin, R., "The effect of calcium carbonate particle size on LDPE foam morphology", *Blowing Agents and Foaming Processes Conference*, 157-166, 2002.

136. TAPPI T455 sp-04, "Identification of wire side of paper", *TAPPI Test Methods*, TAPPI Press, Atlanta, GA, 2004.